

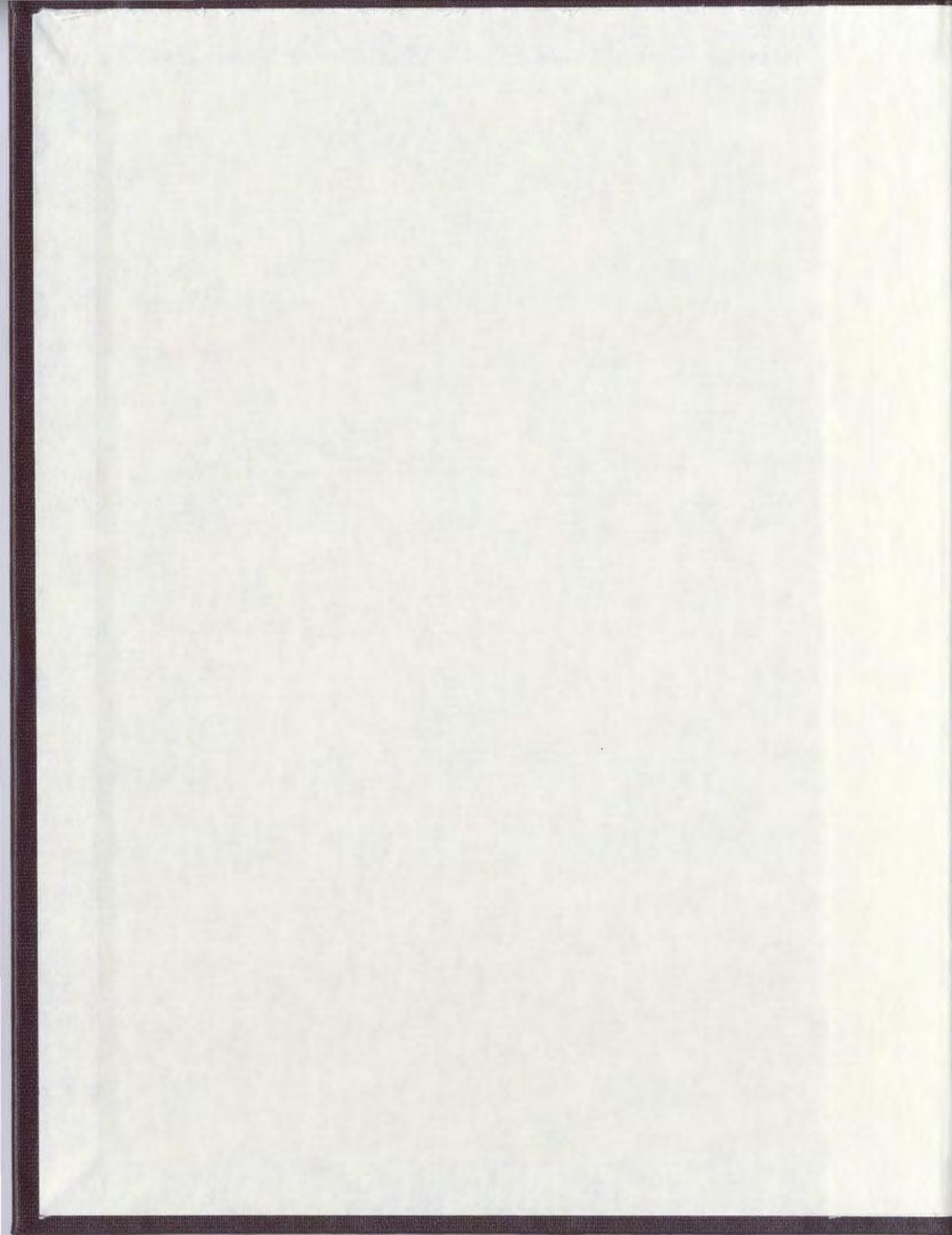
FAULT IMAGING OF HIBERNIA THREE-DIMENSIONAL
SEISMIC DATA USING EDGE DETECTION AND
COHERENCY MEASURES

CENTRE FOR NEWFOUNDLAND STUDIES

**TOTAL OF 10 PAGES ONLY
MAY BE XEROXED**

(Without Author's Permission)

NICHOLLE ANNA GLADYS CARTER





National Library
of Canada

Acquisitions and
Bibliographic Services

395 Wellington Street
Ottawa ON K1A 0N4
Canada

Bibliothèque nationale
du Canada

Acquisitions et
services bibliographiques

395, rue Wellington
Ottawa ON K1A 0N4
Canada

Your file Votre référence

Our file Notre référence

The author has granted a non-exclusive licence allowing the National Library of Canada to reproduce, loan, distribute or sell copies of this thesis in microform, paper or electronic formats.

The author retains ownership of the copyright in this thesis. Neither the thesis nor substantial extracts from it may be printed or otherwise reproduced without the author's permission.

L'auteur a accordé une licence non exclusive permettant à la Bibliothèque nationale du Canada de reproduire, prêter, distribuer ou vendre des copies de cette thèse sous la forme de microfiche/film, de reproduction sur papier ou sur format électronique.

L'auteur conserve la propriété du droit d'auteur qui protège cette thèse. Ni la thèse ni des extraits substantiels de celle-ci ne doivent être imprimés ou autrement reproduits sans son autorisation.

0-612-47443-7

Canada

**Fault Imaging of Hibernia Three-Dimensional Seismic Data
Using Edge Detection and Coherency Measures**

By

Nicholle Anna Gladys Carter

A thesis submitted to the
School of Graduate Studies
In partial fulfilment of the
Requirements for the degree
of Master of Science

**Department of Earth Sciences
Memorial University of Newfoundland**

May 1999

St. John's

Newfoundland

Abstract

Seismic methods play a key role in exploration and reservoir characterization of the offshore Newfoundland Hibernia oil field. Seismic data is traditionally processed to image continuous reflections rather than to image discontinuities such as faults. Thus, when interpreting such 3D seismic data it is often difficult to obtain a clear and unbiased view of faults. Due to the complex structure of offshore Newfoundland fields, fault imaging is extremely important since field production may be affected by sealing faults, and may effect hydrocarbon production and development strategies.

In recent years, companies have produced algorithms for enhanced fault detection. The edge detection differencing method, as presented by Lou et al., (1996), measures changes in the subsurface such as faults using differencing of seismic traces. The C1 coherency algorithm, as described by Marfurt et al., (1998), uses cross-correlation between seismic traces. Another method used for fault detection is second derivative maps which take the second derivative of the seismic traces.

The main objective of the this study is to compare different fault detection algorithms using both synthetic (Kelly, 1998) and real seismic data from the Hibernia fields (1991 and 1997 surveys). For each data set, a representative of the data volume containing the Murre fault was chosen for comparison purposes. Results indicating that the coherency method produces best results with the second derivative produce good results for the model data. The use of EDGE and Poststack/PAL software proved to image more subtle faulting than large scale faulting such as the Murre fault.

Acknowledgments

This work would not have been possible without the help of numerous people whom I would like to thank.

The Hibernia management and development corporation (HMDC) for providing a workstation and software and for partially funding my thesis through a scholarship. I would especially like to thank John Evans, Larry Sydora and David Slater for their help while I was in their offices working.

Irene Kelly for providing the model and real data sets for this thesis. I would also like to thank Irene for her help with answering the numerous questions that I had throughout this work.

Chevron for the allowing me to use their computer and software for this thesis.

Husky Oil for their help in providing computers and printer for the completion of this thesis and to thank Florence Remillard for her help with data loading and project set-up on the Landmark system and David Emery for his help with Landmark Poststack/PAL.

My supervisor away from home, Dr. Larry Lines, for making it possible for me to work on this project and to expand my horizons in the field of geophysics. His support means a great deal to me, thank you so much.

My supervisor at home, Dr. Chuck Hurich, for his help in making this thesis a finished product.

All of my family and friends for their support and never ending questions "when are you going to finish" I know there were many answers through the years but the answer now is "it is finished!!".

My parents Cecil and Freda Evans for their support throughout my years in school and encouraging me that "I could do whatever I put my mind to". Thanks, you mean the world to me.

Finally, my husband James, you were the one to kick me in the butt when I didn't want to work but still let me have fun. You have been my source of strength through the last months of writing this thesis and a great help throughout my graduate student years.

TABLE OF CONTENTS

Abstract	i
Acknowledgements	ii
List of Figures	vi
List of Tables	viii
1 Introduction	1
1.1 Outline of study.....	1
1.2 Previous geophysical work.....	2
1.2.1 Three-dimensional seismic interpretation.....	2
1.2.2 Coherence and Edge Detection.....	4
2 Geophysical Methods	6
2.1 Introduction.....	6
2.2 Coherency Measurement.....	7
2.2.1 Cross-correlation.....	10
2.2.2 Semblance.....	13
2.3 Difference methods and second derivative maps.....	14
2.4 Geophysical background.....	16
3 Regional Geology of the Jeanne d'arc Basin	19
3.1 Tectonic history.....	19

3.2	Regional structure.....	21
3.3	Hibernia structure.....	24
3.4	Regional Stratigraphy.....	25
4	Model Studies	29
4.1	Comparisons of coherency measures to unmigrated and migrated data.....	29
4.2	Description of 3D model.....	36
4.3	Testing of methods.....	37
4.3.1	Coherency Results.....	37
4.3.2	Differencing Results	45
4.3.3	Second Derivative Results	53
4.4	Comparison of Results.....	58
5	Hibernia Real Data Examples	65
5.1	Application to 3D depth migrated data.....	65
5.2	Comparison of depth migrated results.....	70
5.3	Application differencing and coherency methods to time migrated data.....	74
5.3.1	Differencing results using time migrated data.....	75
5.3.2	Coherency results using time migrated data.....	82
5.3.3	Comparison of EDGE and Poststack/PAL.....	91

6 Discussion and Conclusions	94
6.1 Effects of imaging on fault detection.....	94
6.2 Comparison of methods.....	94
6.3 Recommendations.....	95
References	97
Appendix A	100

Figure	List of Figure	Page
Figure 1.1	Fault detection methods currently available	3
Figure 2.1	correlation coefficients reflect variations in geology	8
Figure 2.2	Comparison pattern for coherency	9
Figure 2.3	Illustrates how coherency is measured	11
Figure 2.4	Seismic grid and well locations of the Hibernia field	17
Figure 2.5	Model data consisting of seven layers and Murre fault	18
Figure 3.1	Location Map of the Jeanne d'Arc basin	20
Figure 3.2	Lithostratigraphic column of the Jeanne d'Arc basin	22
Figure 3.3	Regional structure map	23
Figure 3.4	Location map of the Hibernia field	26
Figure 3.5	Hibernia structure map	27
Figure 4.1	Simple extensional fault model	30
Figure 4.2	Unmigrated section of the fault model	32
Figure 4.3	Reverse time migrated section of the fault model	33
Figure 4.4	Differencing result of unmigrated section	34
Figure 4.5	Differencing result of reverse time migrated section	34
Figure 4.6	Synthetic seismic data for inline 60	38
Figure 4.7	Synthetic seismic data for depth slab 215	39
Figure 4.8	Synthetic seismic data for depth slab 250	40

Figure	List of Figures	Page
Figure 4.9	Synthetic seismic data for depth slab 175	41
Figure 4.10	Coherency result of depth slab 215	43
Figure 4.11	Coherency result of depth slab 250	44
Figure 4.12	Coherency result of depth slab 170	46
Figure 4.13	Coherency result of inline 60	47
Figure 4.14	Differencing result of depth slab 215	48
Figure 4.15	Differencing result of depth slab 250	49
Figure 4.16	Differencing result of depth slab 175	50
Figure 4.17	Differencing result of inline 60	51
Figure 4.18	Second derivative result of depth slab 215	54
Figure 4.19	Second derivative result of depth slab 250	55
Figure 4.20	Second derivative result of depth slab 175	56
Figure 4.21	Second derivative result of inline 60	57
Figure 4.22	Comparison of fault detection results of depth slab 215	59
Figure 4.23	Comparison of fault detection results of depth slab 250	60
Figure 4.24	Comparison of fault detection results of depth slab 175	61
Figure 4.25	Comparison of fault detection results of inline 60	62
Figure 4.26	Comparison of differencing and deconvolution.	64
Figure 5.1	Basemap of 1991 3D seismic survey illustrating outline of real data subset.	66
Figure 5.2	Line 60, real data set	67

Figure	List of Figures	Page
Figure 5.3	Plane through real data at 275	68
Figure 5.4	Plane through real data at 325	69
Figure 5.5	Comparison of results for depth section 275	71
Figure 5.6	Comparison of results for depth section 325	72
Figure 5.7	Comparison of results for line 60	73
Figure 5.8	Seismic basemap of Hibernia time data	76
Figure 5.9	Differencing results using varying window sizes	79
Figure 5.10	EDGE results using variation in comparison pattern	80
Figure 5.11	EDGE results of dip steering	81
Figure 5.12	Poststack/PAL results using amplitude scaling and normalization values	85
Figure 5.13	Poststack/PAL results of dip steering	87
Figure 5.14	Poststack/PAL results of varying vertical window size.	88
Figure 5.15	Poststack/PAL result of correlation vs. semblance	89
Figure 5.16	Semblance results of subset #2	90
Figure 5.17	Arbitrary lines illustrating the effects of changing vertic window size	92
Figure 5.18	Comparison of EDGE and Poststack/PAL	93
Table	List of Tables	Page
Table 5.1	EDGE testing using time data	78
Table 5.2	Poststack/PAL testing using time data	84

CHAPTER 1

INTRODUCTION

1.1 Outline of Study

Seismic methods play a key role in exploration and reservoir characterization of the offshore Newfoundland Hibernia oil field. With the development of digital-processing methods, it has become possible to extract huge amounts of geological information from seismic data. Also, with the introduction of three-dimensional (3D) seismic data in the late 1970's, interpretation and imaging uncertainties have been reduced when interpolating between seismic lines (Yilmaz, 1987). Three-dimensional seismic methods also aid in better interpretation of structural detail.

There are several reasons why discontinuities occur in a seismic section. These include structural variation (faulting), stratigraphic or lithologic changes, highly dipping events, lack of reflectors (e.g., salt), and poor data quality. This study will focus on imaging discontinuities that are the result of structural variation due to faulting.

Seismic data is traditionally processed to image continuous reflections rather than to image discontinuities such as faults. Thus, when interpreting 3D seismic data it is often difficult to obtain a clear and unbiased view of faults. Due to the complex structure of offshore Newfoundland fields, fault imaging is extremely important since field production may be affected by sealing faults (Hurley et al., 1992). Therefore, it is important to clearly image faults within the Hibernia structure for the purpose of hydrocarbon production and

development.

In recent years companies such as Amoco, Chevron, and Landmark have produced algorithms for enhanced fault detection. Figure 1.1 outlines the different fault detection methods currently available, separated into categories of seismic edge detection or coherency. The difference method developed by Chevron Petroleum Technology Company (CPTC) measures changes or detects discontinuities in the subsurface such as faults using differencing of seismic traces whereas the coherence method developed by Amoco and Landmark uses cross-correlation between two seismic traces. In addition to these commercially developed techniques, I have also tested second derivative mapping. Second derivative techniques (which are popular in potential field mapping) emphasize the high wavenumber content in data and are in some cases equivalent to the differencing method.

The main objective of this study is to compare different coherency algorithms using both synthetic (Kelly, 1998) and real seismic data from the Hibernia field (1991 and 1997 surveys). For each data set, a representative of the data volume containing one or two of the main interpreted faults will be chosen. Currently in the petroleum industry there are several fault imaging techniques but to date there have been few comparative studies which would allow the user to decide which tool is appropriate for the particular problem.

1.2 Previous Geophysical Work

1.2.1 Three-Dimensional Seismic Interpretation

Three-dimensional (3D) seismic interpretation has several advantages over two-dimensional seismic interpretation due to the 3D nature of geological studies. One

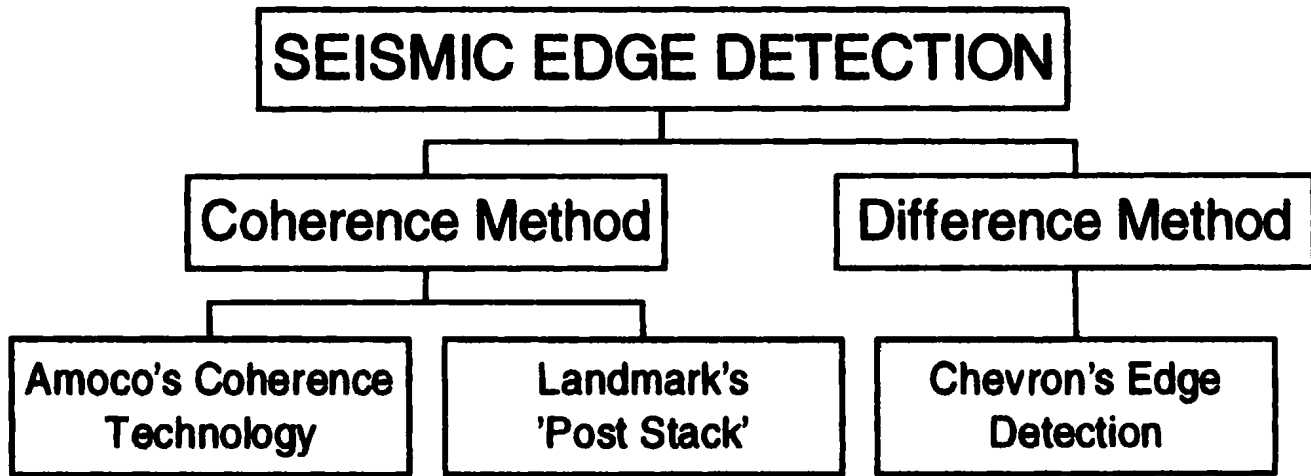


Figure 1.1: Flowchart of available seismic edge detection techniques.

advantage is that 2D seismic interpretation is limited to a vertical cross-section, whereas 3D data can be displayed in a horizontal section or map view. This has its advantages in that one can determine the lateral extent of faulting as well as stratigraphic changes in the subsurface. Horizontal seismic displays may be used to display amplitude maps for time and seismic horizon slices. A time slice is a plane through the 3D data volume that contains events from more than one reflecting horizon at the same time interval. Time slices are used to generate structural contour maps. Seismic horizon slices are slices through the 3D data volume, which are seismic amplitudes associated with an interpreted horizon. Although it is easier to trace faults and stratigraphic features when using a horizon slice, it may still be difficult to pick the stratigraphic horizon which is of interest, and there may also be interpretative bias involved when interpreting faults. If we depth migrate our data, then we interpret depth slices, rather than time slices.

1.2.2 Coherence and Edge Detection

Although it is easier to view faults and stratigraphic features using 3D horizontal slices it is still difficult to obtain a clear and unbiased view of these features, since it is not clear whether discontinuities are fault related or not. Over the past several years imaging techniques have been developed to measure discontinuities such as faults and stratigraphic features instead of continuous reflections. Bahorich and Farmer (1995) of Amoco have developed a way of revealing fault surfaces within a 3D volume for which no fault reflections have been recorded. This technique is called 3D coherence or

coherence cube and the algorithm was described by Marfurt et al. (1998). Another similar technique has since been developed by Landmark (1996) called continuity analysis. This technique is said to reveal and emphasize lateral changes. This was followed by a fault imaging technique developed by Chevron Petroleum Technology Company (CPTC), as presented by Luo et al. (1996), called edge detection that measures variations in the subsurface such as changes in structure and stratigraphy. All three techniques are designed to improve fault interpretation. Comparisons of the fault detection techniques will be the main focus of this project.

Although several fault detection techniques are used on various synthetic and real data sets, not all methods were used on all data sets. This was due to the fact that our processing was done on different platforms and the same software was not available on all platforms. Nevertheless, comprehensive comparisons of the C1, the edge detection differencing, and the second derivative method were carried out on both synthetic and real Hibernia data. The C2 (semblance) method was used on the real data. For the reader's interest, a comparison of the C1 and C2 algorithms on Trinidad data was published by Marfurt et al. (1998).

CHAPTER 2

GEOPHYSICAL METHODS

2.1 Introduction

Detection of discontinuities in seismic data is a relatively new technique aimed at locating faults and stratigraphic terminations. Thus far there have been two unique algorithms created, differencing (CPTC, 1996) and coherency (Amoco, 1995 and Landmark, 1996). Both of these algorithms image discontinuities using different mathematical techniques. The Amoco and Landmark coherency algorithms (described by Marfurt et al., 1998) utilize cross-correlation (multiplication and summation) between two seismic signals A and B and is written as:

$$C(t) = \bar{A}X\bar{B} = \sum A_t + \tau B_\tau \quad (2.1)$$

Where a and b are vectors containing seismic trace time sequences $A=(A_0, A_1, A_2, \dots, A_n)$ and $B=(B_0, B_1, B_2, \dots, B_n)$, and where τ is the time shift of b relative to a. The difference method is a simpler technique which measures differences between seismic signals (signal A on the target trace and signal B on an adjacent trace) and can be written as:

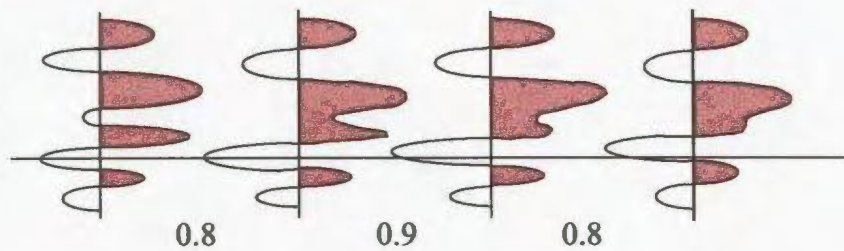
$$\bar{d} = |\bar{A} - \bar{B}| / (|\bar{A}| + |\bar{B}|) \quad (2.2)$$

where d is the difference at the center sample of the window on the target (Luo et al., 1996).

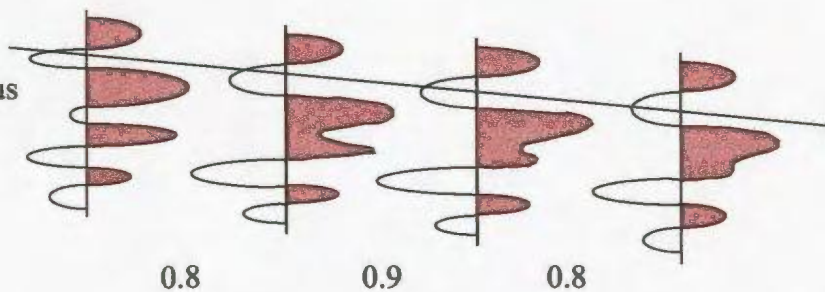
2.2 Coherency Measurement

Coherency is a measure of lateral changes in the seismic response due to variation in structure and stratigraphy (Marfurt et al., 1998). One possible coherency measurement is cross-correlation. Cross-correlation measures the degree of similarity or linear relationship between a pair of traces; a measure of how much two traces look alike or the extent to which one can be considered a linear function of the other (Sheriff, 1982). To relate this to geology, you would expect high correlation when traces are similar or when the geology is flat and continuous, lower values when it is dipping and continuous, and anomalous values when it is discontinuous (Landmark, 1996). Figure 2.1 illustrates a simplified example of how correlation coefficients reflect variations in geology when using a one-trace comparison pattern. Coherency analysis using Landmark PostStack is more robust than this simplified example and compares each trace to two, four, or eight adjacent traces. It has a user identified comparison pattern as shown in figure 2.2. This comparison of traces is calculated for each trace pair within the comparison pattern and is determined and assigned to the central sample in the comparison window. The correlation option measures data continuity using cross-correlation. Therefore, for each trace, data within the time window is cross-correlated with data from 2, 4, or 8 adjacent traces and then compared to the central trace using continuity attributes such as minimum correlation, maximum correlation, and average correlation.

Flat and Continuous
Geology



Dipping and Continuous
Geology



Flat and Discontinuous
Geology

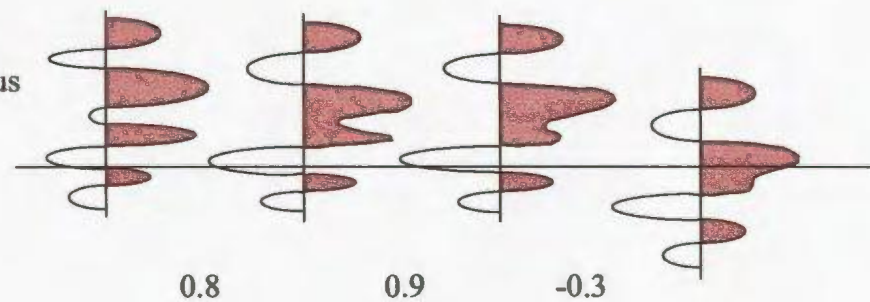
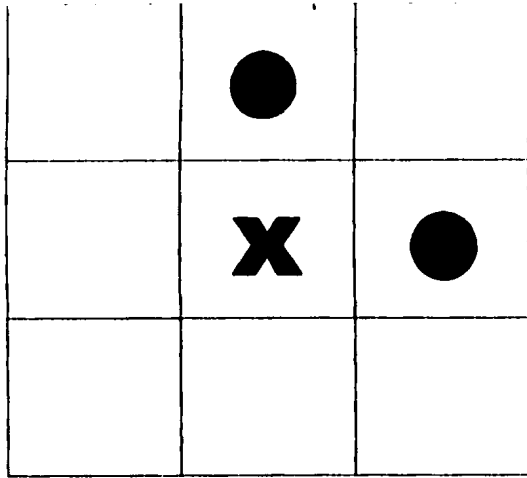
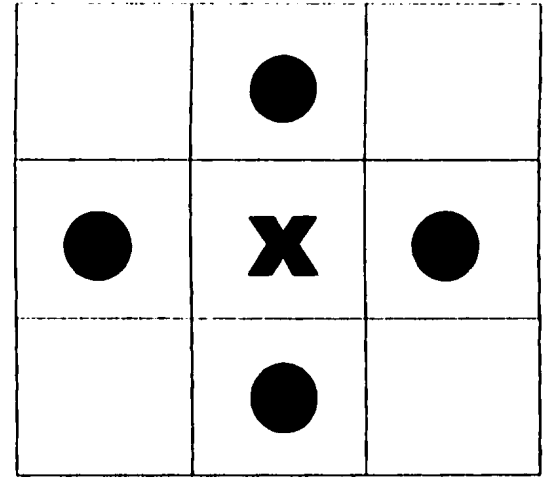


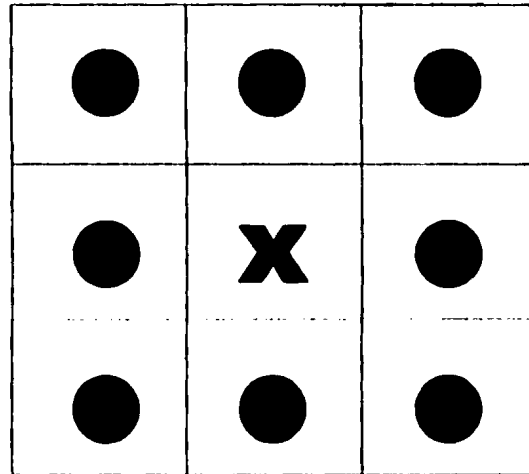
Figure 2.1: Examples of how correlation coefficients reflect geology using a one-trace comparison pattern.



2 Traces



4 Traces



8 Traces

Figure 2.2: Comparison patterns showing 2,4, and 8 traces. X is the trace to be compared to the surrounding traces ●

2.2.1 Cross-Correlation

Cross-correlation, as stated previously is a measure of the similarity between two data sets (Sheriff and Geldart, 1995). Comparison of the two data sets may show that one data set is time shifted by varying amounts relative to the other. These corresponding values of the two data sets are multiplied together, with the products summed to result in a value for cross-correlation. If the two sets are the same, the product will be positive and cross-correlation is large. If the two sets are not alike the products will contain positive and negative values and therefore the sum will be small. If the result is a large negative value it means that the two traces would be similar if the polarity of one of the traces was inverted (Sheriff and Geldart, 1995).

The algorithm used to compute a coherency result of the model and real data set for Hibernia was developed by L.R. Lines (1997) based on an unnormalized version of a formula in Marfurt et al., (1998). Marfurt et al., (1998) uses a normalized cross-correlation which compares the data in terms of inline and cross-line directions (figure 2.3). The in-line l-lag cross-correlation, ρ_x , at a time t between data traces, u, at positions (x_i, y_i) and (x_{i+1}, y_i) is expressed as:

$$\rho_x(t, \ell, x_i, y_i) = \frac{\sum u(t - \tau, x_i, y_i) u(t - \tau - \ell, x_{i+1}, y_i)}{\sqrt{\sum u^2(t - \tau, x_i, y_i) \sum u^2(t - \tau - \ell, x_{i+1}, y_i)}} \quad (2.3)$$

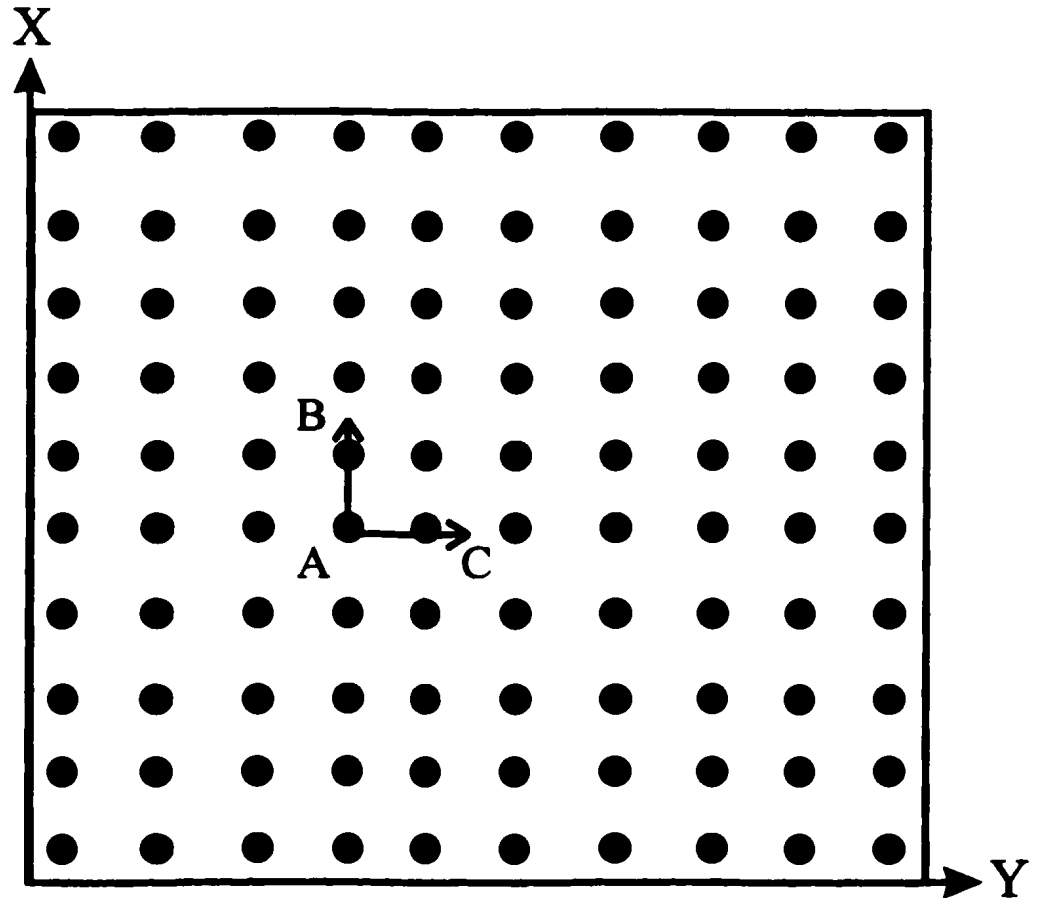


Figure 2.3: Coherency is measured by calculating seismic trace similarity in the in-line and cross-line directions

The cross-line m-lag cross correlation, ρ_y , at a time t between data traces, u, at positions (x_i, y_i) and (x_i, Y_{i+1}) is defined as:

$$\rho_y(t, m, x_i, y_i) = \frac{\sum u(t - \tau, x_i, y_i) u(t - \tau - m, x_i, y_i + 1)}{\sqrt{\sum u^2(t - \tau, x_i, y_i) \sum u^2(t - \tau - m, x_i, y_i + 1)}} \quad (2.4)$$

By combining the in-line (l-lag) and cross-line (m-lag) correlation coefficients a 3-D estimate of coherency, ρ_{xy} , can be generated:

$$\rho_{xy} = \sqrt{[\max \rho_x(t, l, x_i, y_i)] [\max \rho_y(t, m, x_i, y_i)]} \quad (2.5)$$

where, $\max \rho_x(t, l, x_i, y_i)$ and $\max \rho_y(t, m, x_i, y_i)$ denote those lags l and m for which ρ_x and ρ_y are maximum.

Landmark (1996) uses a similar formula for calculating normalized cross-correlation values (correlation coefficients) and is expressed as:

$$\phi(t, d) = \frac{\sum G_k H_{k+d}}{\sqrt{\sum G^2_k \sum H^2_{k+d}}} \quad (2.6)$$

where k is the time window and ϕ is the correlation coefficient calculated for any pair of traces, G and H, at time t, and dip d. This calculation is then repeated for every possible

dip within the search limits that have been set, with the highest correlation coefficient obtained being used as input for computing the continuity attribute. There are several continuity attributes, which could be used to statistically measure the range and variation in the correlation coefficients. Such attributes include the minimum, maximum, average, or median coefficient. Each correlation coefficient will tend to give different results when looking at structural areas, with maximum correlation values emphasising the largest local continuities. Minimum correlation values will emphasise the largest local discontinuities and the average or median will give a view of the representative data continuity. Since the goal for this project is to image faults, an average statistical measurement was used. These results are compared for their fault imaging abilities. Landmark software also depends on vertical window size (time window). This parameter specifies the length of the trace data to be used for each cross-correlation. A typical value to use is 20 to 100ms. Shorter window sizes give a measure to trace difference and are likely to be biased from noise. Longer windows reduce noise effects but because of a high degree of statistical averaging they can obscure subtle discontinuities Landmark, 1996).

2.2.2 Semblance

Semblance is described by Sheriff and Geldart (1995) as the ratio of the total energy of the stack within a gate of length $(l+m)$ to the sum of the energy of the component traces within the same time gate and is expressed as:

$$S_T = \frac{\sum (\sum g_{it})^2}{\sum \sum (g_{it})^2} \quad (2.7)$$

where S_T and g_{it} are the amplitude of the individual channel at time t . Therefore semblance will tend to be large for coherent events, but the magnitude of the semblance will be sensitive to the amplitude of the event. So strong events will exhibit large semblance and weak events will exhibit moderate values of semblance, whereas incoherent data will have very low semblance.

2.3 Difference Method

The difference method was developed by CPTC (1996) and is a very different technique than the coherence method. It is based on identifying local trace-to-trace differences (CPTC, 1996) by measuring the difference between seismic signals. If there is a change in the seismic signal due to faulting then the result will be a high difference value indicating a discontinuity.

Seismic signals are windowed segments of seismic traces and can be represented as vectors (Luo et al., 1996). Equation 2.2 shows how the difference between two seismic signals can be calculated. This equation assumes that there is a signal A on the target trace and signal B on an adjacent trace with d being the difference at the center sample of the window on the target trace (Luo et al., 1996). L.R. Lines has also coded an algorithm based on the difference method very similar to that of Chevron's difference method to be used to compute results using the model data and the real data sets. Results of both algorithms are shown.

The difference algorithm simply takes the difference of the seismic trace at a given depth, z with the average of its neighbours in the x and y direction. For example, if we consider the seismic trace at a grid point (i,j,k) in an x - y - z co-ordinate system, the difference trace at i,j,k is defined as the average of the absolute value of differences between the wavefield at a point and its neighbours.

$$\Delta U_{i,j,k} = 0.25 \left(|U_{i+1,j,k} - U_{i,j,k}| + |U_{i-1,j,k} - U_{i,j,k}| + |U_{i,j+1,k} - U_{i,j,k}| + |U_{i,j-1,k} - U_{i,j,k}| \right) \quad (2.7)$$

where $| |$ denotes absolute values. This type of differencing is very similar to second derivative maps, which are used to detect edges for potential field data.

In terms of finite differences, second derivatives are given by:

$$\nabla^2 U_{i,j,k} = \Delta X^{-2} \left[(U_{i+1,j,k} - 2U_{i,j,k} + U_{i-1,j,k}) + \Delta (U_{i,j+1,k} - 2U_{i,j,k} + U_{i,j-1,k}) \right] \quad (2.8)$$

so that in the case of positive differences for terms in (2.7), the second derivative measure would be equivalent to the difference map (to within a scale factor).

2.4 Geophysical Background

For the purpose of this thesis seismic data over the Hibernia field was used. The seismic data is a three-dimensional survey, which was shot in the spring-early autumn of 1991. The survey is 21 by 28 km in size, thirty fold with a 25 m common mid-point spacing and record length of 6 seconds with a 2 ms sampling rate. A small portion of the 1991 Hibernia seismic survey, was used to generate synthetic seismic data (figure 2.4). This synthetic seismic data as described in Kelly (1998) is 7420 m in the east-west direction and 5460 in the north-south direction. The model data consists of seven layers and the Murre fault as shown in figure 2.5. The seven-layer model consists of 180 x-points , 132 y-points, and 333 z-points.

The real data as outlined in figure 2.4 overlaps the model area. The data set consists of 310 inlines and 270 crosslines at a 25 m spacing. Both data sets will be used to test coherency and differencing algorithms coded by Lines. For testing of the software developed by Chevron and Landmark the same three-dimensional data set over the Hibernia field was used which consisted of 400 inlines and 300 cross-lines over the Murre fault at a 2730 time slice. The size of the data set was chosen for computation time.

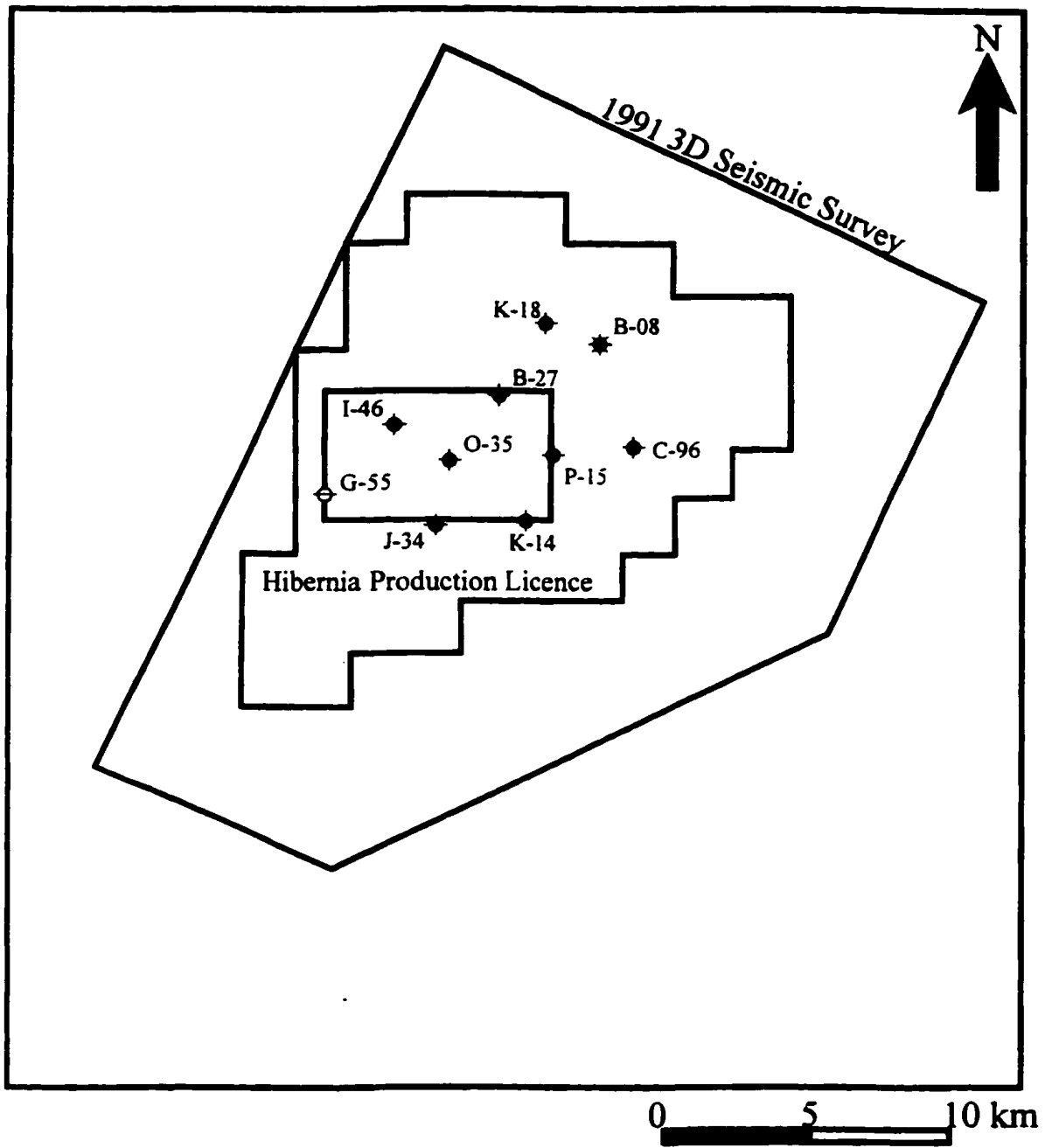


Figure 2.4: Illustration of the 1991 3-D seismic survey shot over the Hibernia field. Also shown is the well locations and an outline of the seismic area used for the model data (black rectangle). Adapted from Kelly (1998).

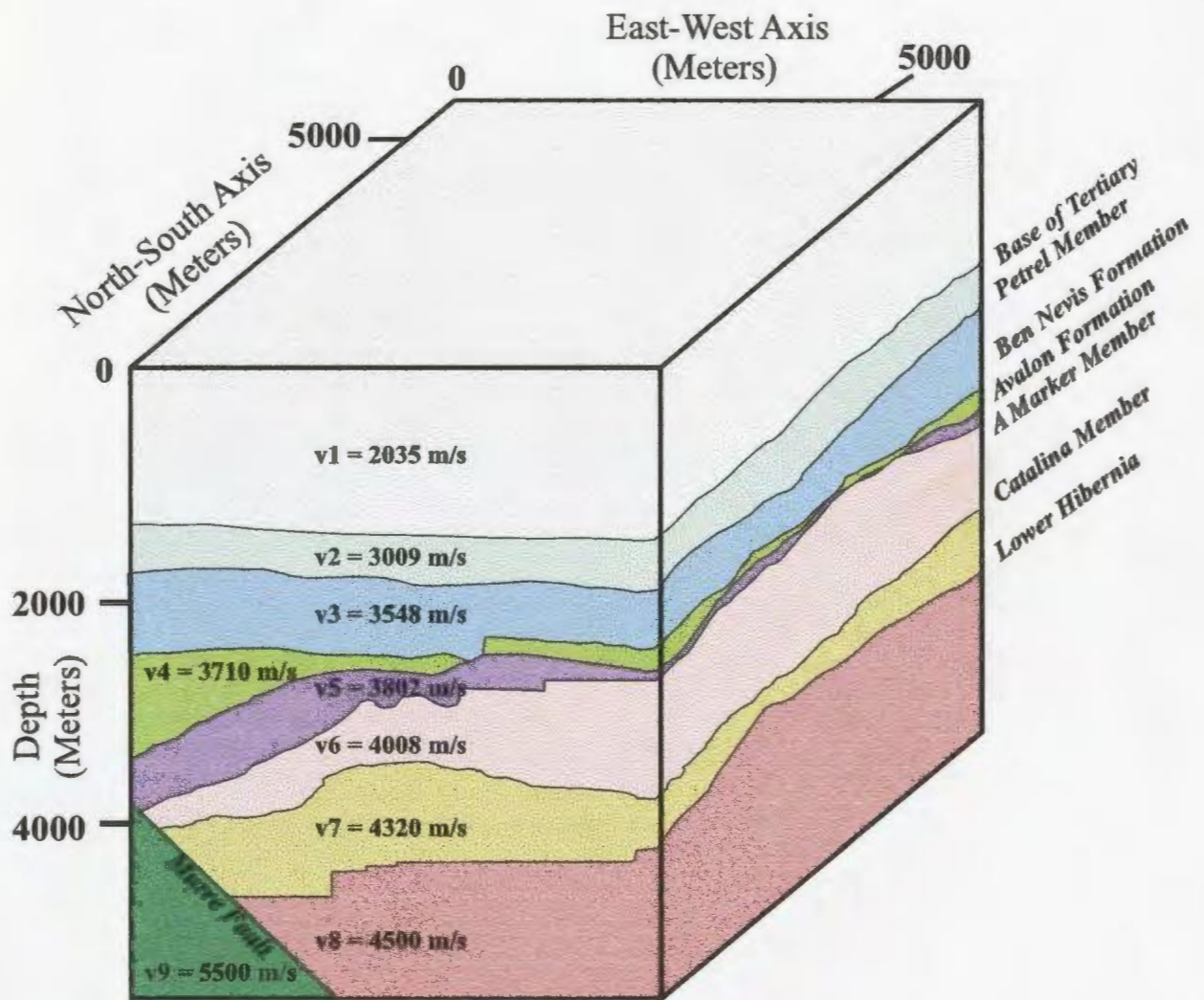


Figure 2.5: Complex Hibernia model consisting of seven stratigraphic layers and the Murre fault (modified after Kelly, 1998).

CHAPTER 3

REGIONAL GEOLOGY OF THE JEANNE d'ARC BASIN

3.1 Tectonic History

During Palaeozoic times the basement underlying the present day Mesozoic strata was located at the centre of Pangea (Tankard et al., 1987), with the Mesozoic strata deposited through a convergence and ocean closing event. The Jeanne d'Arc Basin of the Grand Banks was formed by three major episodes of rifting associated with opening of the Atlantic Ocean. This occurred during Triassic through Cretaceous time (PetroCanada, 1996). Each of these rifting phases had an associated period of passive subsidence (Tankard et al., 1987). The result was the formation of one of several Mesozoic extensional-sag cratonic margin basins, including the Jeanne d'Arc basin, underlying the Grand Banks of offshore Newfoundland. Figure 3.1 illustrates the location of basins that formed during deposition of Mesozoic-Cenozoic sedimentary succession, with the Jeanne d'Arc Basin being approximately 20 km in thickness and covering an area greater than 10,000 km² (Arthur et al., 1982). The basin is thought to be fault bound and plunges in a north-eastward direction. Deposition of the major source rocks and hydrocarbon-bearing reservoir intervals occurred during subsidence phases.

The first phase of rifting spanned Late Triassic through Early Jurassic times. This event resulted in the separation of Nova Scotia and Africa. A second phase of rifting occurred during Late Jurassic to earliest Cretaceous times. During this rifting phase, extension resulted in the separation of the southern Grand Banks and southern Iberia. The third phase of rifting occurred during mid-Aptian to Late Albian time. Separation of

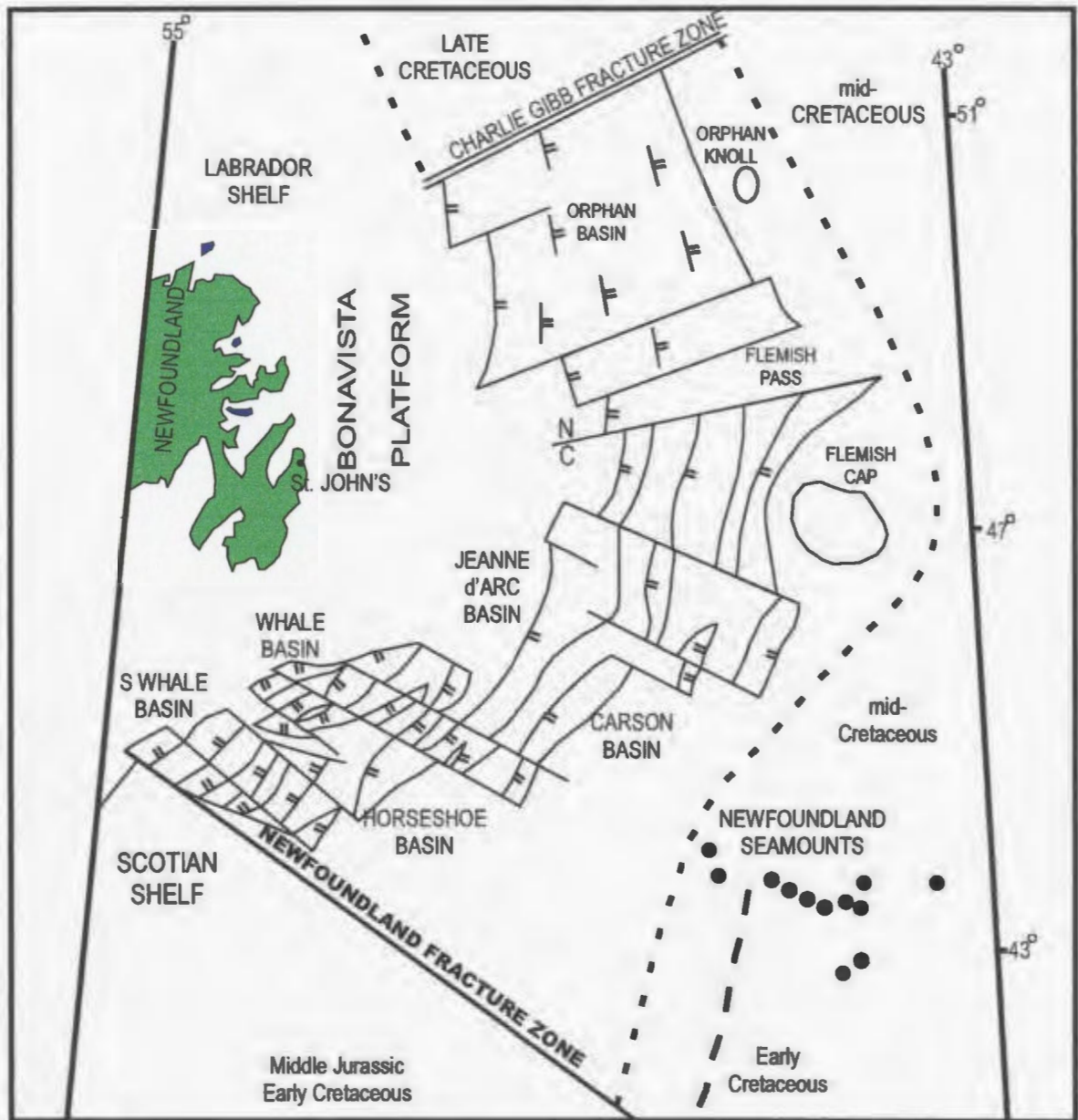


Figure 3.1: Location of basins that formed during deposition of Mesozoic-Cenozoic sedimentary succession.

the central Grand Banks from the Northern Iberian margin and the British Isles occurred during this rifting phase.

Figure 3.2 illustrates several interpretations for the timing, type, and range of the third rifting event (Sinclair, 1993a). Re-activation of major basin faults in the Late Cretaceous and Early Tertiary may have been caused by extension which occurred when the Norwegian-Greenland Sea opened. This may be considered as a fourth phase of rifting. Since Late Cretaceous the Grand Banks has formed part of a passive margin.

3.2 Regional Structure

Structural analysis of the Jeanne d'Arc Basin is based on seismic interpretation and well data information, with the timing of deformation based on biostratigraphic analysis and stratigraphic geometries. Three periods of structural events formed the basis for the structural shape of the Jeanne d'Arc Basin. The first structural event occurred during Late Triassic to Early Jurassic. During this time a large half-graben was created giving the shape of the south and central areas of the basin (Tankard et al., 1987). Extensional basin forming faults, such as the Murre and Mercury faults, as well as northeast trending listric synthetic and antithetic faults, also formed. These northeast trending faults are said to either offset or terminate against transfer faults thus giving the basin margin a regular orthogonal pattern (PetroCanada, 1996) (figure 3.3). This period is difficult to decipher since later extensional events tend to overprint structural trends formed during the Late Triassic to Early Jurassic age (Mackay et al., 1990).

The second structural event occurred during Late Jurassic to Early Cretaceous when extension formed the structural shape of the basin (Arthur et al., 1982). Uplift of a broad region (Avalon Uplift) in the southern part of the basin occurred during this time

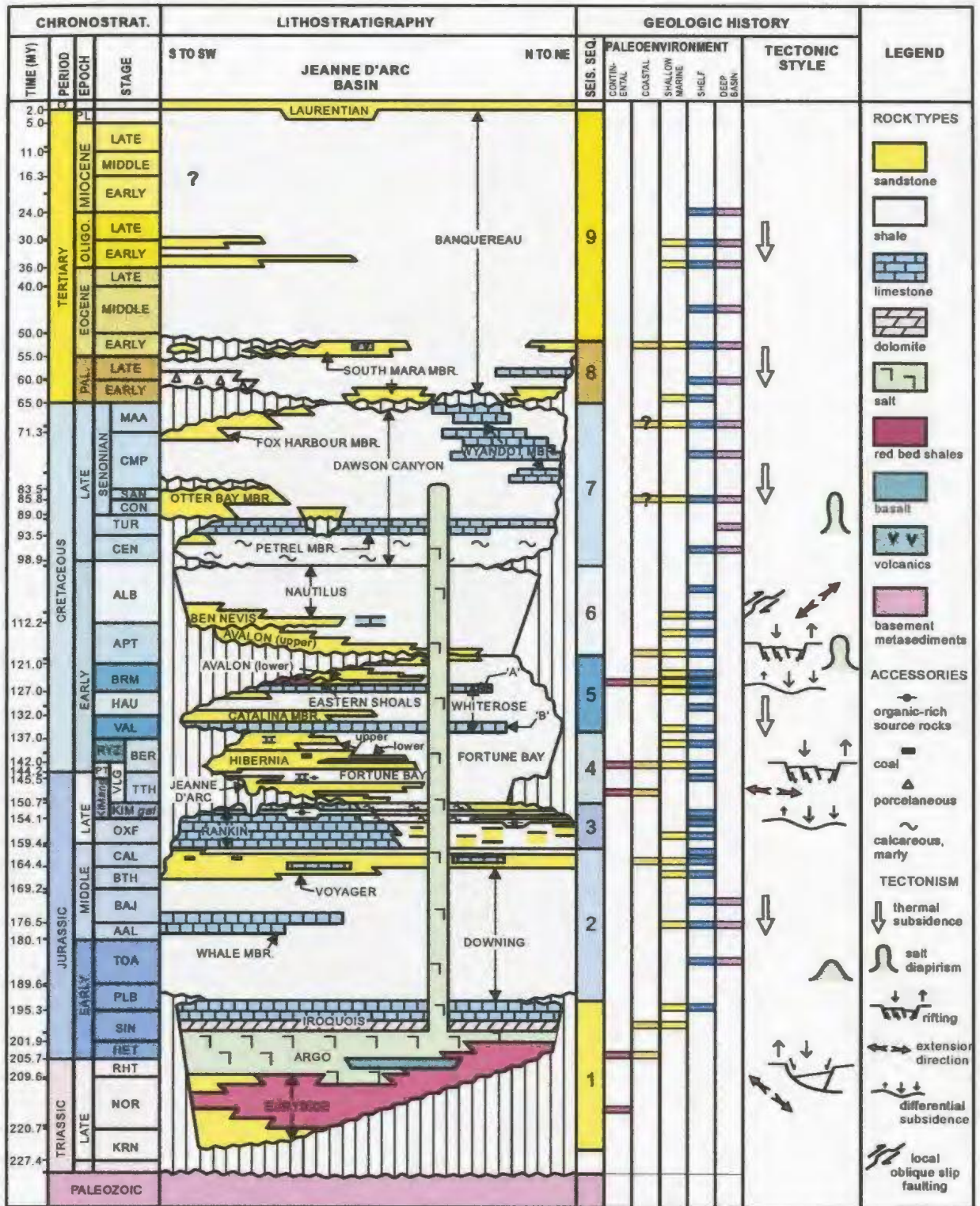


Figure 3.2: Lithostratigraphic section of the Jeanne d'arc basin from Sinclair (1994).

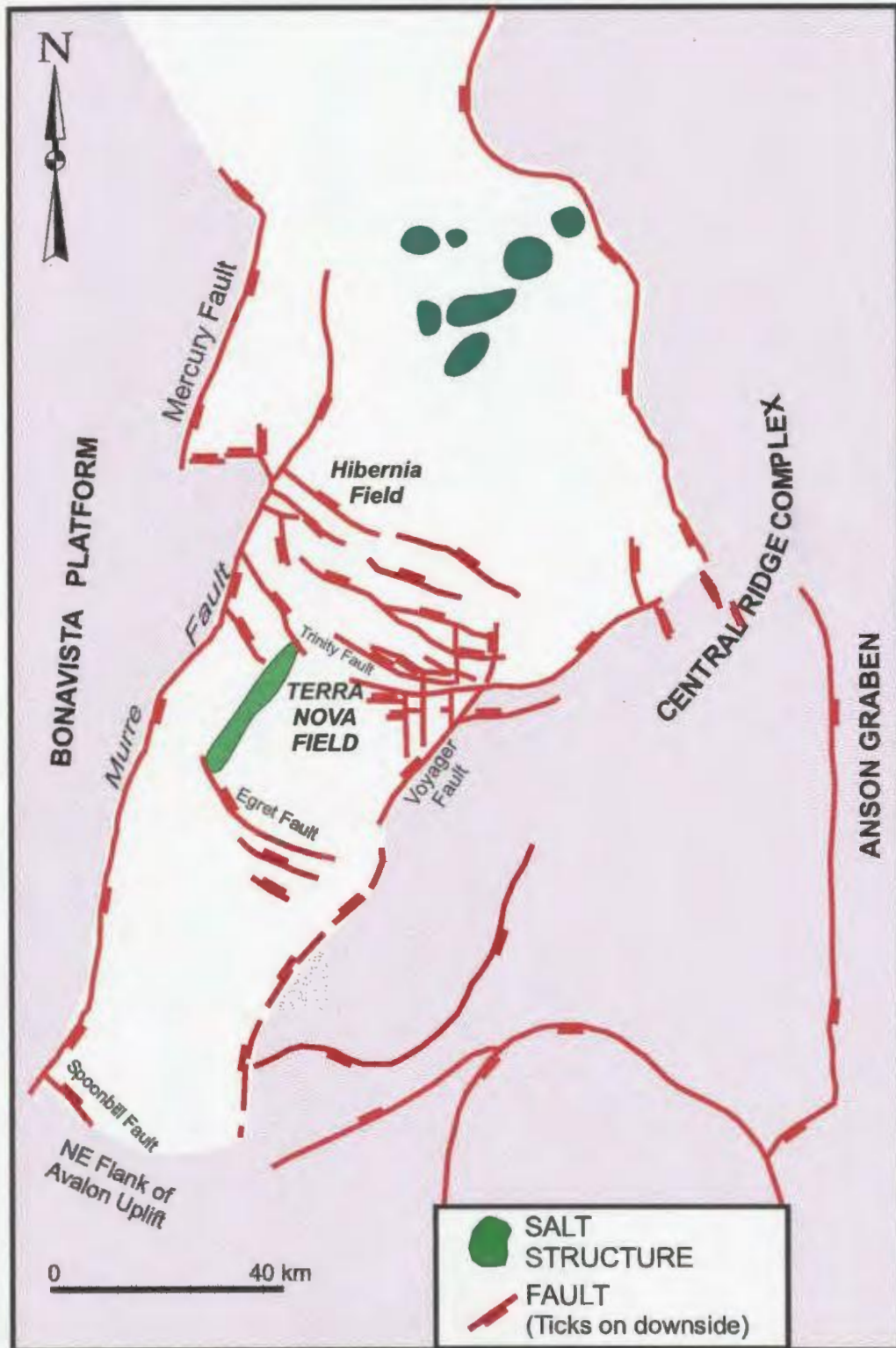


Figure 3.3: Structural shape of the Jeanne d'Arc basin.

(Mackay et al., 1990). This uplift also developed North-South-oriented faulting which is characteristic of the central Jeanne d'Arc Basin and Central Ridge (Figure 3.3).

The third structural event involved the growth of a series of Northwest-Southeast oriented normal faults. These normal faults are thought to have initiated in mid-Aptian and terminated in the Late Albian. Mackay and Tankard (1990) have interpreted that most of the normal faults oriented Northwest-Southeast that occurred in the Albian were related to salt tectonics. Regardless of their origin, the Northwest-Southeast faults experience detachment at different levels within the sequence. Detachment zones occur between basement and sedimentary infill, within basement, between carbonates and clastics, within salt, and within thick ductile shales (Arthur et al., 1982). These faults form excellent hydrocarbon traps by forming such structures as horsts, grabens, tilted fault blocks, rollovers, and reverse drag folds. The occurrence of local salt diapirism and re-activation of some of the major faults such as the Murre, Voyager, Trinity and Egret mark the end of significant tectonic activity in the Basin (figure 3.3).

3.3 Hibernia Structure

The Hibernia structure, located 315 km south-east of St. John's, Newfoundland (figure 3.4), is characterized by extensional faulting and a rollover anticline that was formed due to salt diapirism. The Murre Fault is a major listric growth fault that bounds the western side of the field as shown in figure 3.5. It is offset by the Nautilus fault, which extends along the Northeast boundary of the field (figure 3.5). The Hibernia field is dissected by a series of smaller scale faults which in turn dissect the area into a number of separate blocks via transfer faults (Arthur et al., 1982).

Several small scale faults have a major effect on the thickness of several stratigraphic sequences, and some faults completely offset the principal Hibernia reservoir. Therefore, the current strategy for depletion of the field will be on a block-by-block basis, assuming faults are sealing the hydrocarbons (Hurley et al., 1992).

3.4 Regional Stratigraphy

Regional stratigraphy of the Jeanne d'Arc Basin is dominated by terrigenous clastic deposition. The type of depositional environment is thought to be fluvial and nearshore marine (Tankard et al., 1987). Sinclair (1993a) illustrates lithostratigraphy of the Jeanne d'Arc Basin as shown in figure 3.2. The earliest record of deposition within the basin, which can be observed through seismic imaging and by well penetration in the southern extents of the basin, are the Eurydice, Argo, and Iroquois formations. These are upper Triassic to Lower Jurassic continental redbeds, restricted-marine evaporites, and carbonates (Arthur et al., 1982). A thick post-rift succession of Lower to Middle Jurassic marine mudstones and carbonates of the Downing Formation (Sinclair 1988) overstepped the syn-rift succession of the Eurydice, Argo, and Iroquois formations. The overlying Voyager formation consists of Middle Jurassic marine shales and siltstones, which are conformably overlain by the Rankin Formation. The Rankin Formation is an 800m thick succession of thin bedded marine limestone, mudstone, shale, and siltstone (Sinclair, 1988). Near the top of the Rankin Formation is the Egret Member, which is the source rock for the Hibernia field. The Jeanne d'Arc Formation consists of porous sandstones and a non-reservoir conglomerate and shaly unit. Offshore marine shales of the Fortune Bay Formation overstep these rocks which provide the top seal of

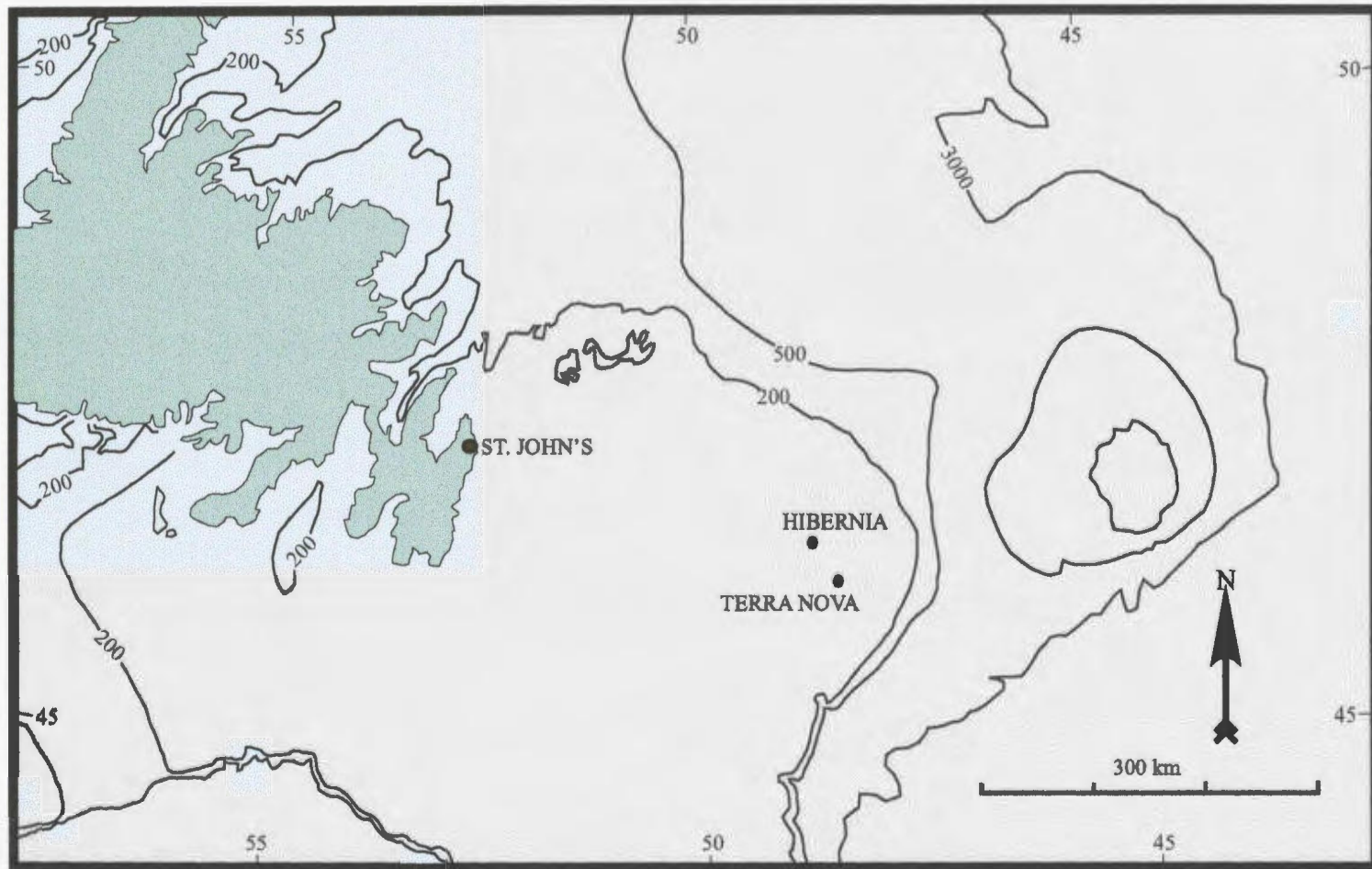


Figure 3.4: Location map of the Hibernia field.

46°50'N

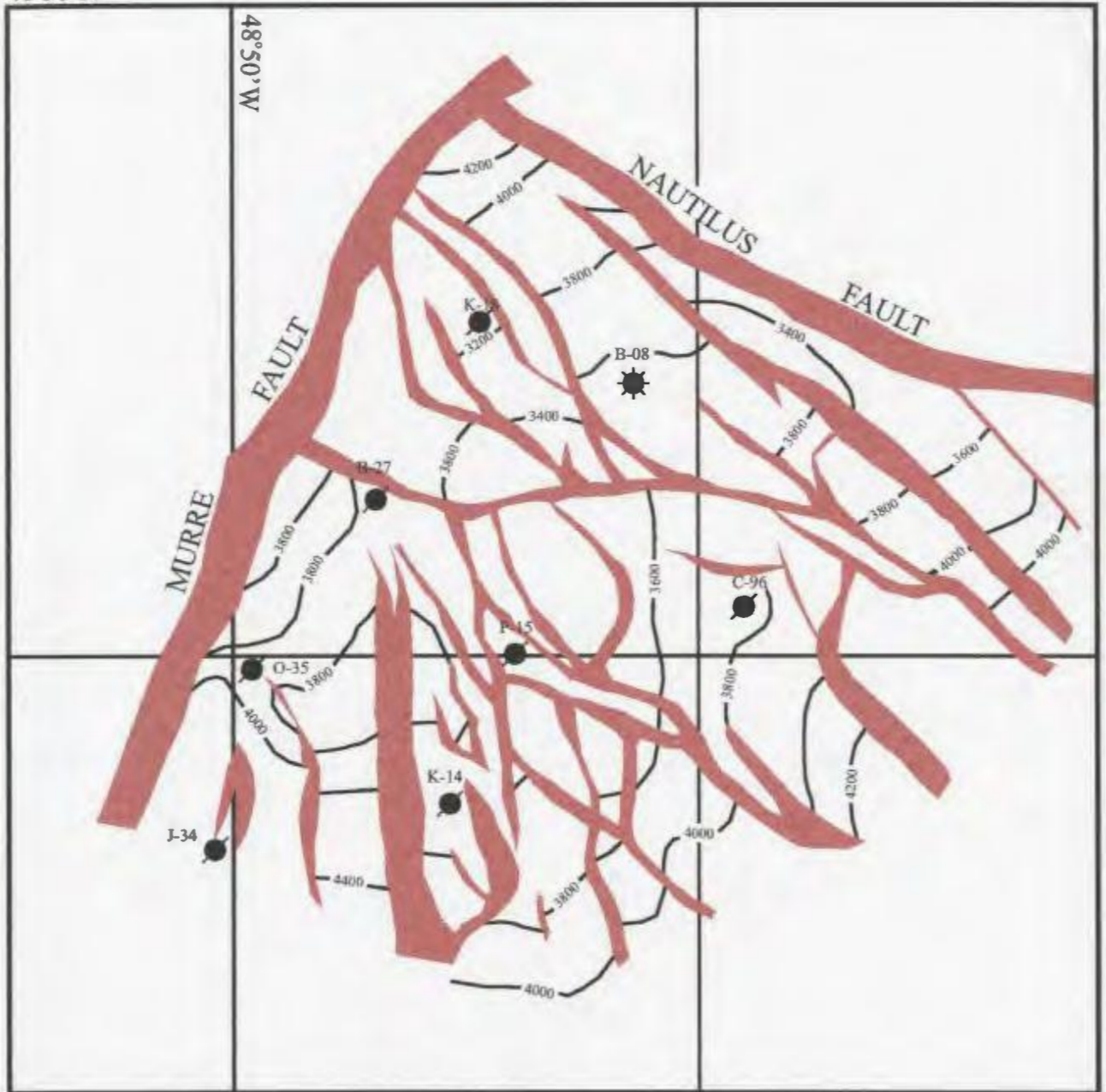


Figure 3.5: Hibernia structure shown at the Hibernia sandstone depth.

the Jeanne d'Arc Formation hydrocarbons (Sinclair, 1994). Similar to the Jeanne d'Arc Formation, the Hibernia Formation is comprised of deltaic sandstones and shales. The Aptian unconformity occurs between the Avalon and Ben Nevis Formations and above the Hibernia sandstones. These formations represent very good to excellent reservoir rocks, but they are also mostly wet. The Aptian Unconformity marks the end of rifting and transition into a passive margin. A thick sequence of Tertiary marine shales, minor chalk, and occasional sandstones are the youngest rocks in the field (Sinclair, 1988).

Chapter 4

Model Studies

4.1 Comparison of Coherency measures applied to unmigrated and migrated data

The quality of edge detection images is related to the quality of the input seismic data (Marfurt et al., 1996). Therefore to obtain faults as discontinuous features they have to be properly migrated into their correct sub-surface location. Undermigrated faults will produce diffractions and be relatively coherent events (Marfurt et al., 1996). Therefore to determine if the seismic data should be migrated before input into edge detection and coherency algorithms, comparison tests were performed on a simple extensional fault model (figure 4.1). Migration is an important part of the processing of seismic data, as it repositions data to its correct subsurface location. There are several seismic migration techniques, available. The type of migration one chooses to use is determined by factors such as type of data (structural verses flat), complexity of velocity distribution, objective of migration, data quality, computation time, computer memory, and cost. For the model data a reverse-time migration was used as determined by Kelly (1998). Reverse-time migration is a depth migration in the space-time domain (McMechan, 1983; Baysal et al., 1983; and Whitmore 1983). The model itself (figure 4.1) consisted of two stratigraphic layers with velocity $V_1 = 2500$ m/s and $V_2 = 3500$ m/s. The extensional fault had a throw of 400m and is at vertical position 1000 m to 1400 m, it also has a grid spacing of 20 m and $\Delta t = 2$ ms.

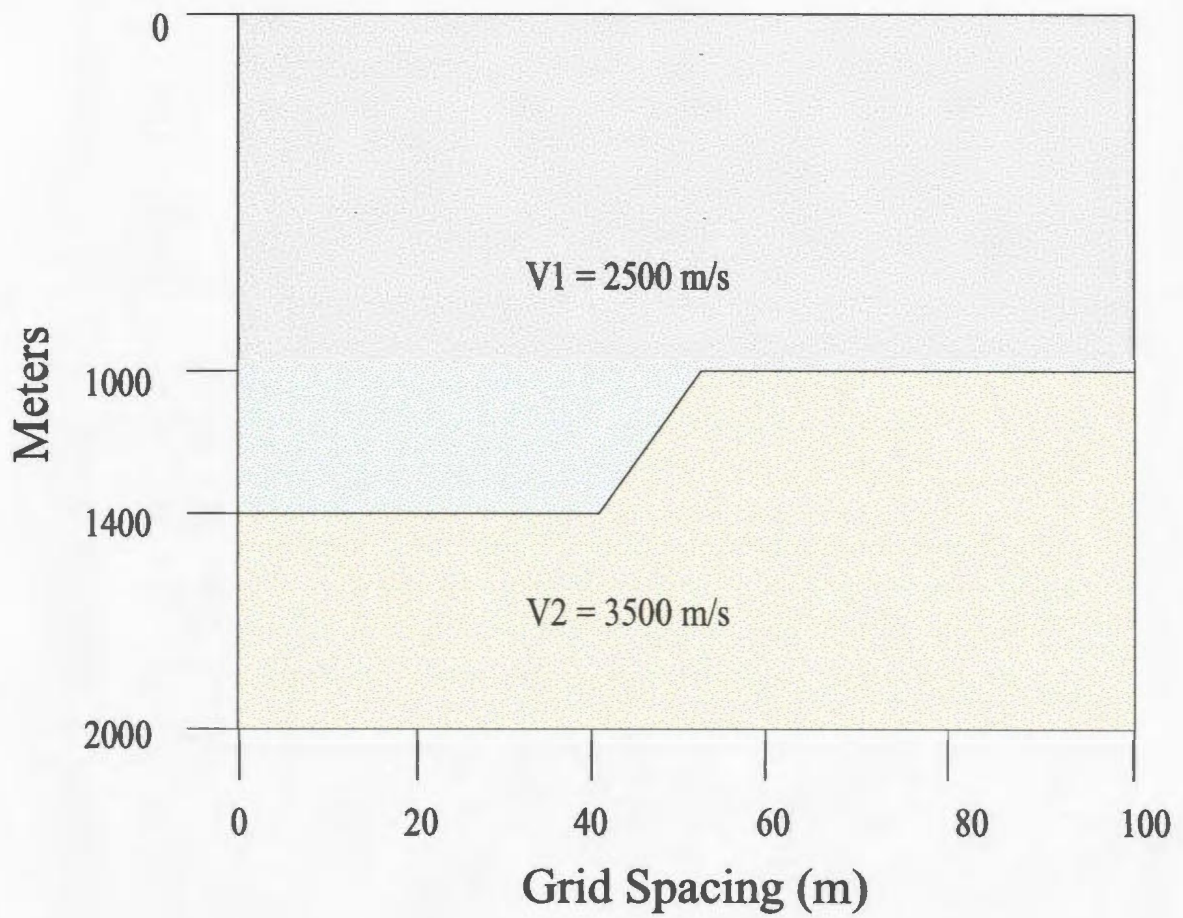


Figure 4.1: Simple extensional fault model which consists of two stratigraphic layers with velocities $V1 = 2500$ m/s and $V2 = 3500$ m/s with a throw of 400 m and the fault.

Depth migration is useful for structural data since it produces a section and takes into account the lateral velocity variations caused by faulting. Most time migrations do not consider lateral velocity changes and can therefore produce sections that have incorrect fault positioning. Figure 4.2 illustrates an unmigrated section of the fault model created by the model in figure 4.1, applying a finite difference code to create the synthetic seismogram. Using the same fault model figure 4.3 illustrates the result of applying a reverse time migration on the synthetic seismogram. This provides a window into the differences between migrated and unmigrated data. The position of the fault for the migrated data is at 1000m to 1400m with a 400m throw as in the model. Alternatively, the fault of the unmigrated time data in Figure 4.2 has considerable diffraction energy that obscures the fault position. Therefore, it is easier to interpret the migrated data as compared to the unmigrated data. This example is similar to real seismic fault reflections shown by Tucker and Yorston (1973).

Next both the migrated and unmigrated data are used as input into the differencing algorithm with the following results achieved. Figure 4.4 illustrates the differencing result of the unmigrated data as compared to the input data. For the unmigrated data, the result show that the differencing algorithm did not produce a result that defined the correct position of the fault (as shown by arrow), however it is easier to interpret than the input data. The resultant section does define the top and bottom of the stratigraphic layers, but it is still difficult to interpret the correct position of the fault.

Finally, figure 4.5 illustrates the differencing result of the migrated data as compared to the input data. This produces a result that adequately images the fault.

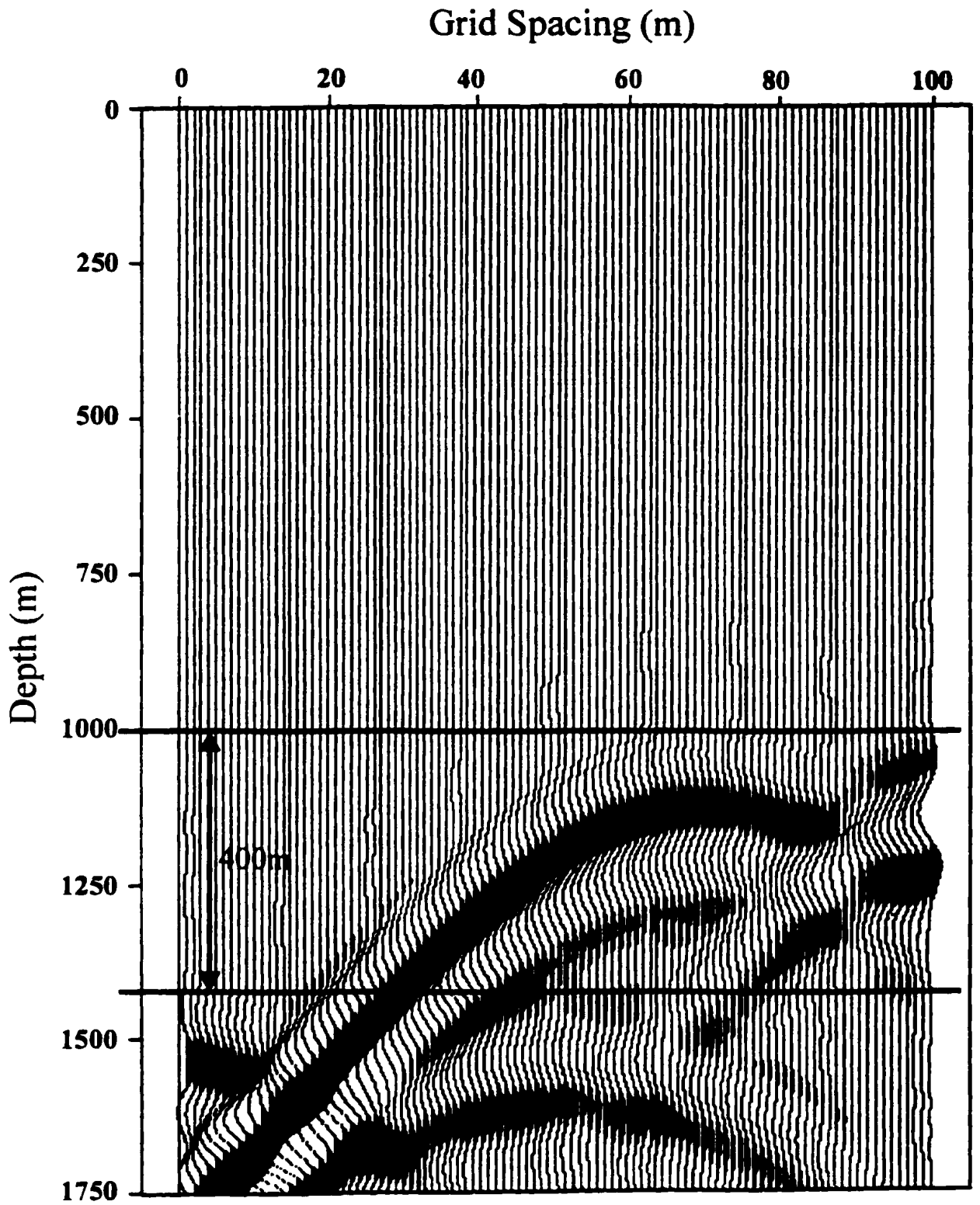


Figure 4.2: Unmigrated section of the fault model created using finite difference code. Fault throw is 400m.

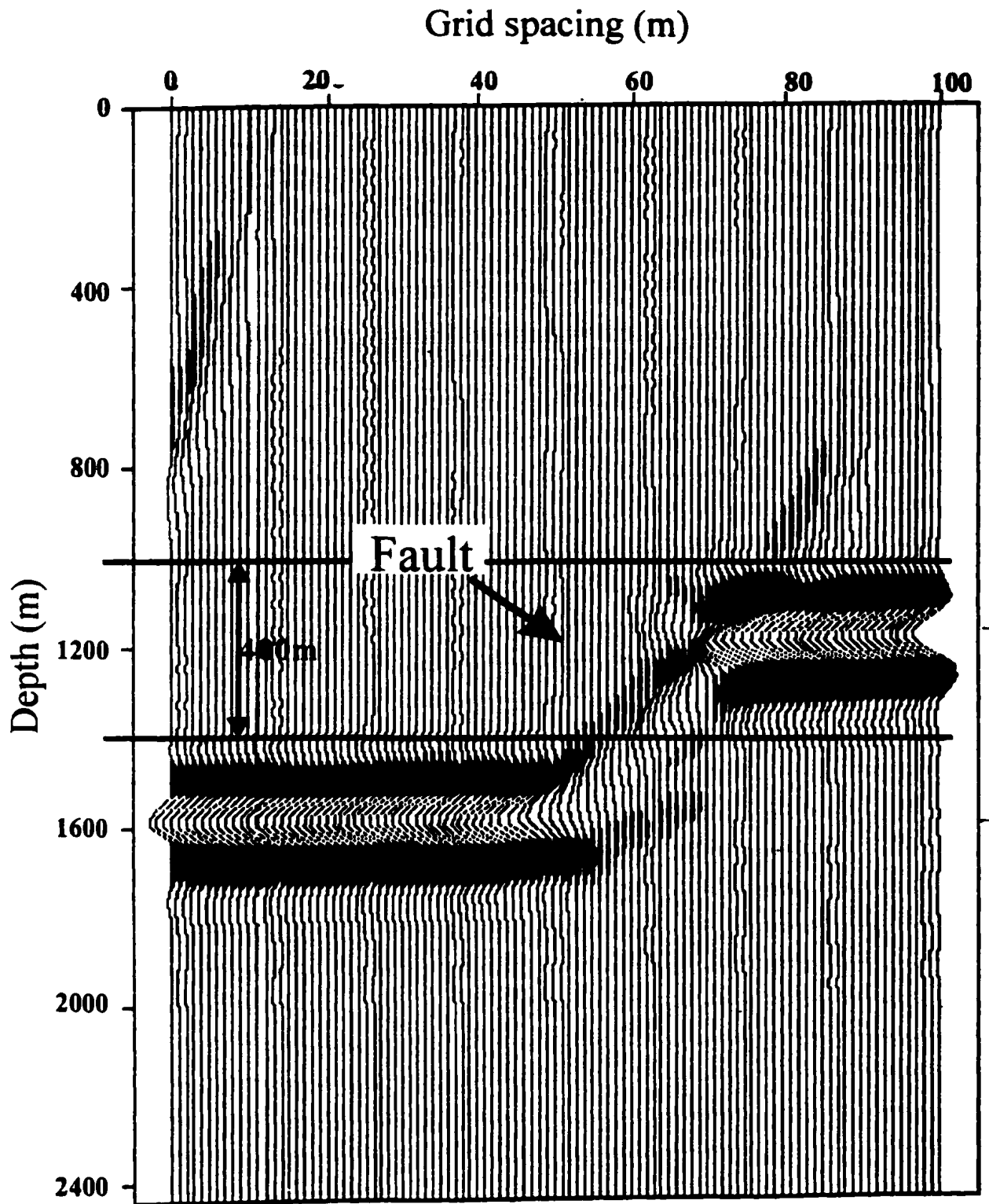


Figure 4.3: Migrated section of the unmigrated synthetic seismic.

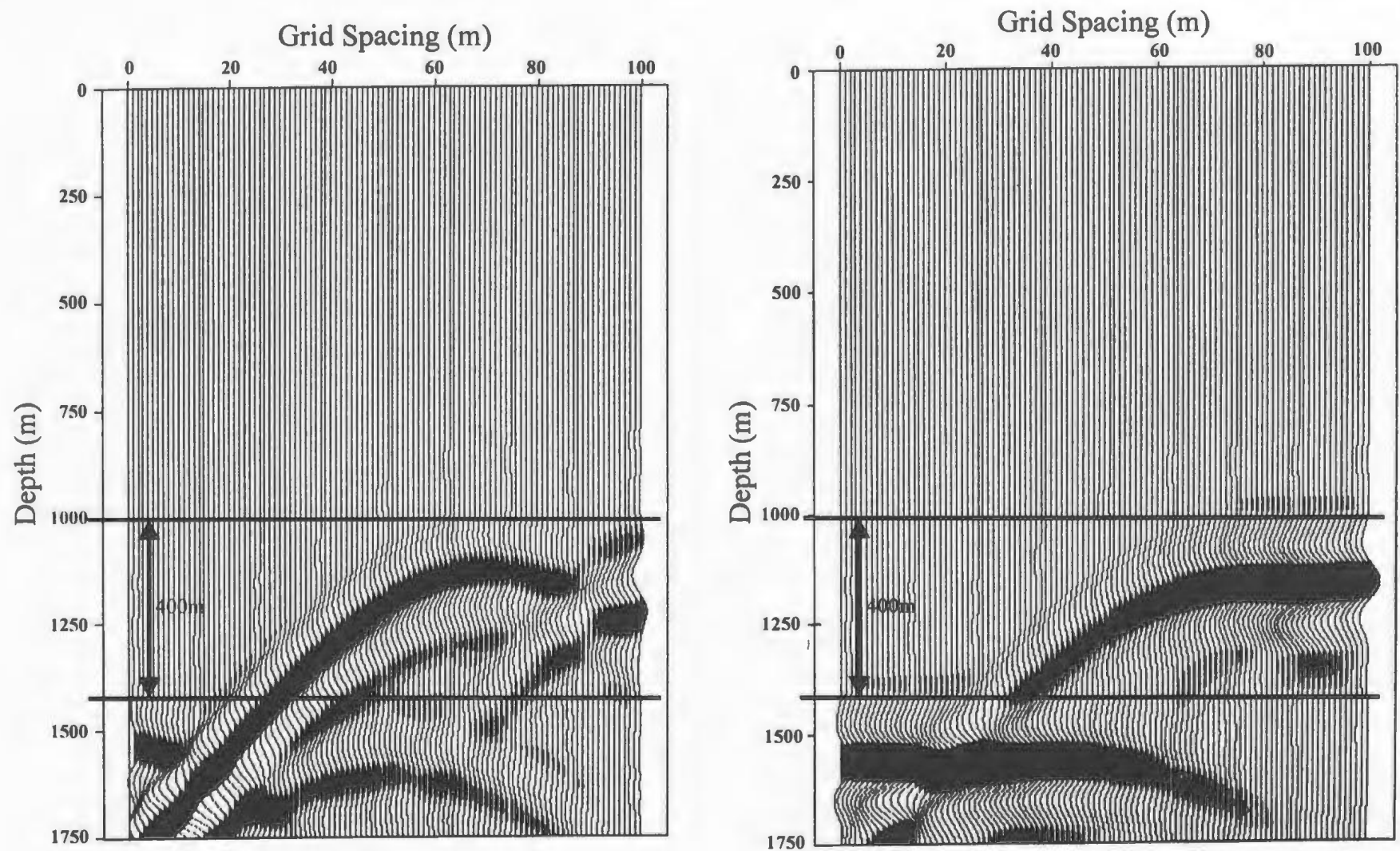


Figure 4.4: Differencing result of the unmigrated data (B) as compared to unmigrated model input (A).

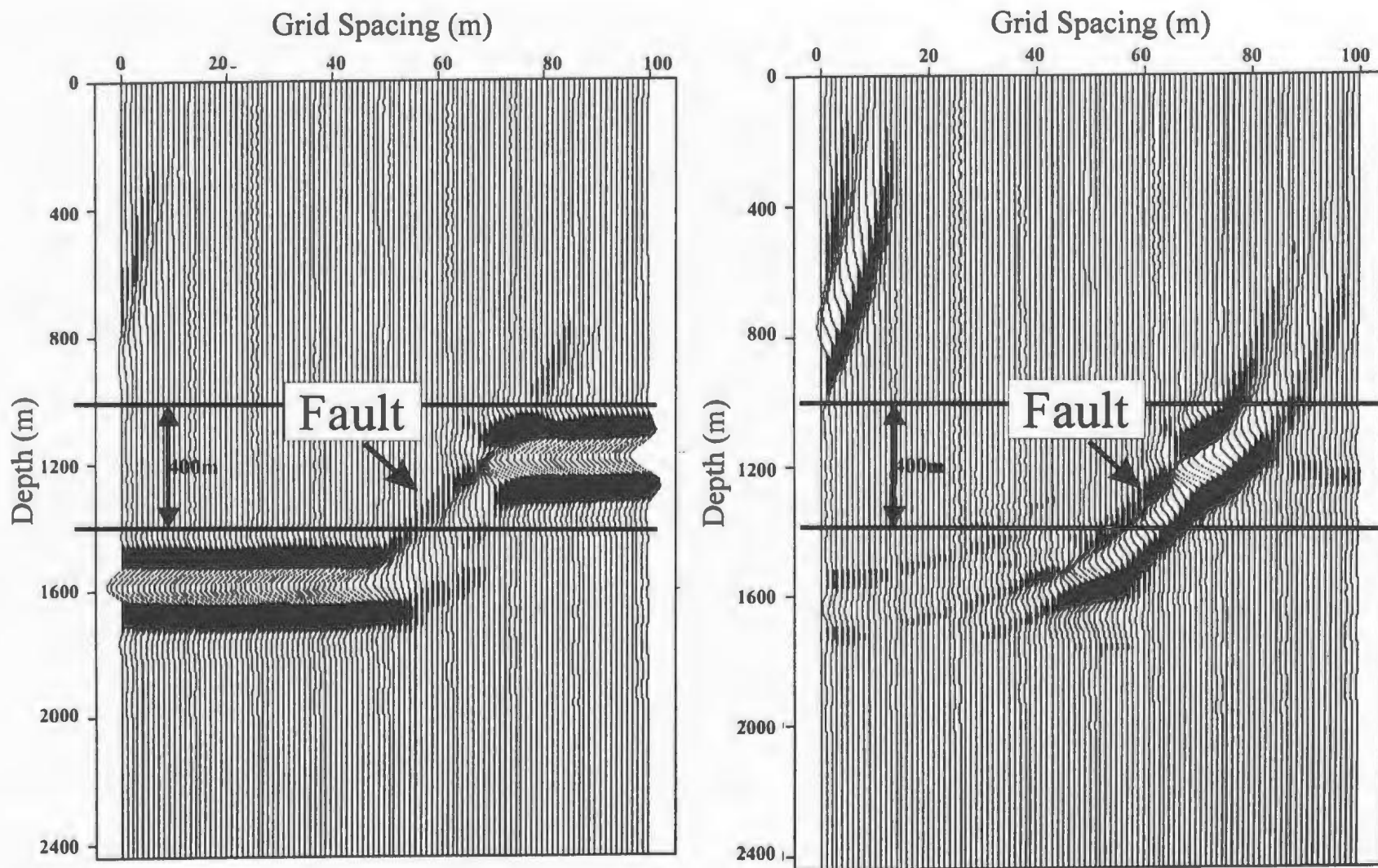


Figure 4.5: Differencing result of the migrated data (B) as compared to migrated model input (A).

There are some oscillations, although if you look at the first continuous reflections the fault is positioned at 1000m to 1400m as the model data. The artifact from 400-800m at the left hand side are due to edge effects. The other strong continuous reflections are oscillations caused by the finite length of the wavelet. Differencing causes phase changes in the wavelet, which can be remedied by deconvolution.

From the result shown above it is evident that migration is an important factor in the correct positioning of faults prior to using fault detection methods. Therefore for the purpose of this thesis all model data will be migrated using a reverse time migration.

4.2 Description of 3D Model

The 3D Hibernia model was provided by Kelly (1998) and was used for modeling and migration of seismic data as shown in figure 2.2. The size of the model was determined by computation time and memory capacity (Kelly, 1998). A portion of the 1991 Hibernia seismic survey was used to generate the synthetic seismic data (figure 2.3). Hibernia Management Development Corporation (HMDC) supplied depth information of the seven horizons and the Murre fault. The model area is 7420 m in the east-west direction and extends to 5460 m in the north-south direction. Depth information was provided for Base of Tertiary Unconformity, Petrel Member, base of the Ben Nevis Formation, base of the Lower Avalon and top of the Lower Hibernia zone. For complete description of model layers see Kelly (1998). The interval velocities of the layers were determined using checkshot information from the wells in the study area as shown in figure 2.3. The seven-layer velocity depth model contained 180 x-points, 132 y-points and 333 z-points. A finite difference code was then used to create synthetic

seismic of the depth model, which was then used for reverse-time migration. It is this reverse-time migration result that was used to test fault detection and coherency methods.

4.3 Testing of Methods

This section explains results of each of the methods using the same data set. This includes description of the results and qualities of each method. Detailed comparisons between the methods are in the following section. Input for each method consisted of horizontal depth slabs and a vertical depth section of the reverse-time migrated model. Figure 4.6 illustrates a vertical depth slice of the reverse time migrated model data. From this we can see the seven stratigraphic layers as well as the Murre fault represented by a dashed line. For all figures in chapter four correct positioning of the Murre fault is illustrated by a dashed line. There is also another feature at position $z=175$ and $x=120$, which is a stratigraphic change as seen from the model. By examining the vertical section, several horizontal sections were chosen based on structural changes seen in the data at $z=175$, 215, and 250. Figure 4.7 shows a plane through the model data at depth position 215, which corresponds to a depth of 4300m. This depth was chosen since it would intersect the top of the Murre fault. Figure 4.8 illustrates a horizontal depth slab further down the Murre fault at depth position 250, which corresponds to a depth of 4750m. The other depth slab which will be used for testing the algorithms will not include the Murre fault but does illustrates a stratigraphic change at depth position 175 or 2500m (figure 4.9). These input depth sections (175, 225, and 250) will be used for testing the methods of coherency, differencing, and second derivatives. The results of this testing will be shown in the following sub-sections.

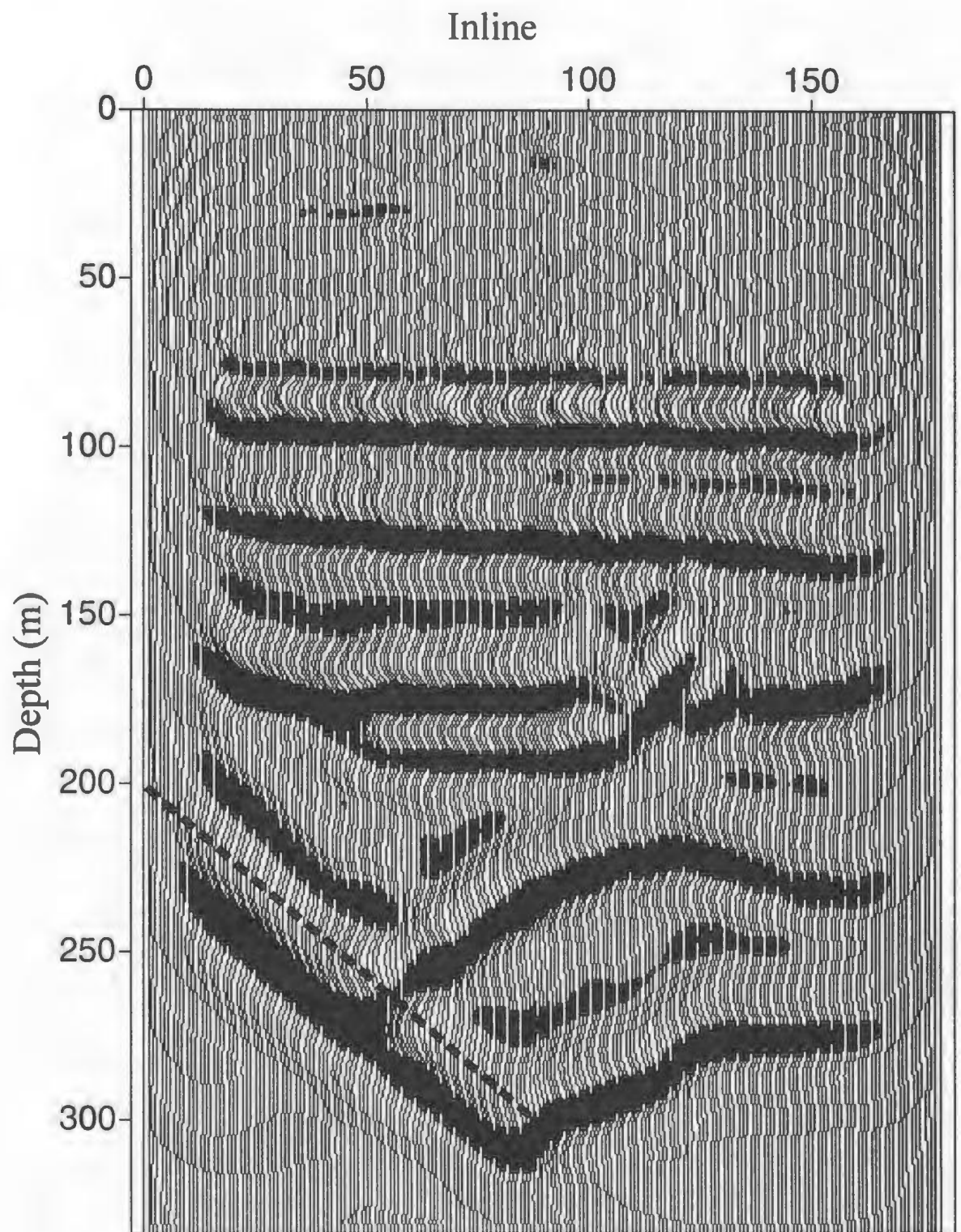


Figure 4.6: Vertical section through model data at line 60. Dashed line represents fault interpretation.

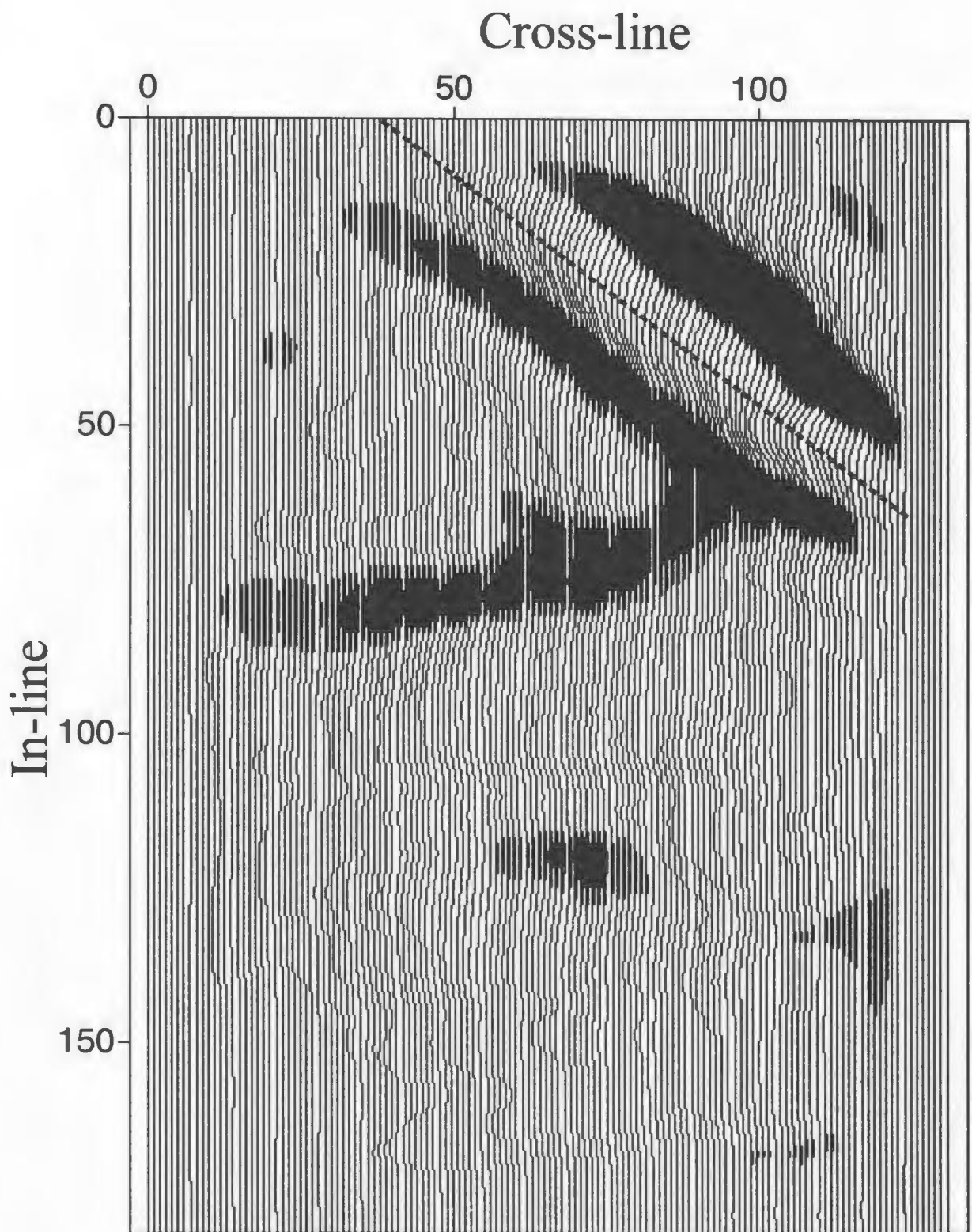


Figure 4.7: Plane through model data at depth position 215 which corresponds to a depth of 4300 m. Dashed line represents fault location.

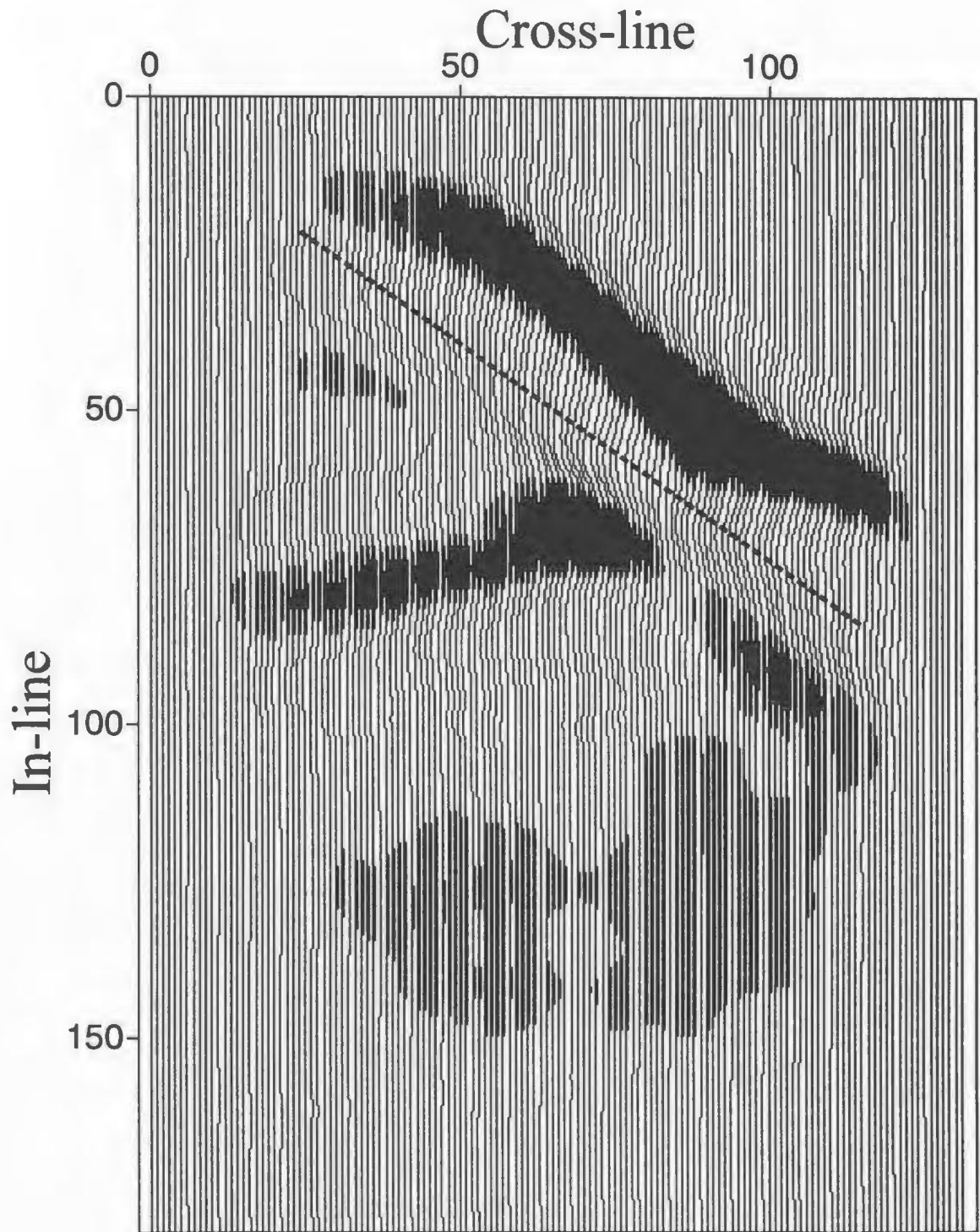


Figure 4.8: Plane through model data at depth position 250, which corresponds to a depth of 4750 m. Dashed line represents fault location.

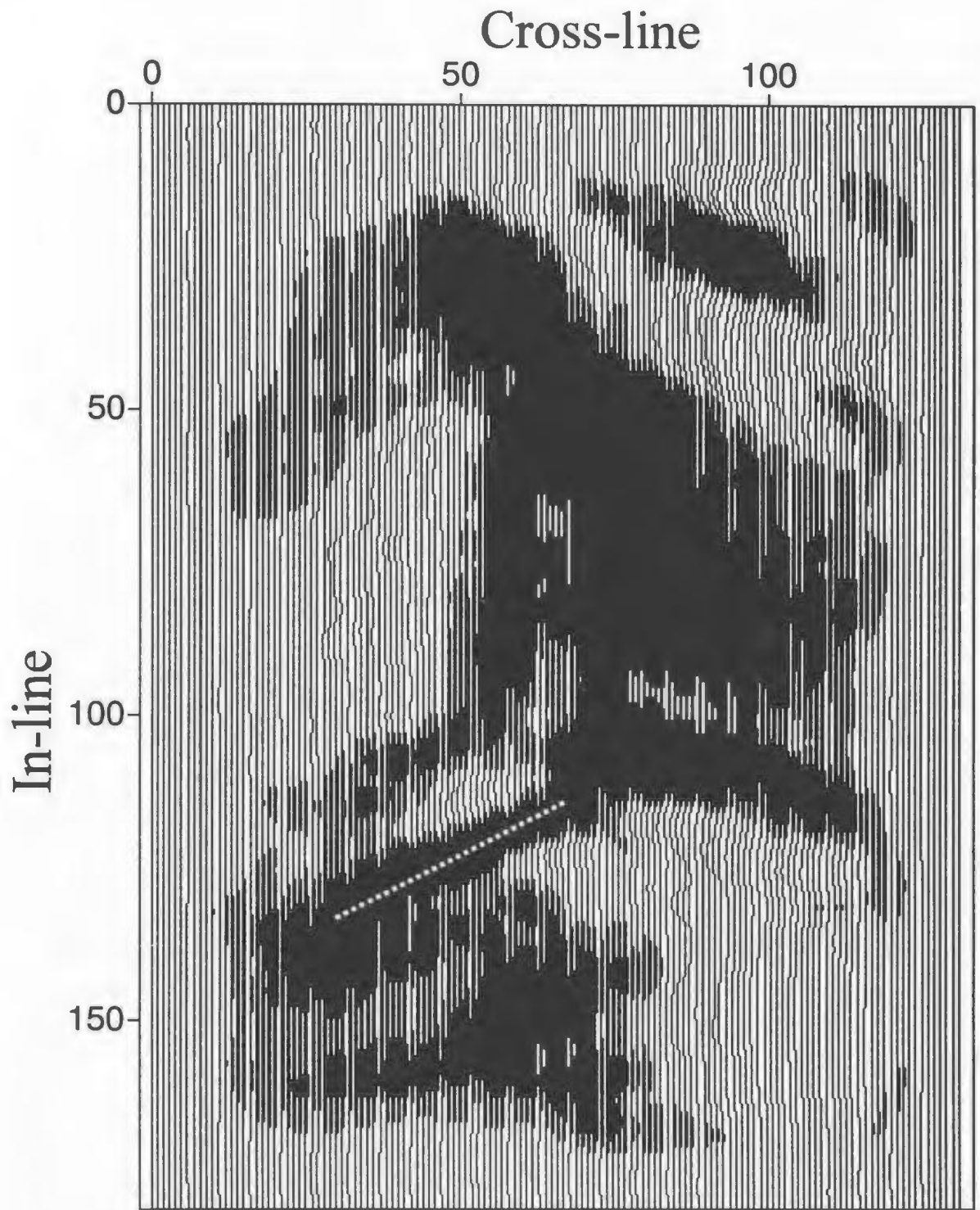


Figure 4.9: Plane through model data at depth position 170, which corresponds to a depth of 2500 m. Dashed line represents stratigraphic feature.

4.3.1 Coherency Result

Next applied to the input data was the coherency algorithm that was developed by Lines for the purpose of this thesis. This algorithm computes cross-correlation between the adjacent rows and then the adjacent columns, resulting in the average cross-correlation of the rows and columns as output. The result of the depth slice at $z=215$ is shown in figure 4.10. These results show that there are two continuous lines of discontinuity that are found in the area of the fault plane as compared with the input. The lower discontinuity is at the correct position of the fault plane, whereas the top one may be caused by wavelet size or there may be some residual energy. There are also very weak areas of discontinuity at $y = 100$ and 125 . These are caused by to stratigraphic changes in the geology rather than faulting since no faults are present in that area of the model.

The next depth that was used as input occurs at $z=250$ (figure 4.8). This input illustrates that the Murre fault has moved eastward due primarily to the fact that we are moving down the fault plane. Also present is an interesting feature that depicts the rollover anticline terminating against the Murre fault. The coherency result shown in figure 4.11 illustrates that the algorithm places the fault in its correct position, however it is not continuous and seems to pinch out. Again the continuous line of discontinuity is observed as in the previous example. Where the fault appears to be pinched out low amplitudes are present. When compared to the input, these low amplitudes occur where the fault is pinching and the anticline is terminating against the fault. There are also some areas of high amplitude discontinuities where the anticline is present, which are a result of stratigraphic changes that the algorithm calculated.

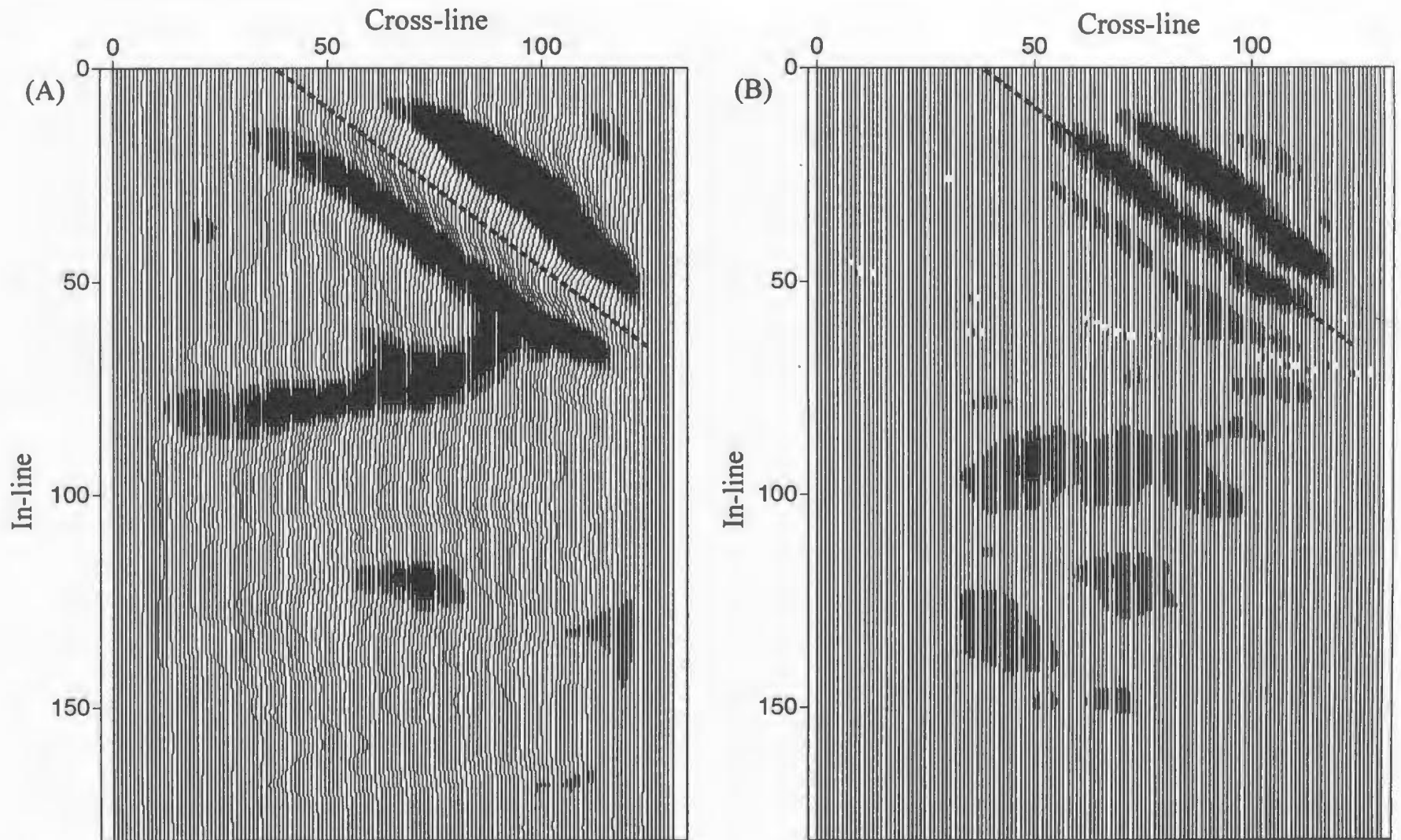


Figure 4.10: Coherency result at depth position 215 (B) as compared to model input (A). Dashed line represents fault interpretation.

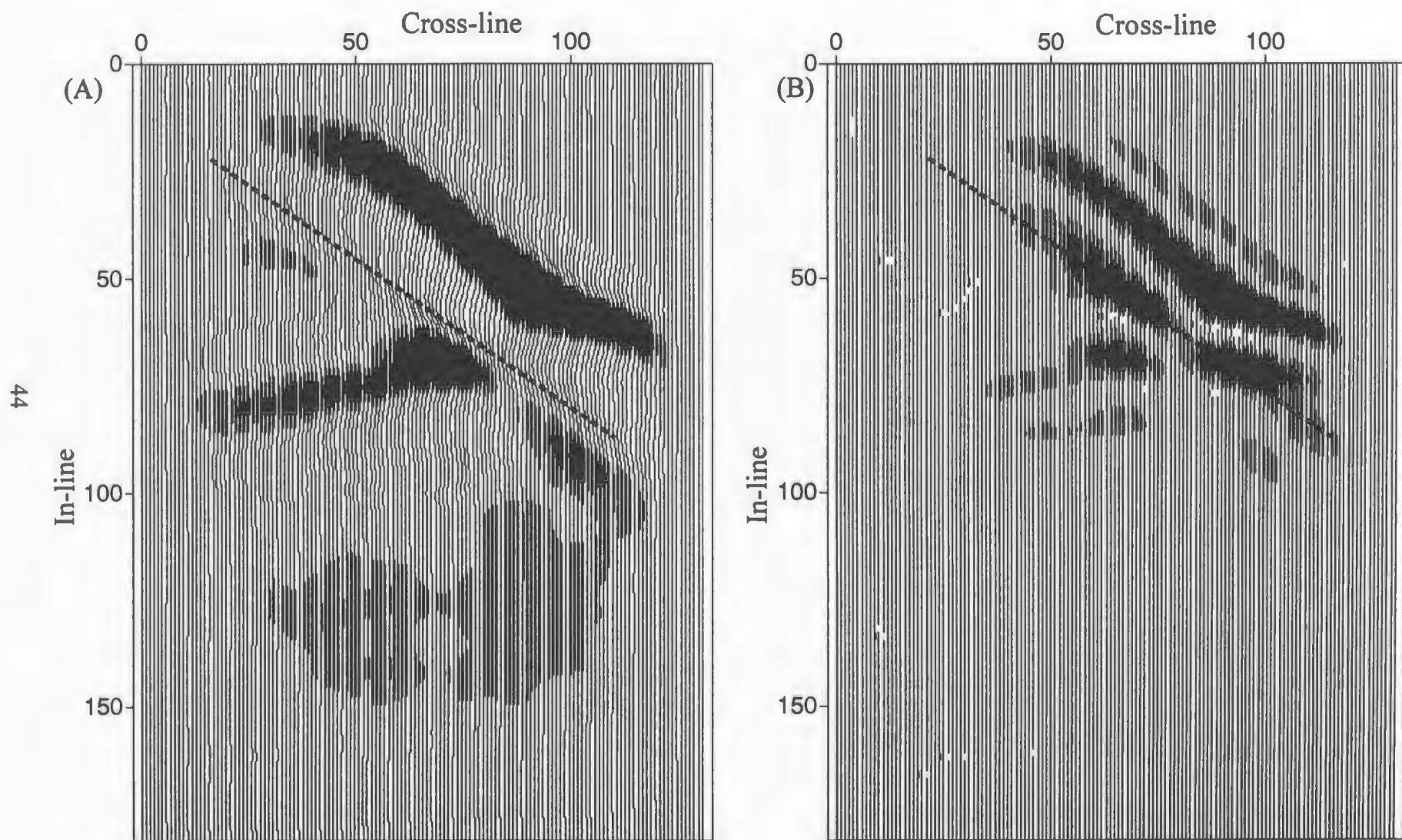


Figure 4.11: Coherency result at depth position 250 (B) as compared to model input (A). Dashed line represents fault interpretation.

Next, depth section 175 that contains a smaller, less evident fault was tested using the coherency algorithm. If we look at depth slice 170 (figure 4.6) we see a smaller fault at $x = 125$. Therefore if we take depth slice 170 and use it as input for the coherency algorithm, it is expected that the fault would be observed at $x = 125$ and $y = 50$. The result shown in figure 4.12 does seem to do a very good job at imaging the fault in its correct position. Also from this result it is evident that where there were areas of high amplitude continuous reflection seen on the input there are also some high amplitude areas of discontinuous reflections image. These areas of discontinuous reflection which are either due to stratigraphic changes or trace to trace effects of the algorithm.

The results of the coherency tests can be summarized as follows. Firstly, it images the Murre fault in its correct position and also images other areas of discontinuous reflection as shown in figure 4.12. When imaging the Murre fault, it also seemed to image both the fault as well as a mirror image of the fault above it. This is caused by wavelet size, residual energy or trace to trace changes between the top of the fault and the unit above it.

4.3.2 Differencing Result

The model data described in section 4.1 was used as input into the differencing algorithm. This algorithm takes the seismic traces and computes the difference, finally outputting the average differences between seismic traces. Therefore large differences between seismic traces, such as those caused by faults, will result in high values indicative of a discontinuity. The results from the differencing algorithm using the model data are illustrated in the following figures. Figure 4.14 (b) illustrates the result of depth

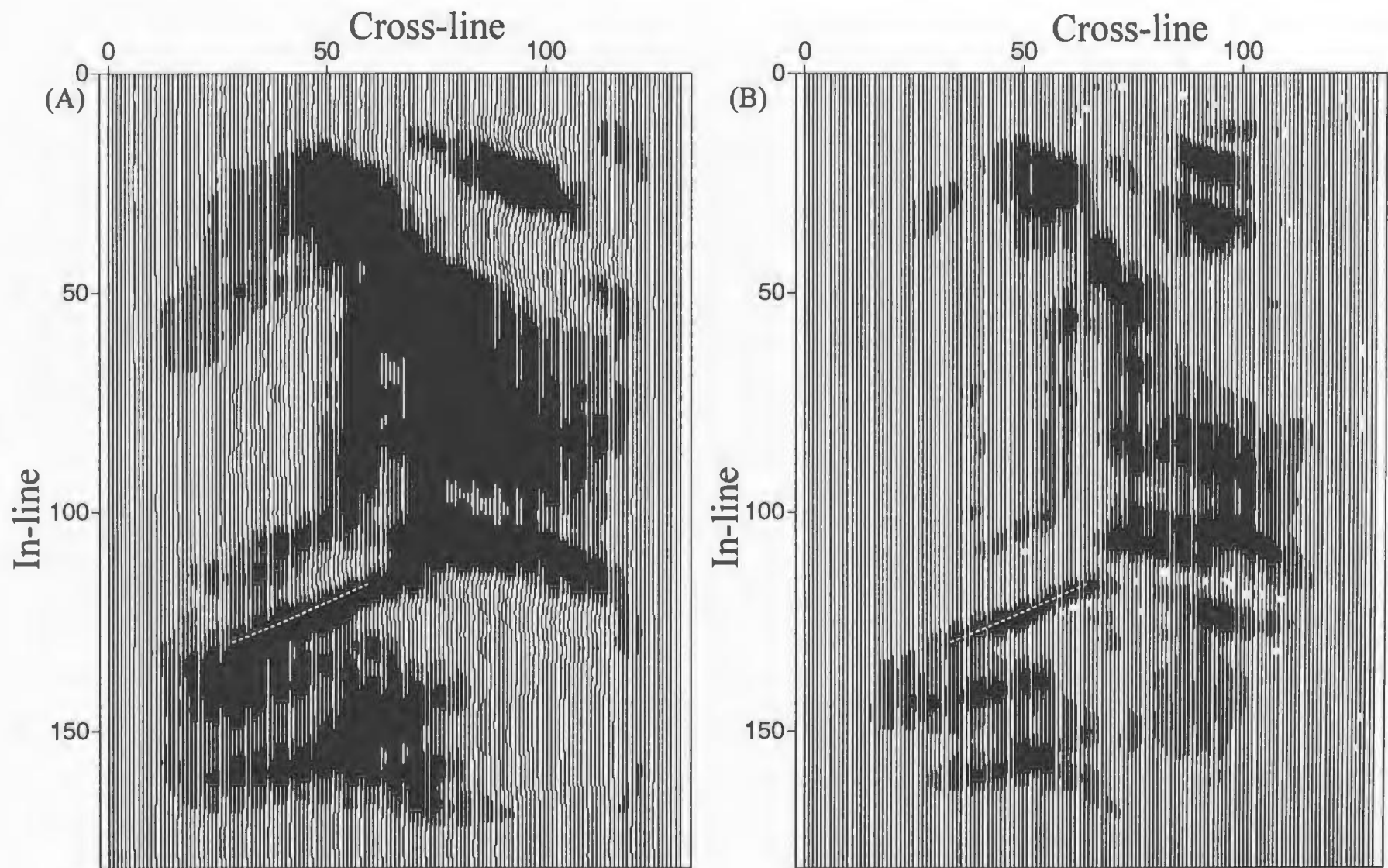


Figure 4.12: Coherency result at depth position 170 (B) as compared to model input (A).

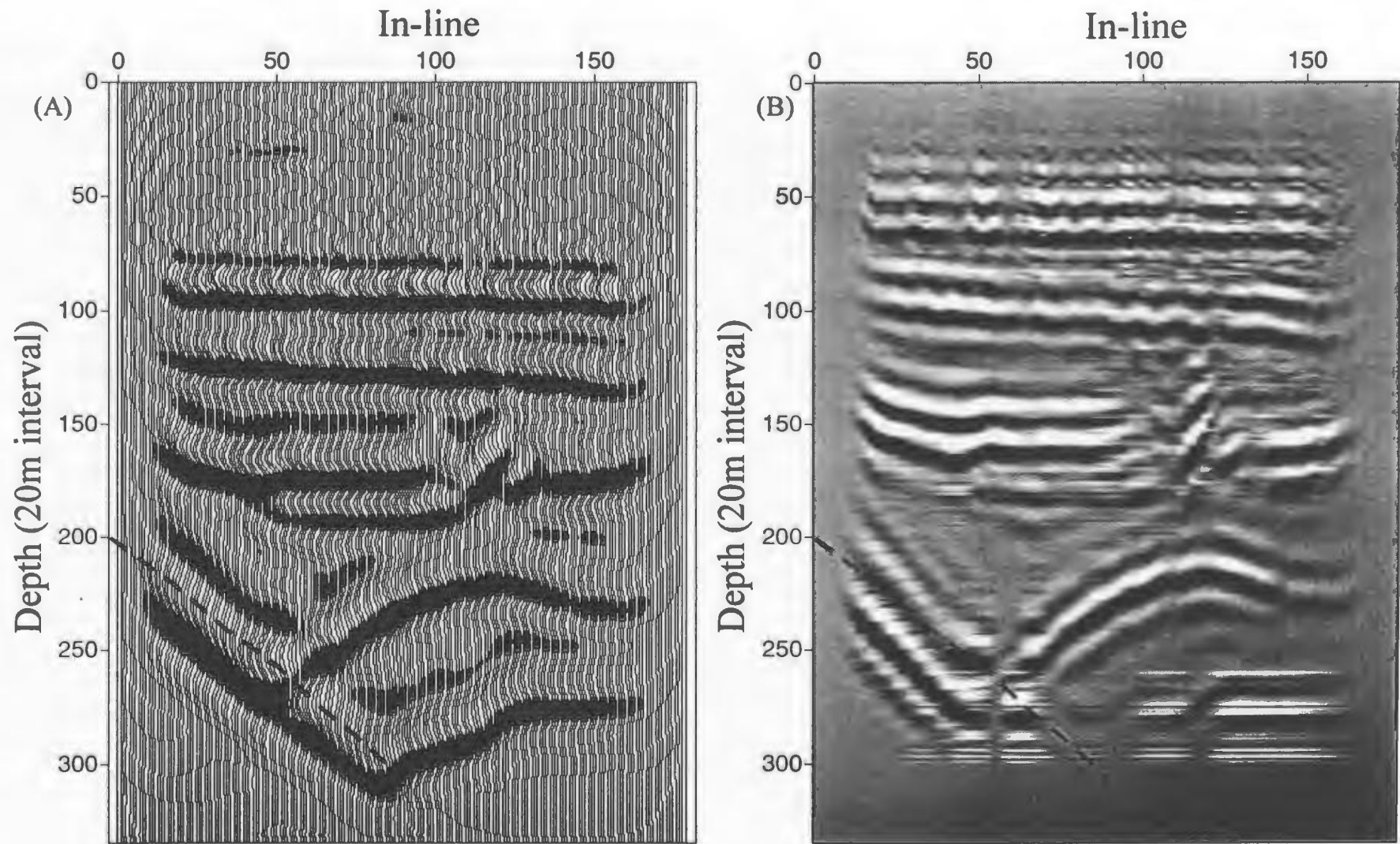


Figure 4.13: Coherency result at vertical line 60 (B) as compared to model input (A). Dashed line represents fault location.

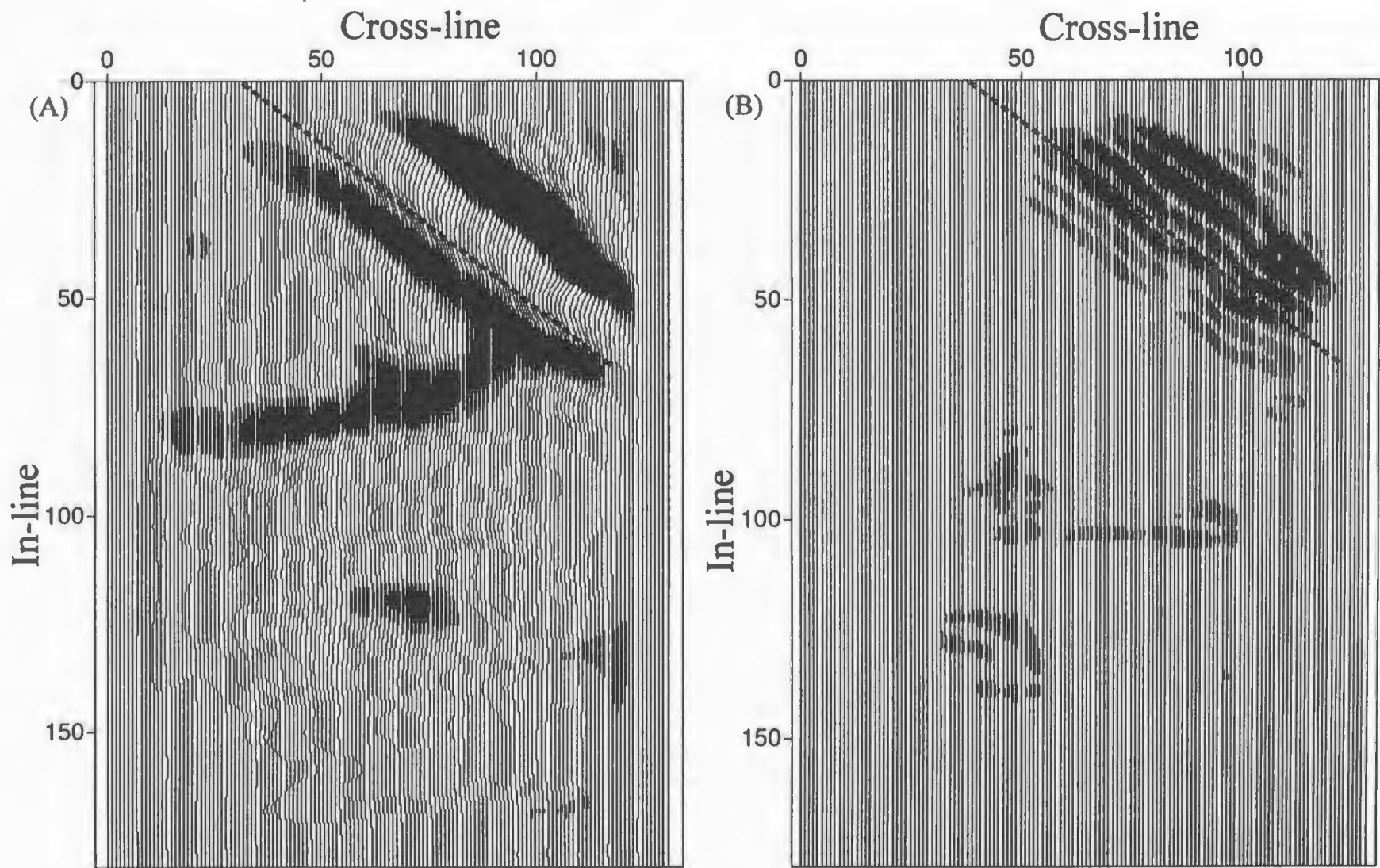


Figure 4.14: Differencing result at depth position 215 (B) as compared to model input (A). Dashed line represents fault location.

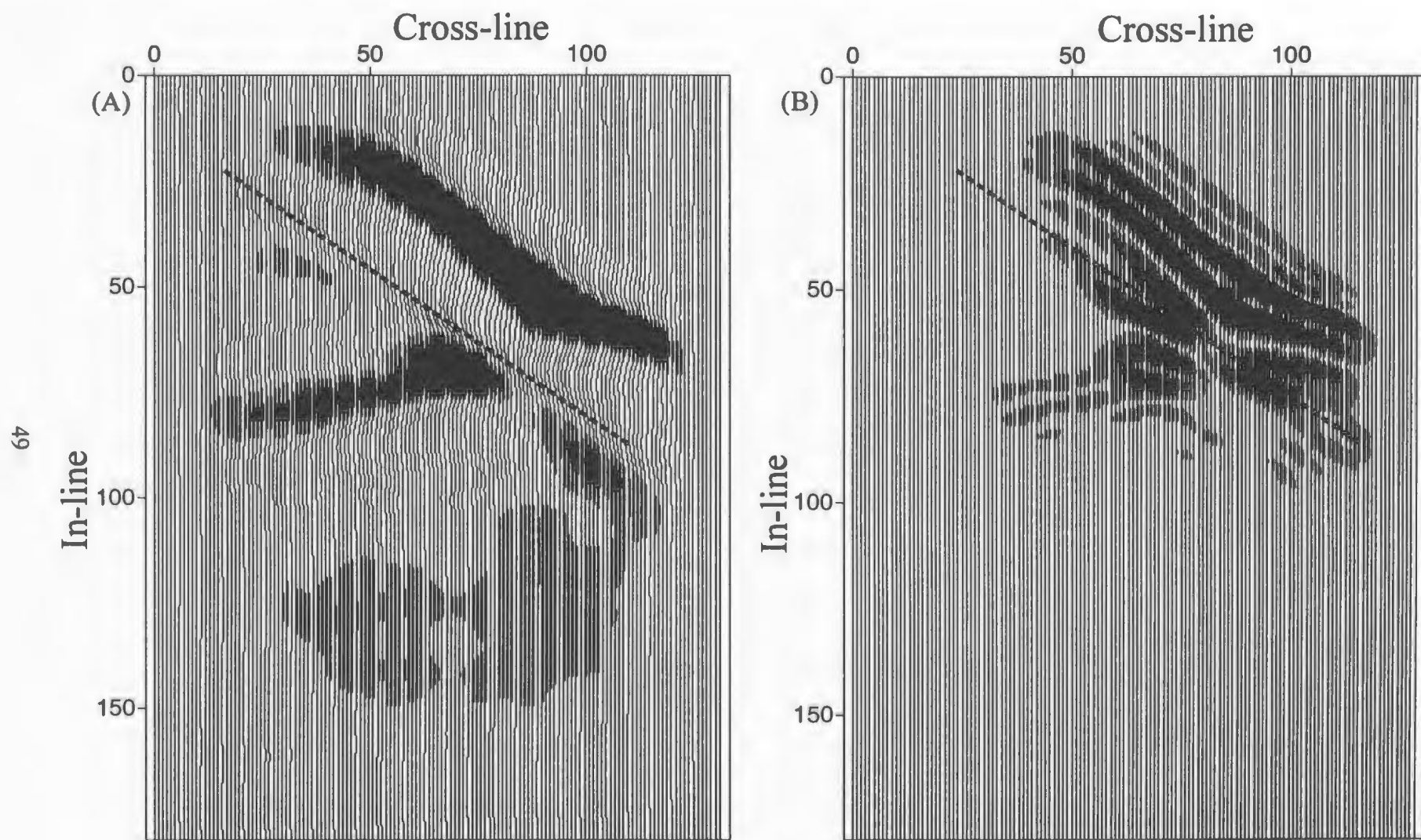


Figure 4.15: Differencing result at depth position 250 (B) as compared to model input (A). Dashed line represents fault location.

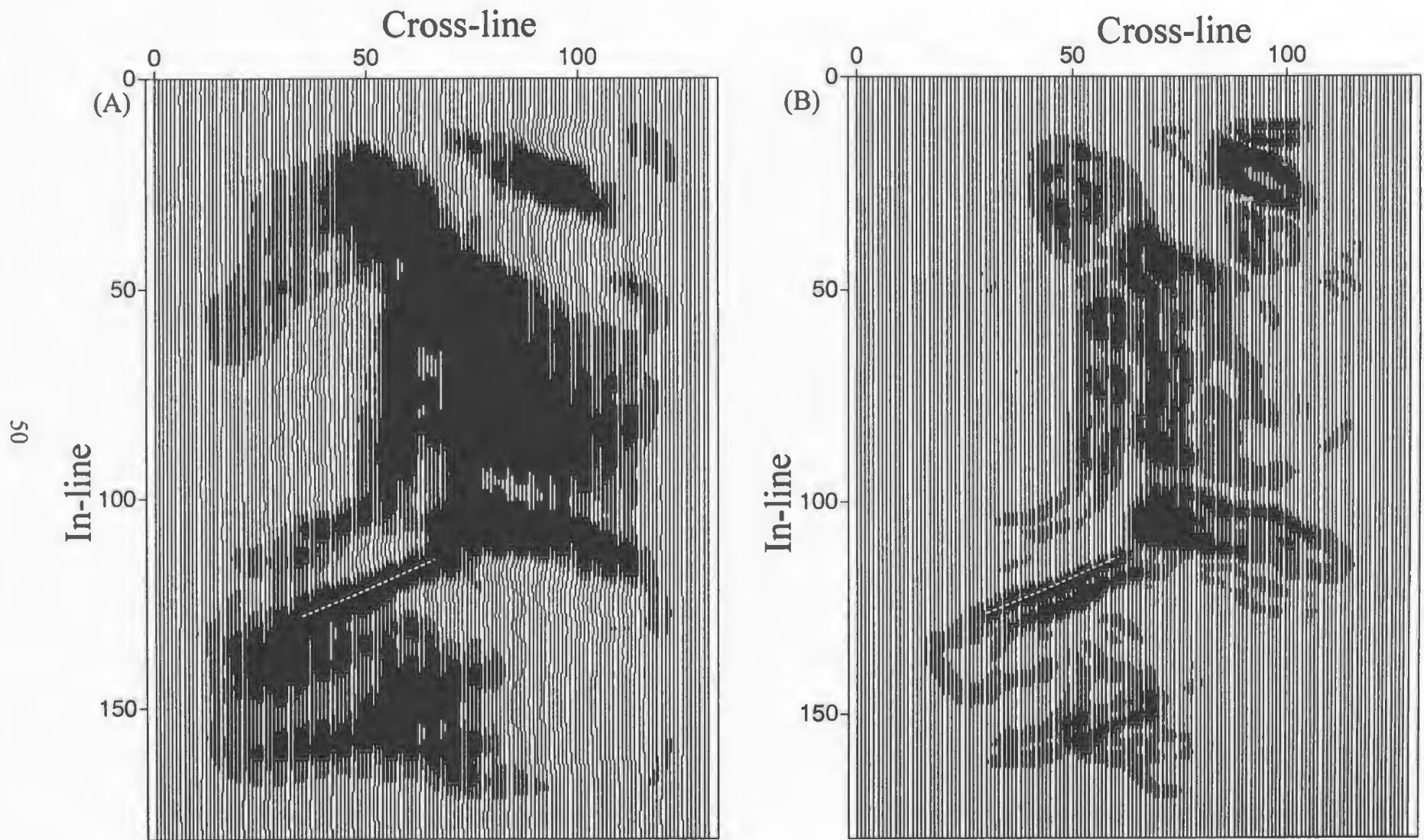


Figure 4.16: Differencing result at depth position 170 (B) as compared to model input (A). Dashed line represents fault location.

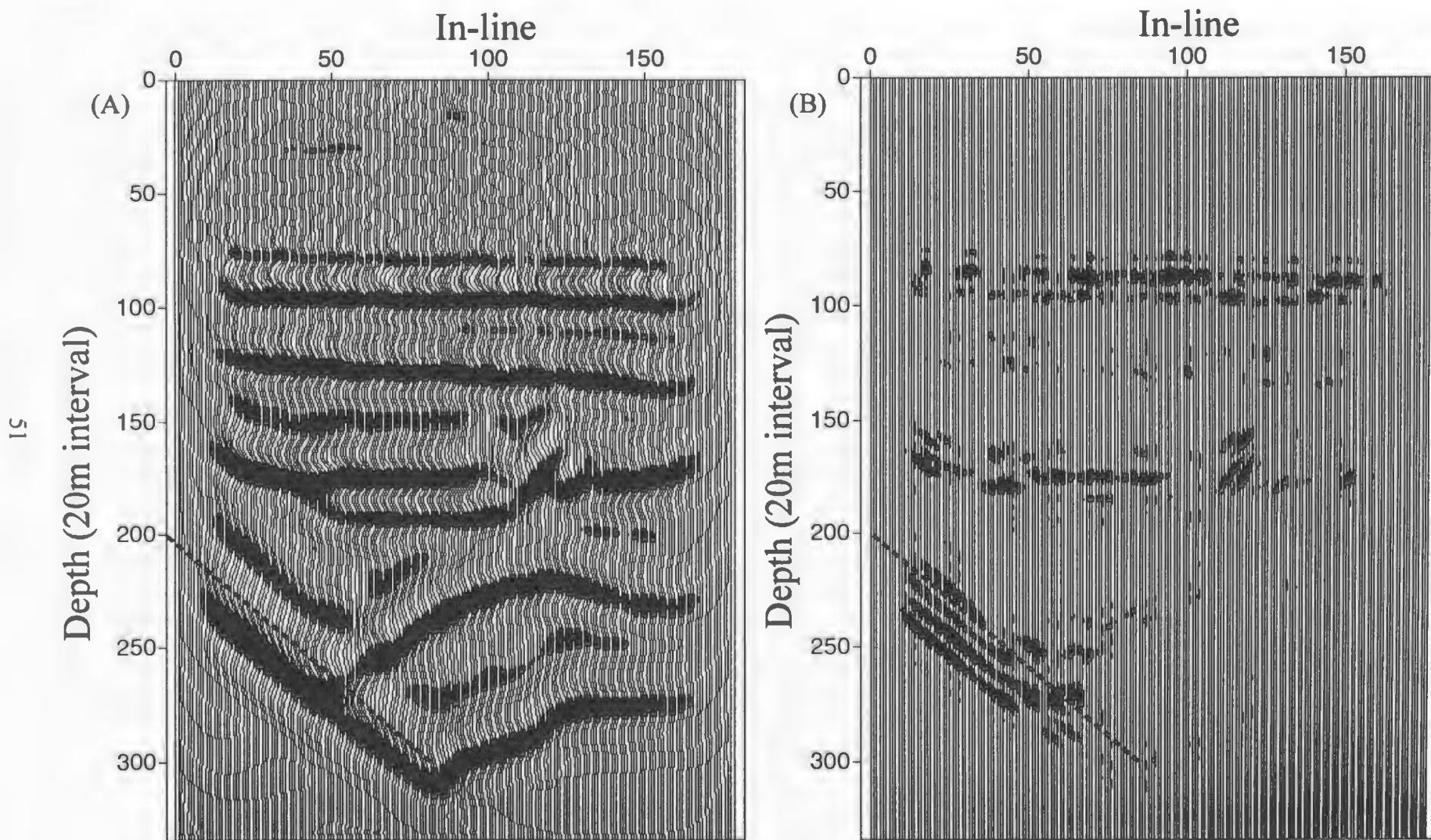


Figure 4.17: Differencing result at vertical line 60 (B) as compared to model input (A). Dashed line represents fault location.

plane 215 as compared to the input shown in figure 4.14 (a). This result shows that the algorithm computes an adequate image of the fault, but does not give it a clear position. There appears to be high frequency oscillations in the image primarily because it is the result of a derivative.

Figure 4.15 illustrates the differencing result of the depth position slice 250. This result is similar to the 215th depth slice in that there are high frequency oscillations, and therefore the correct position of the fault cannot be determined. The differencing result of the depth position 170 is shown in figure 4.16. The result illustrates that the algorithm does eliminate most of the continuous reflections, and highlights discontinuous reflections such as the fault at $x=125$ and $y=50$. There are some high frequency oscillations present but not as much as the previous depth sections at 215 and 250.

Figure 4.17 illustrates the result of using a vertical section at position line 60 as input into the differencing algorithm. This result does a very good job in imaging the discontinuous features such as those of the Murre fault and the stratigraphic change at depth slab 170. Again, high frequency oscillations are present at the Murre fault but seem to only oscillate within the fault plane.

The differencing result illustrates that the algorithm highlights discontinuous reflections and eliminates continuous reflections with some degree of accuracy, but tends to have high frequency oscillations. The vertical section produced the best result, due to the vertical resolution of the data not being dependent on the vertical time window size therefore producing sharp inline and crossline difference results (Luo et al., 1996). The oscillations as seen from the depth sections make it very difficult to determine the correct position of the Murre fault and other stratigraphic changes within the model. A reason

for the oscillations in frequency may be caused by the fact that differencing is similar to the derivative method that tends to produce high frequency oscillations.

4.3.2 Second Derivative Result

The second derivative method is very similar to the differencing method except that the second derivative does not take the absolute values of the differences as shown in equations 2.7 and 2.8. Second derivative maps are mainly used to locate local anomalies in potential field data (Garland, 1965). There are other uses of second derivative maps using seismic data. Such maps produce dip changes of the seismic data. Therefore because faults are involved, a change in dip will occur on a second derivative map.

The results using the second derivative algorithm are shown in figures 4.18, 4.19, 4.20 and 4.21. Figure 4.18 illustrates the result at depth position 215 as compared to the input. This result produces a very good image of the fault and can be correctly imaged. There does seem to be some extra reflections below the fault, which are due to dip changes in the subsurface. Figure 4.19 is the result at depth position 250. Again the fault is correctly imaged but seems to be broken in places. This is due to the fault pinching out on the input. The third depth slab used was at depth position 170 and is shown in figure 4.20. This result seems to image much more than just the fault, and again this can be taken as a result of dip changes at this depth. The result of the vertical section is shown in figure 4.21. This result looks different than that of the other examples, but this is due to the figure being plotted using a different plotting program as opposed to actual differences in the result. This imaged the fault well, although it appears to be broken near

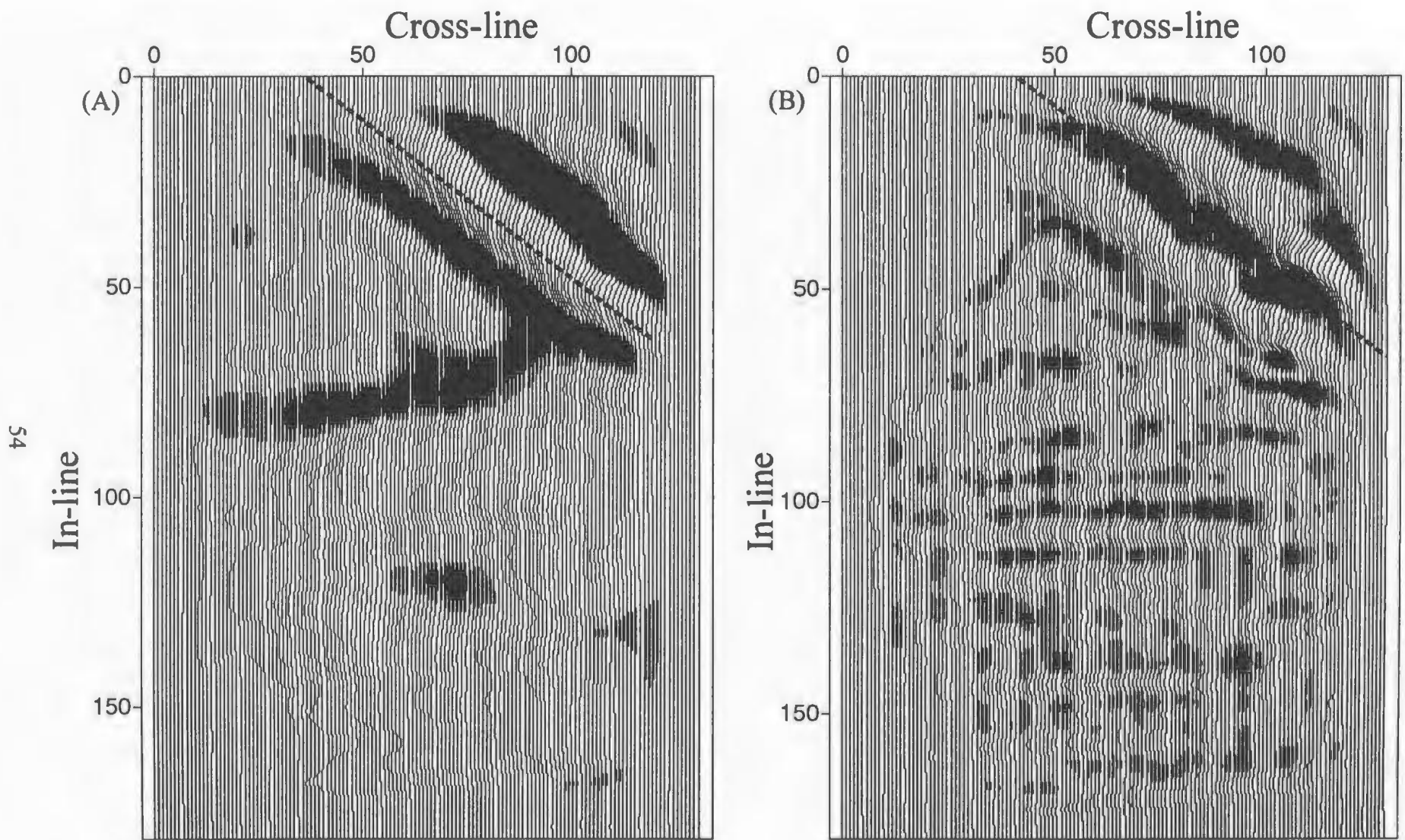


Figure 4.18: Second derivative result at depth position 215 (B) as compared to model input (A). Dashed line represents fault location.

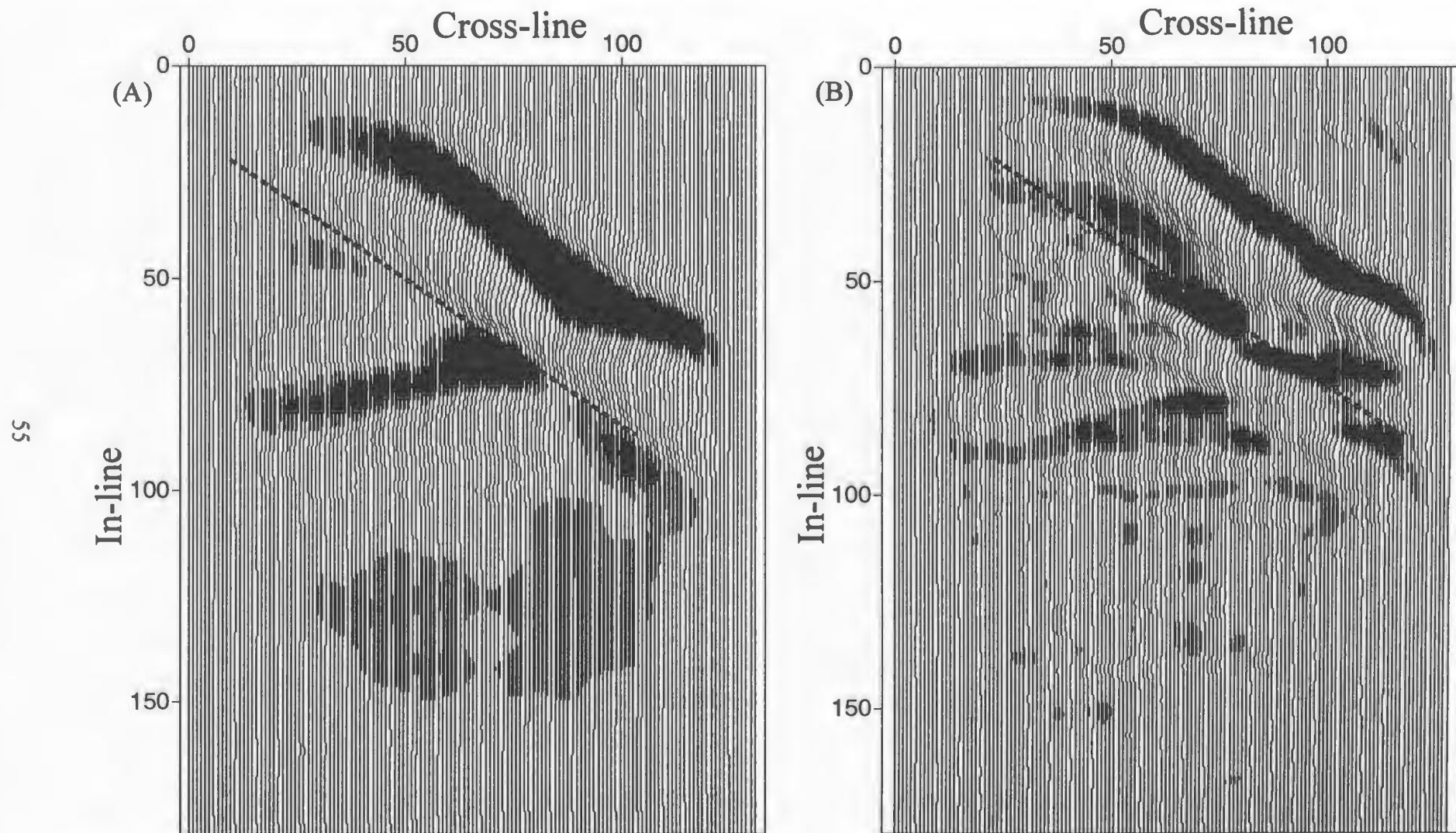


Figure 4.19: Second derivative result at depth position 250 (B) as compared to model input (A). Dashed line represents fault location.

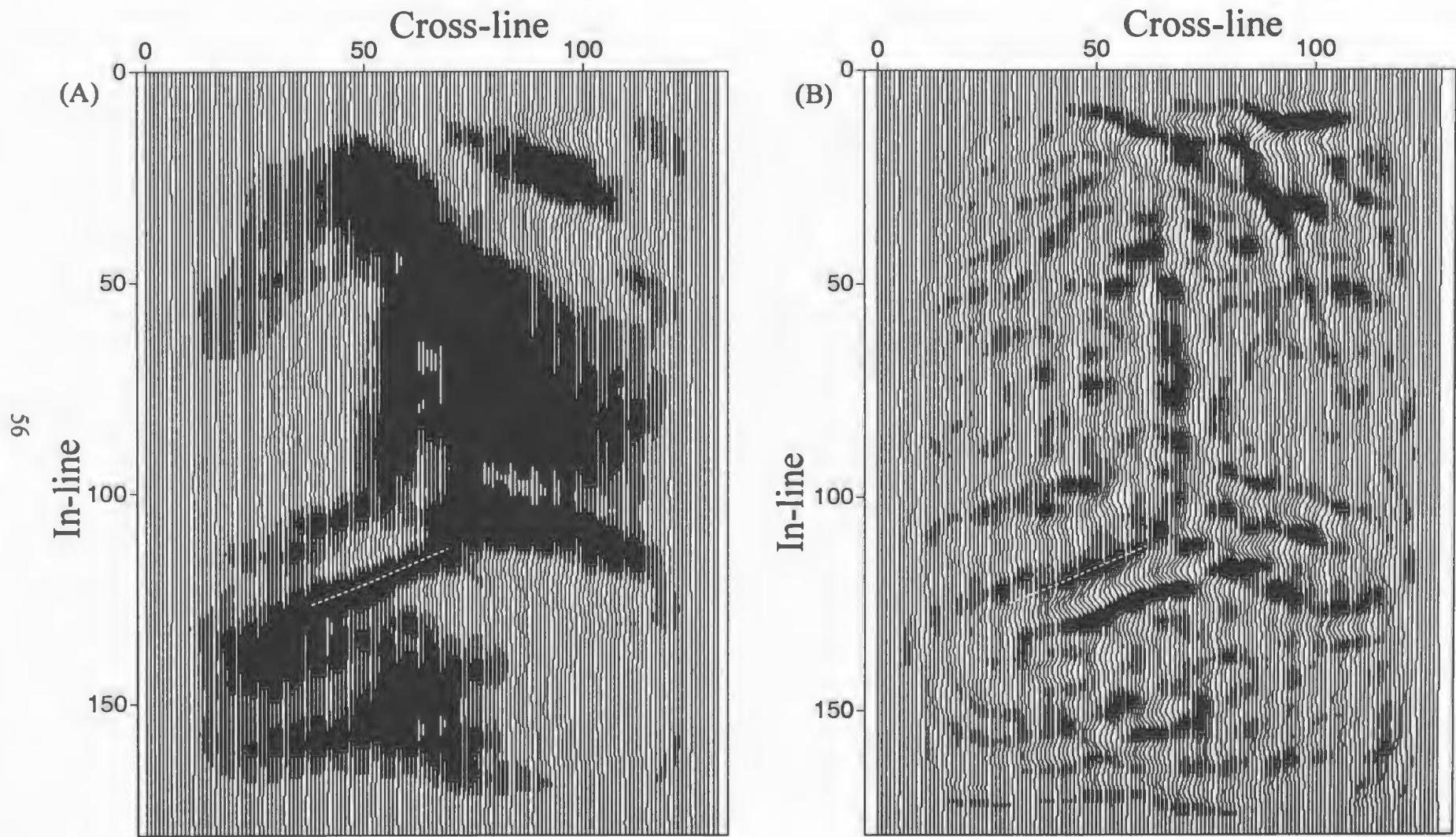


Figure 4.20: Second derivative result at depth position 170 (B) as compared to model input (A). Dashed line represents fault location.

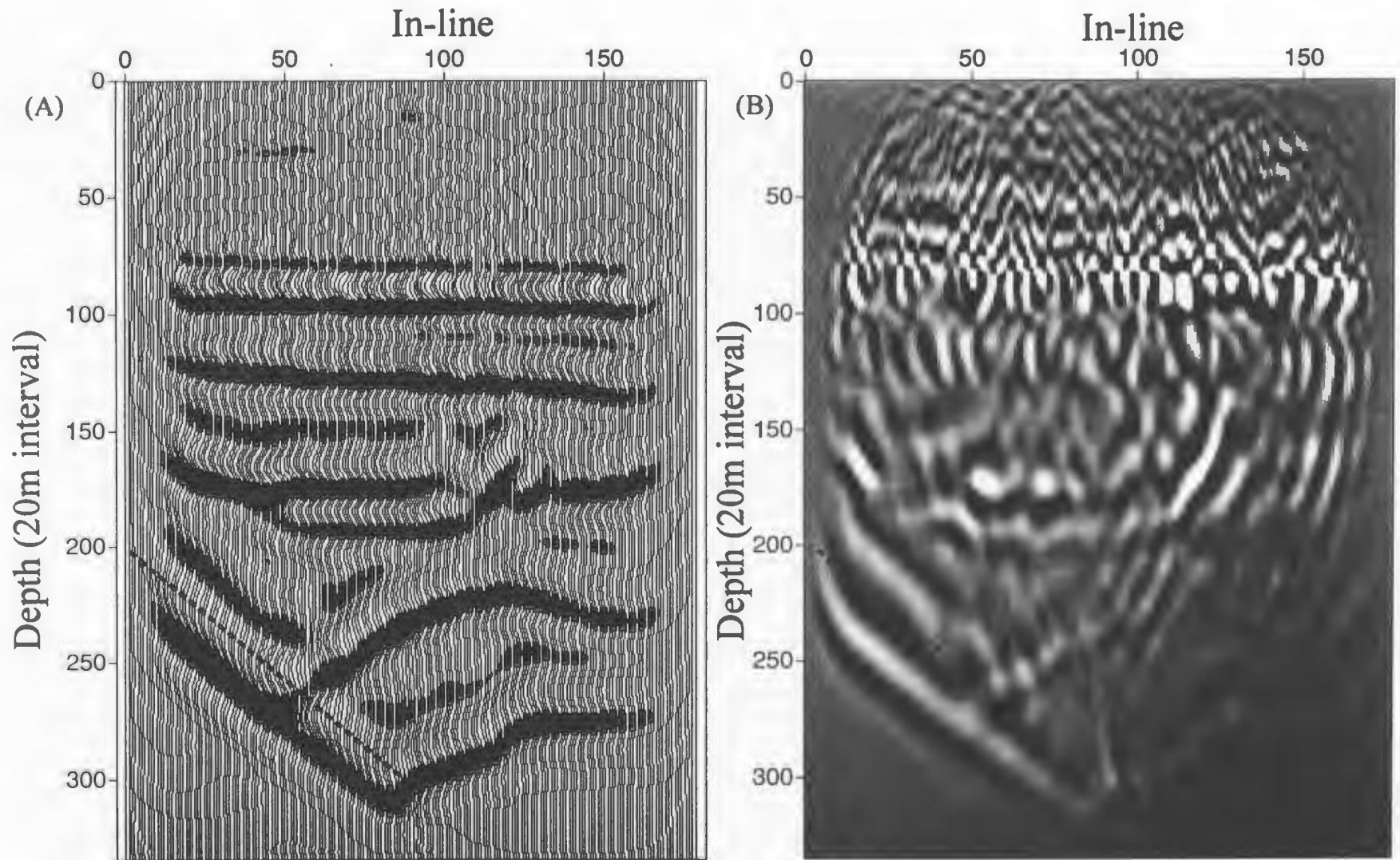


Figure 4.21: Second derivative result at vertical line 60 (B) as compared to model input (A). Dashed line represents fault location.

the position of the rollover anticline. There does appear to be many of reflections imaged and there seems to be a problem at the top of the line. Which is due to amplifying higher frequency noise in x and y.

The result of using the second derivative algorithm produces results which images the fault in it correct position and is easy to interpret.

4.4 Comparison of Results

The results between the three algorithms will be discussed in this section. The result of using depth section 215, 250 and 170 as shown in figures 4.22, 4.23, and 4.24 (a) is the input data, (b) is the coherency result, (c) is the differencing result, and (d) is the second derivative result. By examining the result of figures 4.22, 4.23, and 4.24. It can be clearly shown that the second derivative produced the best result for the fault in depth sections 215 and 250. The coherency result was also quite good except you can not be sure if the upper or lower discontinuity is the fault. In the differencing result the fault position is almost impossible to locate, you could assume that it is in the middle of the high frequency oscillations but that would prove to be incorrect. Whereas for depth slab 170 as shown in figure 4.24 the coherency result seems to produce the best result of the input feature. The differencing and second derivative results do a good job at imaging the Murre fault.

Figure 4.25 compares the coherency (b), differencing (c) and second derivative (d) result for line 60 of the model data (a). Here we compare the result and see that the second derivative result gives the best image of the fault plane. Again the differencing result has high frequency oscillations.

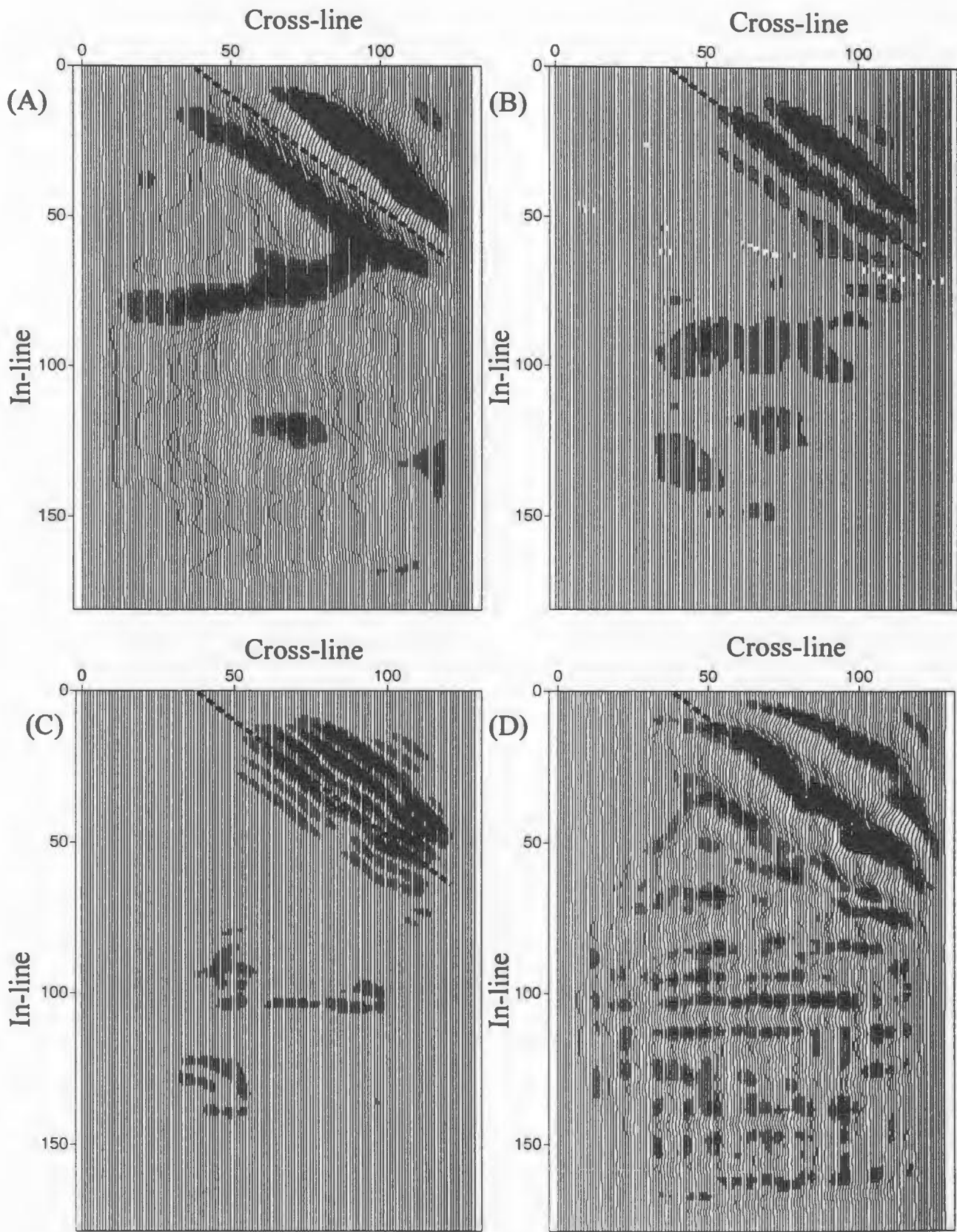


Figure 4.22: Comparison between coherency (B), differencing (C), and second derivative (D) result using input model (A) at depth slice 215.

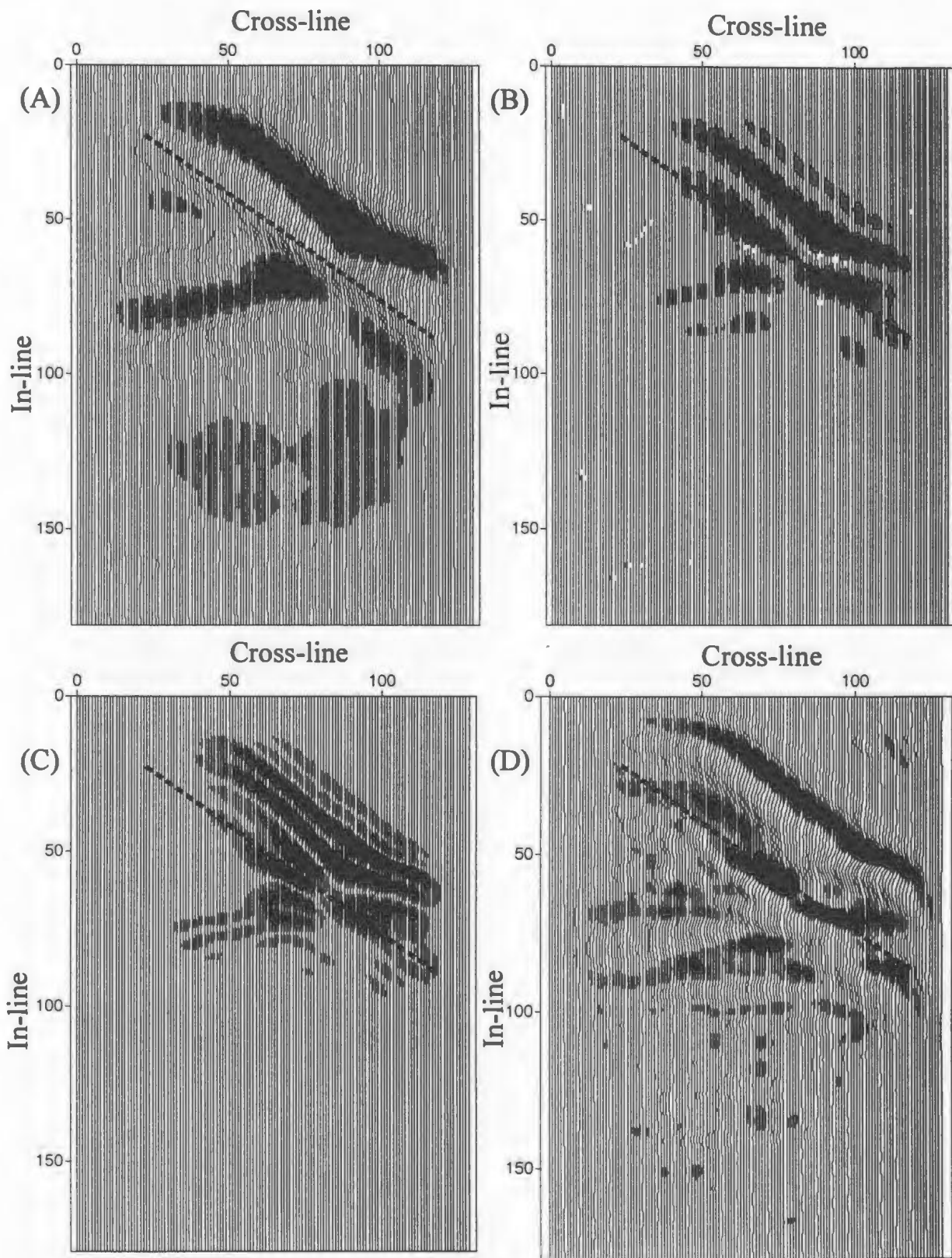


Figure 4.23: Comparison between coherency (B), differencing (C), and second derivative (D) result using input model (A) at depth slice 250.

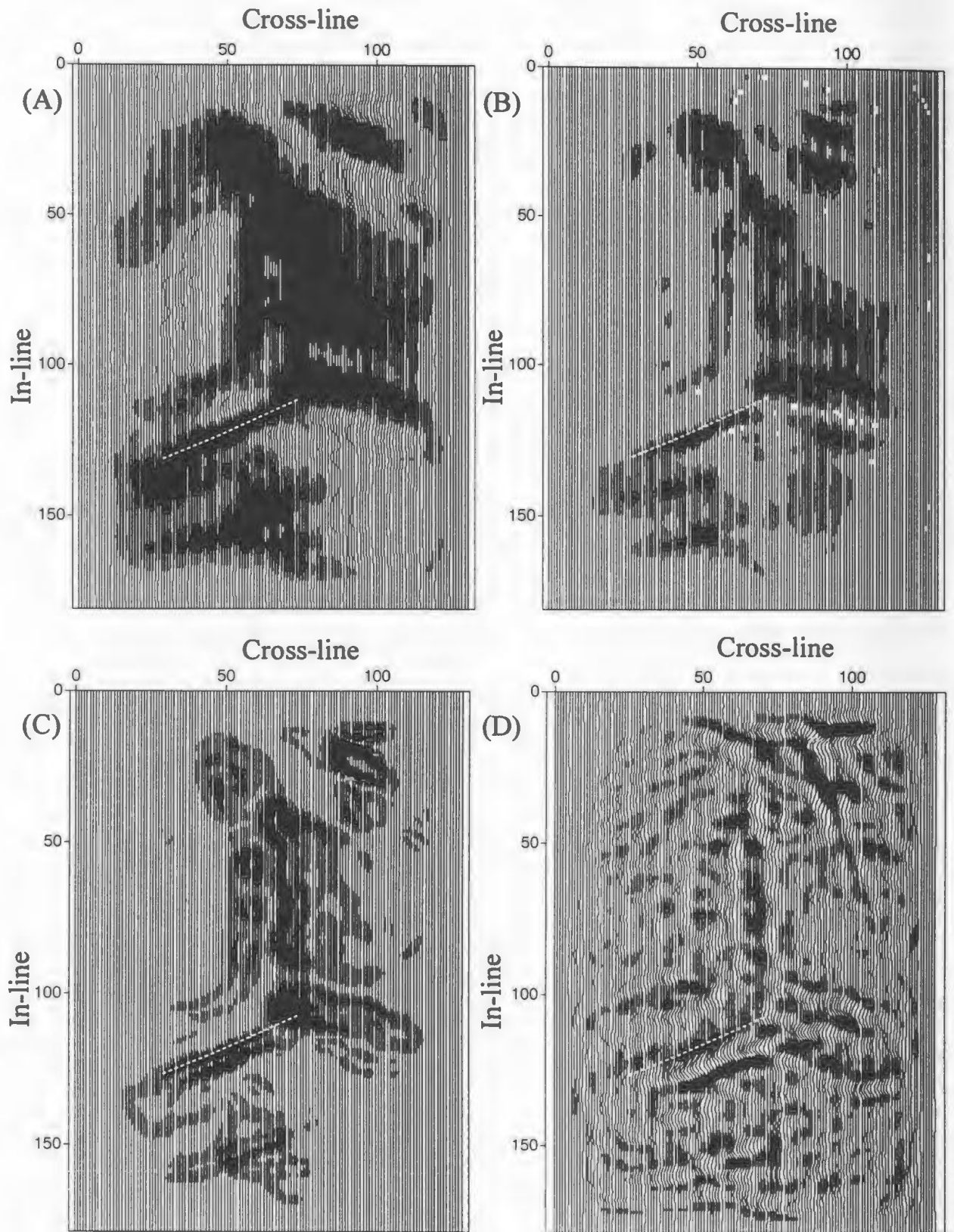


Figure 4.24: Comparison between coherency (B), differencing (C), and second derivative (D) result using input model (A) at depth slice 170.

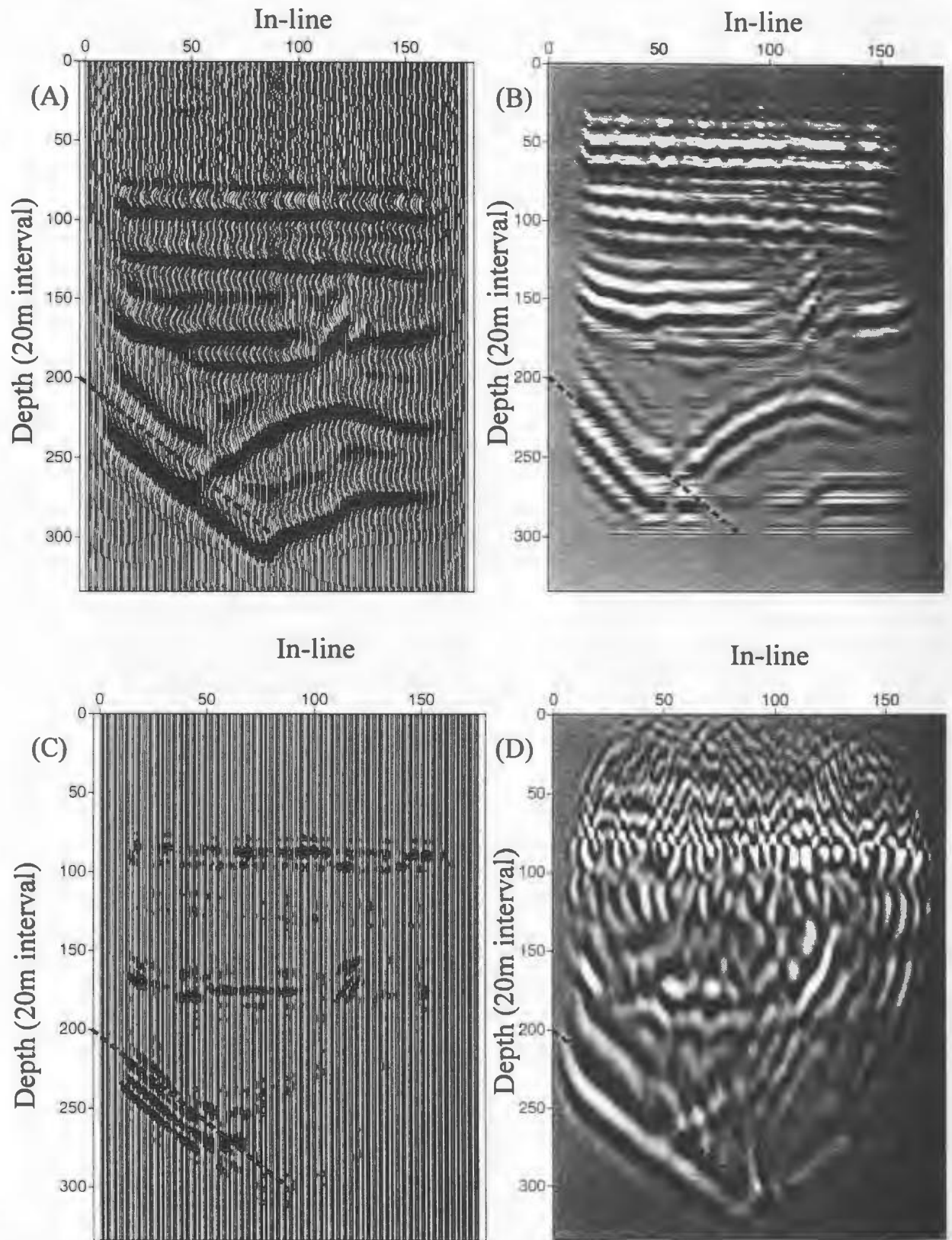


Figure 4.25: Comparison between coherency (B), differencing (C), and second derivative (D) result using input model (A) at vertical slice 60.

The second derivative algorithm tends to give better results than the differencing and coherency results for fault imaging whereas the coherency result tends to be better at imaging shallower stratigraphic features. The differencing results tend to have high frequency oscillations that make it difficult to interpret the fault position. One possible way to get rid of these high frequency oscillations is to use deconvolution.

Deconvolution would also remove wavelet delay effects. An example of how this type of processing can effect the fault positioning is shown in Figure 4.26. The seismic event is moved up to the correct position and the oscillating event is compressed into one dominant peak. This obviates the problem of ambiguity in defining the fault. This deconvolution is implemented by designing a Wiener filter to shape the seismic wavelet to a spike as shown by Robinson and Treitel (1980). Of course this deconvolution requires knowledge of the wavelet, which in the case of real data, is a nontrivial issue.

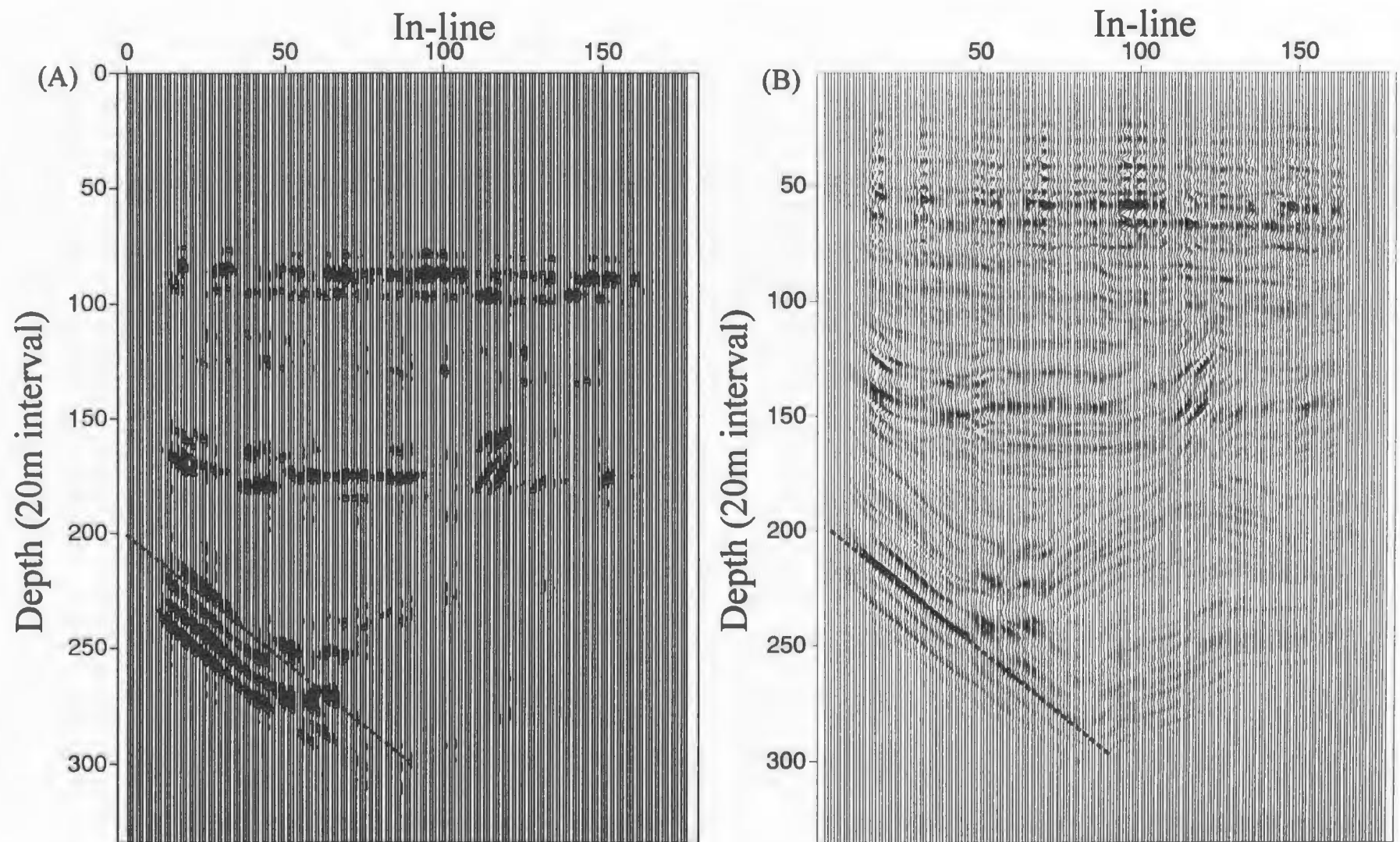


Figure 4.26: Comparison between differencing (A), and deconvolution result (B).

Chapter 5

Hibernia Real Data Examples

5.1 Application to 3D depth migrated data

This section describes results of the fault detection algorithms using data obtained during the Hibernia 1991 three-dimensional survey. The area used for the reverse time migration shown in figure 5.1 (outlined in red), and was chosen because it overlaps with the model area and illustrates positioning of the Murre fault. A portion of this data was used for fault detection and consisted of 150 in-lines and 121 cross-lines with 350 depth traces. Figure 5.2 illustrates a vertical section through the 3D cube at in-line 60. In-line 60 was depth migrated using the same poststack depth migration that was used for the model data. From Figure 5.2, it is apparent that the Murre fault has vertical positioning from 250 to 350, as illustrated by the dashed line. For the above, and each of the examples to follow, a dashed line will outline the Murre fault.

To test the fault detection algorithms, depth slice 275 (figure 5.3) was chosen to represent the upper portion of the fault and 325 (figure 5.4) to represent the lower portion of the fault. Figure 5.3 illustrates a plane through the real data at depth section 275; the Murre fault is interpreted at $x = 10-90$ and $y=130-140$. As mentioned above, a dashed line represents the fault interpretation. Figure 5.4 illustrates a depth slice through the real data at depth position 325. This shows that the fault is positioned at $x = 10-100$ and $y = 100-120$. The results of fault detection testing performed on in-line 60 (depth slices 275 and 325) are provided in the following sections.

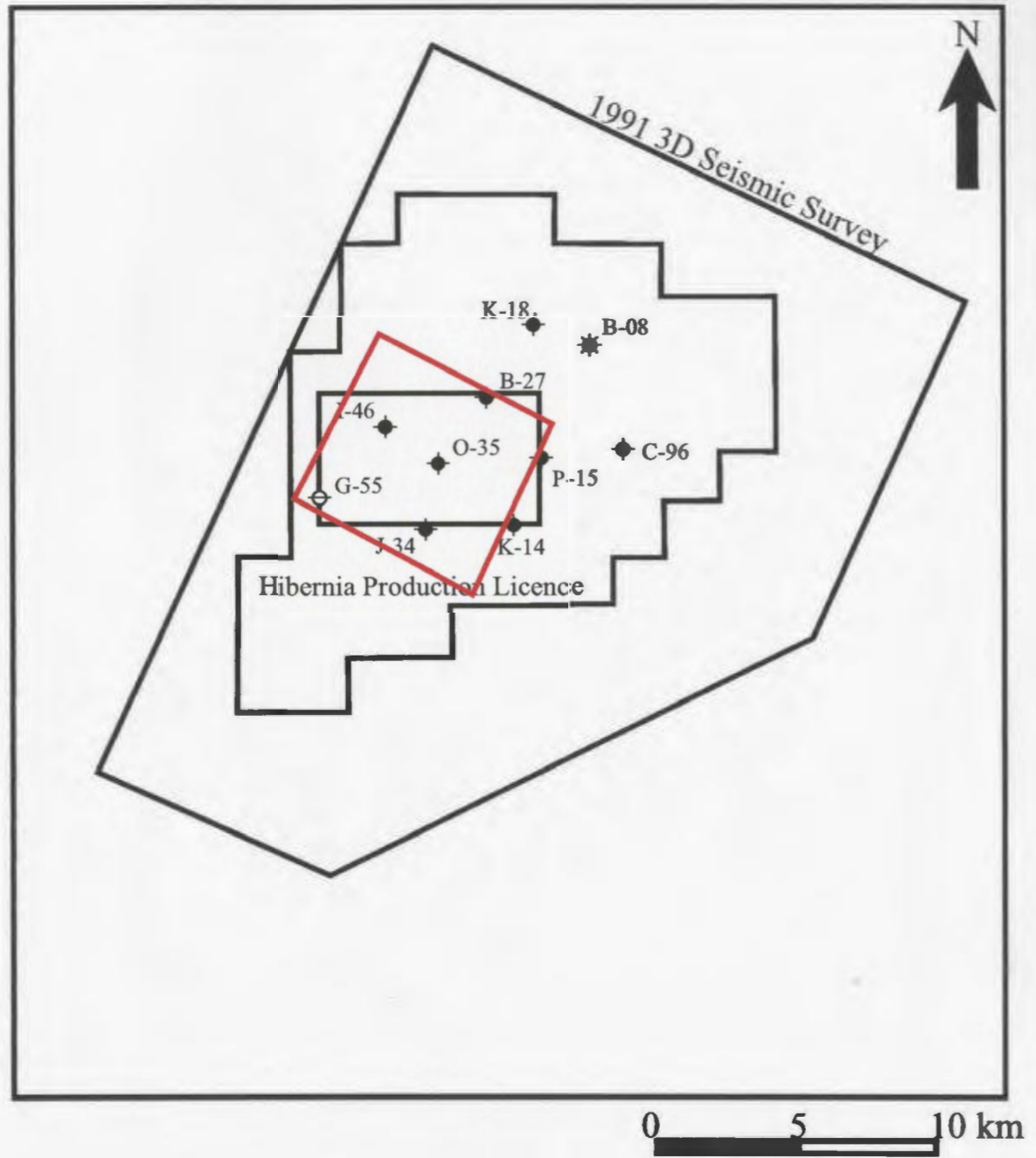


Figure 5.1: Illustration of the 1991 3-D seismic survey shot over the Hibernia field. Also shown is the well locations and an outline of the seismic area used for the model data (black rectangle) and real data (red). Adapted from Kelly (1998).

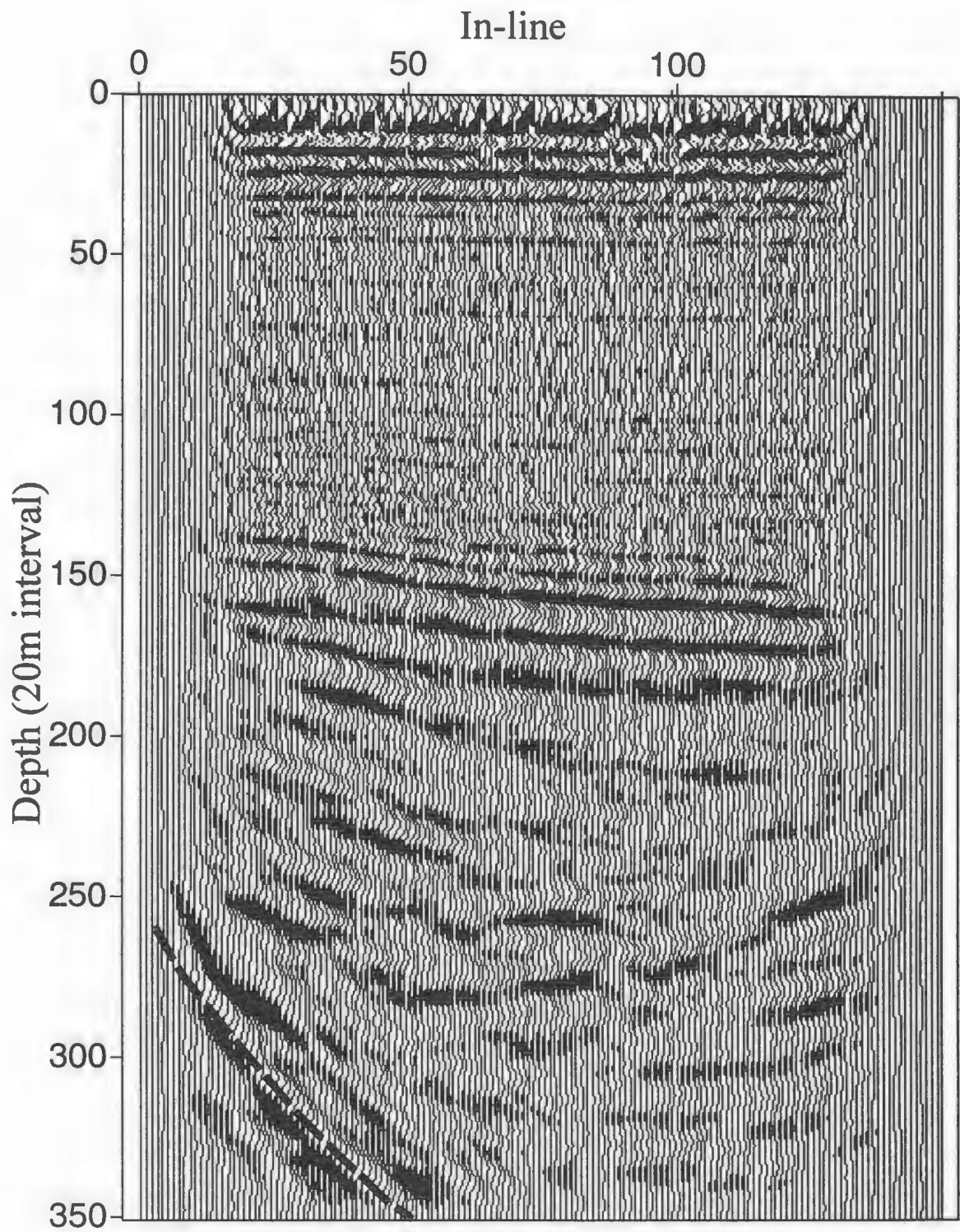


Figure 5.2: Line 60 from the depth migrated 1991 Hibernia survey.

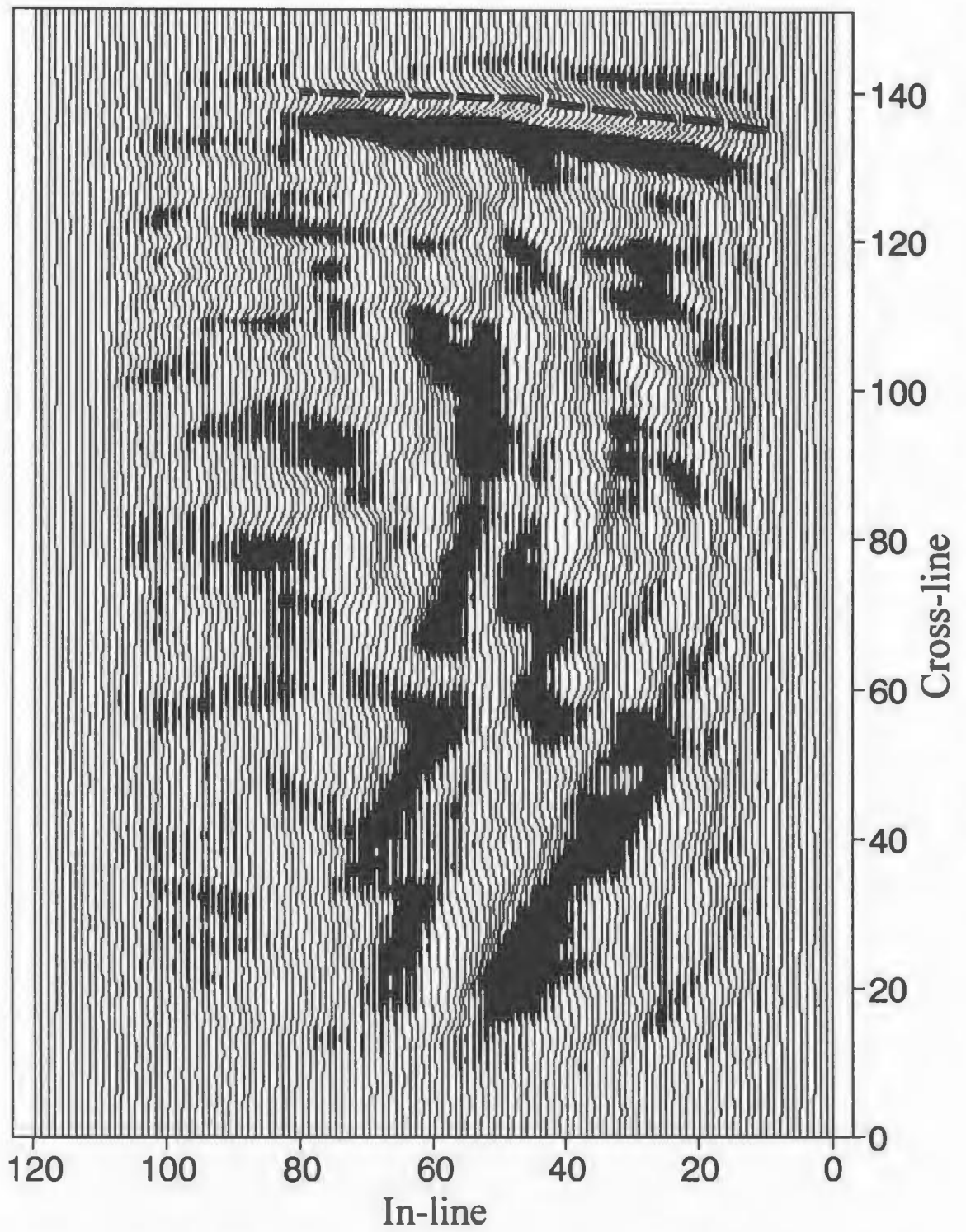


Figure 5.3: Plane through real data at 275. Dashed lines represents fault interpretation.

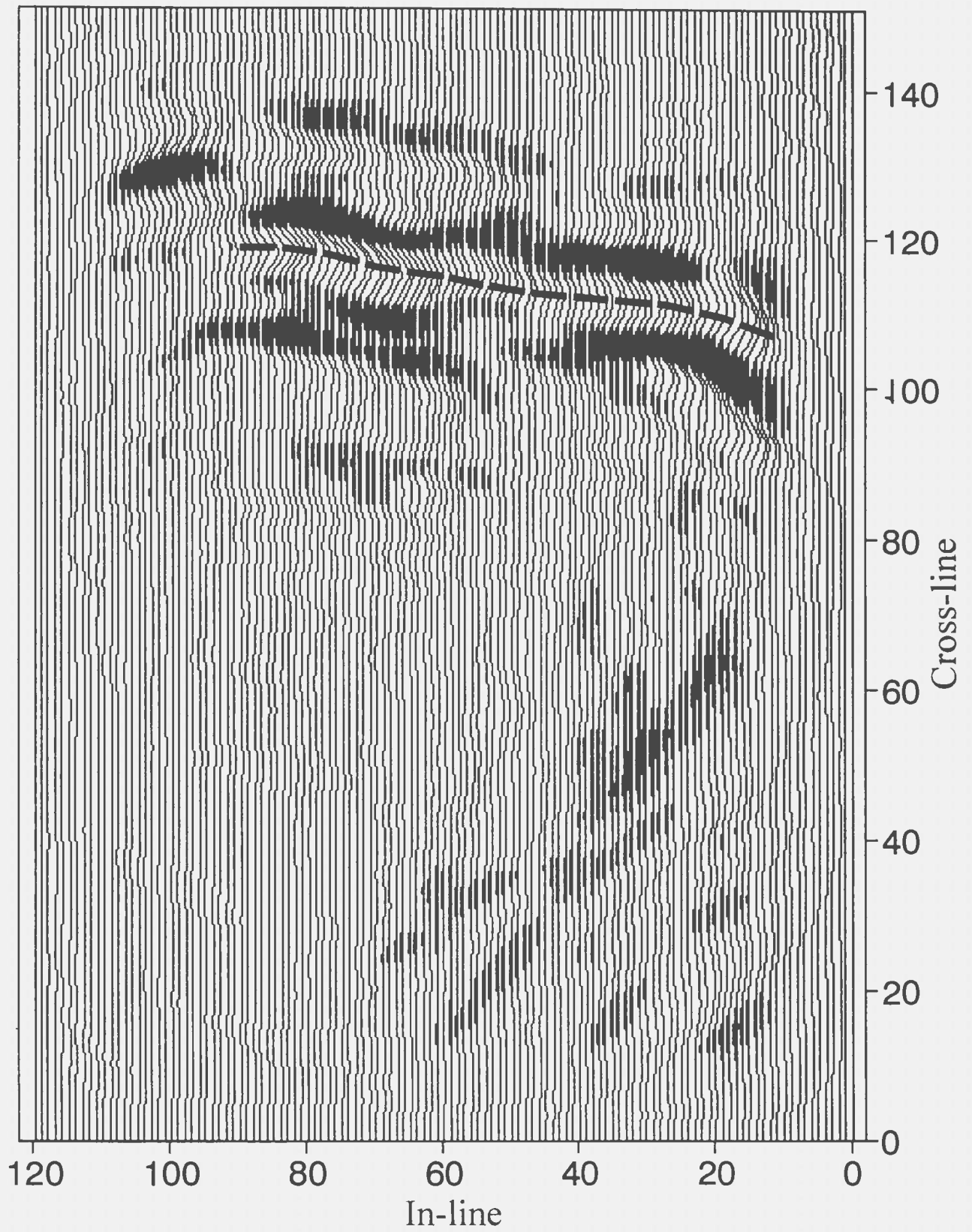


Figure 5.4: Plane through real data at 325. Dashed lines represents fault interpretation.

5.2 Comparison of Depth Migrated Results

This section describes comparison results of the different fault detection algorithms for each of the real data input. Depth section 275 will first be compared, followed by depth section 325, then vertical section in-line 60. These results are shown in figures 5.5, 5.6, and 5.7 respectively.

Result of depth section 275 is illustrated in figure 5.5. The input shown in (A), illustrates the Murre positioned at the top of the section. These results illustrate that the coherency (B) and differencing (C) give similar results with coherency giving greater amplitudes and appearing more continuous. Both perform well at imaging the Murre fault and in eliminating the continuous reflections. Alternatively the second derivative (D) result does image the Murre fault in its correct location, as well gives the correct wavelet size of the fault.

Depth section 325 input (A) and results (B, C, and D) are illustrated in figure 5.6. At first observation it appears as though neither result imaged the Murre fault adequately but upon closer inspection the second derivative (D) does image the extent of the Murre fault better than the other methods. Again, the coherency (B) and differencing (C) do eliminate almost all the reflections except those of the Murre fault, however they do have the same problem of wavelet size (as when imaging depth section 275). The input of depth section 325 illustrates that the Murre fault has an irregular shape; it tends to thin between $x=40-60$. This thinning does effect the imaging capabilities of the differencing and coherency algorithms in that the outputs show a broken up image of the fault. This feature is less evident on the second derivative result.

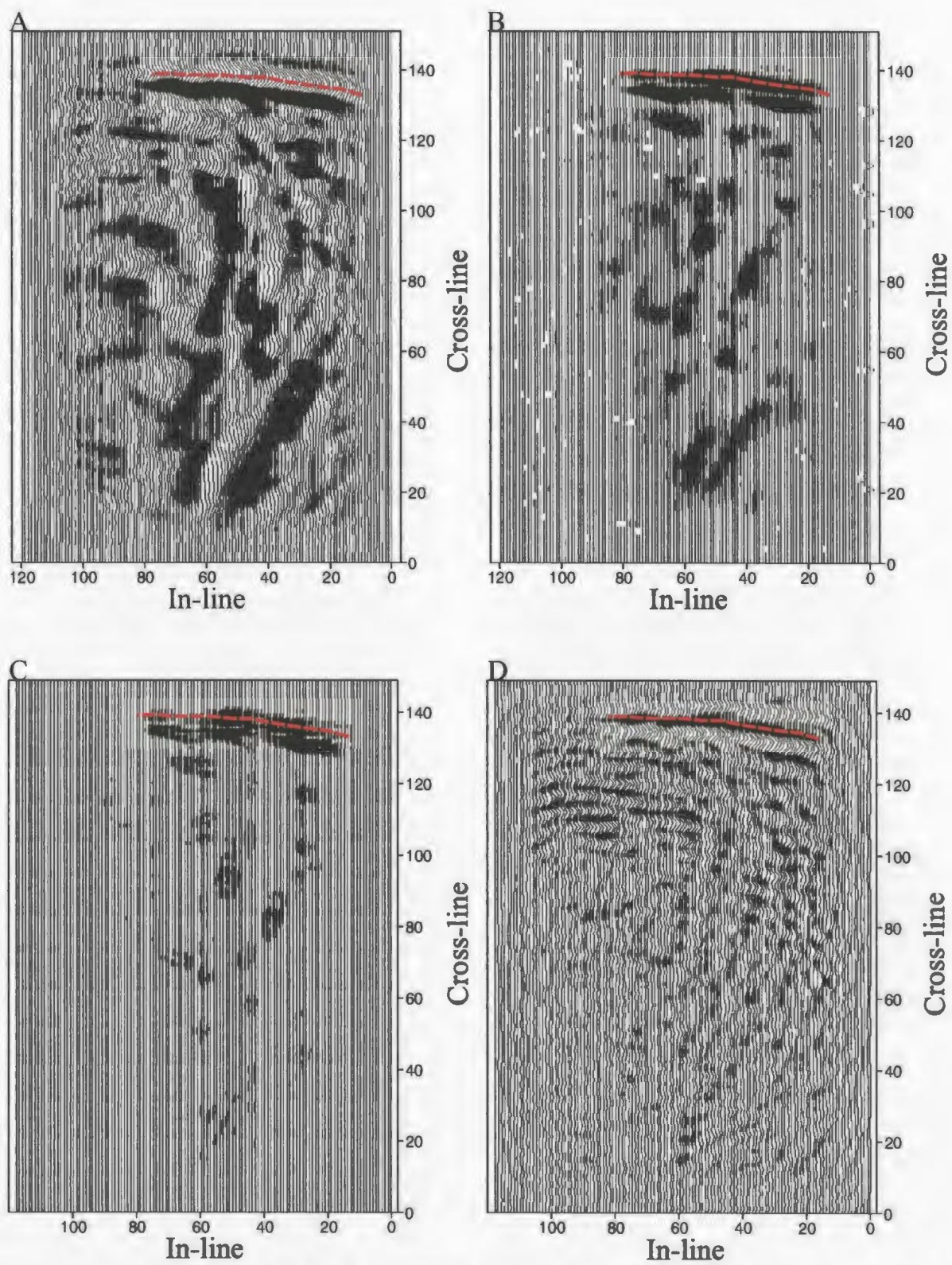


Figure 5.5: Comparison of result for depth section 275. (A) Input data, (B) coherency result, (C) differencing result, and (D) second derivative result.

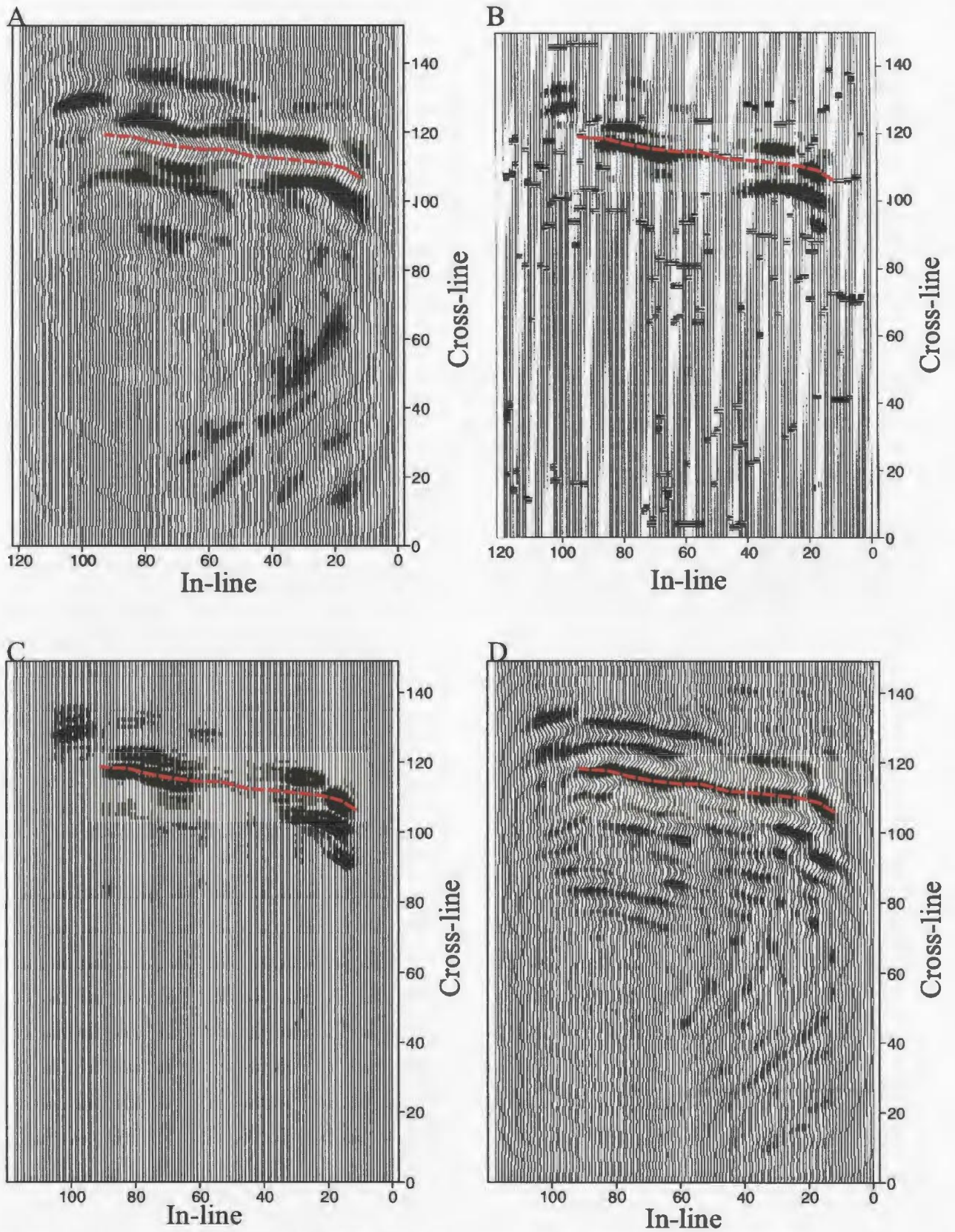


Figure 5.6: Comparison of result for depth section 325. (A) Input data, (B) coherency result, (C) differencing result, and (D) second derivative result.

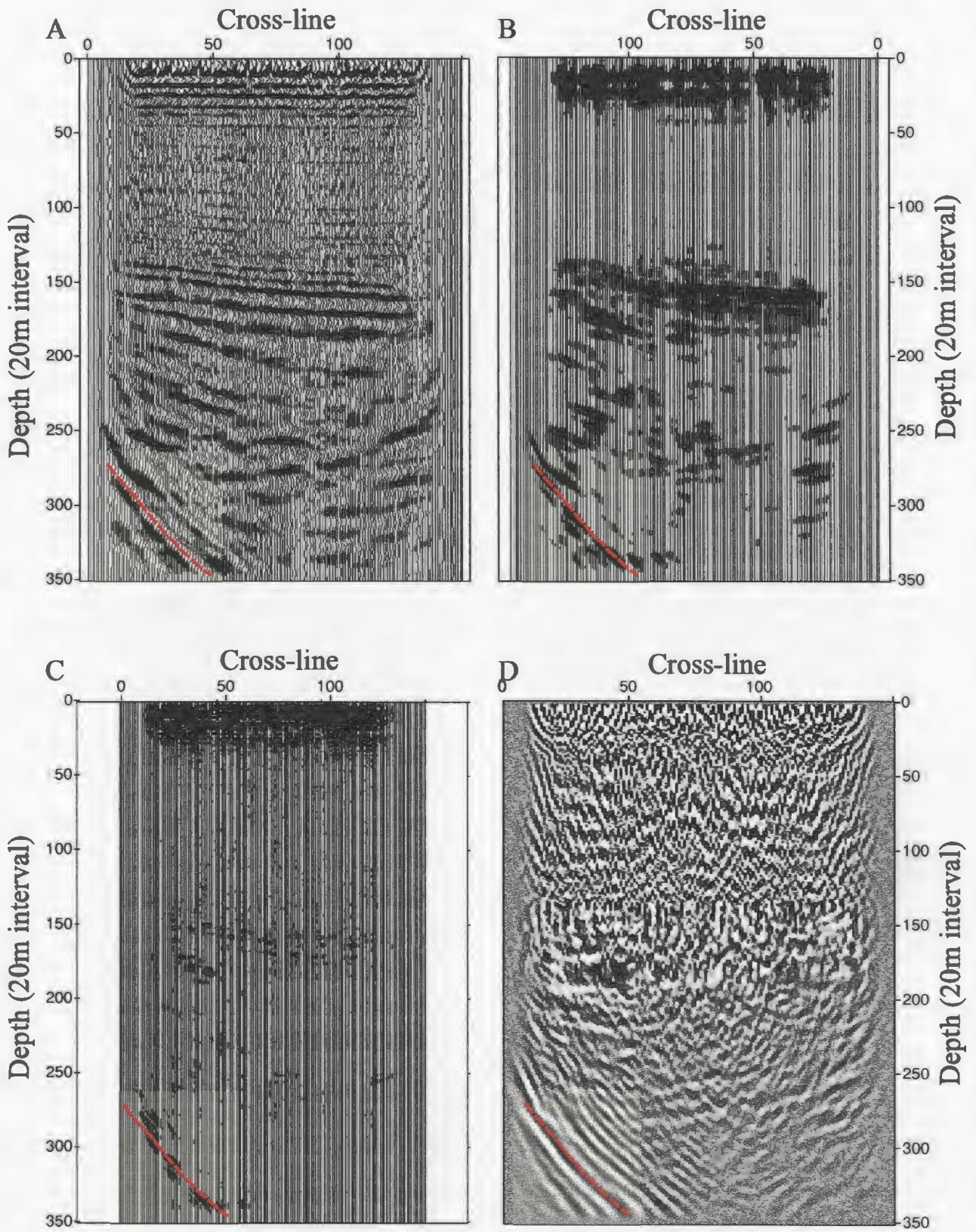


Figure 5.7: Comparison of result for in-line 60. (A) Input data, (B) coherency result, (C) differencing result, and (D) second derivative result.

The last comparison of the depth migrated result is of in-line 60. The input is illustrated in figure 5.7a. Again, the Murre fault location illustrated by a dashed line. The results of the coherency (B), differencing (C) and second derivative (D) illustrate that the Murre fault is imaged accurately. The coherency and differencing also show similar results. The differencing method appears to have high frequency oscillations, as observed in section 4.3.2. Also illustrated in Figure 5.7 is that the Murre fault not being imaged as a continuous discontinuity. This may just be amplitude scaling factor. The second derivative result does image the Murre fault as continuous but still has a lot of high frequency oscillations due to the fact that it is a second derivative.

Therefore, the above results illustrate that the second derivative method highlights the faulted event of the Murre fault. It gives a continuous fault image and does not have the longer wavelength that is illustrated by the coherency and differencing results. However the high frequency reverberations associated with the second derivative make it difficult to pick the correct phase of the wavelet. Again, deconvolution could help decrease this ambiguity if we knew the wavelet. The coherency and differencing algorithms perform well at eliminating the continuous reflections and imaging the discontinuous reflections associated with the Murre fault.

5.3 Application of Differencing and Coherency Methods to Time Migrated Data

This section describes the effects of the differencing and coherency methods to time data. The data set used was a portion of the Hibernia 1997 three-dimensional seismic survey, which was provided by Hibernia Management Development Corporation. Two subsets of the 3D seismic survey were selected, the first outlined in red as shown in

figure 5.8 consists of 300 traces, 400 lines and covers the area of the Murre fault. The second subset outlined in yellow as shown in figure 5.8 consists of 400 traces, 400 lines and is an area with smaller scale faults. Each subset had a time range of 2400 to 3000 ms with a sample rate of 4ms. The first data set was used for testing both the differencing and coherency algorithms for comparison purposes. The second data set was not available for testing using the differencing software; as a result this data was only used on the coherency software.

5.3.1 Differencing Results Using Time Migrated Data

For differencing, software called EDGE developed by Chevron Petroleum Technology Corporation was used. This deals with imaging of faults and stratigraphic changes in the subsurface. Within the software there are three methods of edge detection, amplitude differencing, super amplitude differencing, phase differencing, and derivative. To keep consistent with the previous algorithms amplitude differencing was chosen. The amplitude difference calculates trace to trace differences in the input data. To test the software, four input parameters must first be determined; vertical window sizes, trace pattern, dip steering, and edge detection attribute. First, the display attribute for the output cube was determined. The options for this input parameter are as follows: average-provides most robust result, minimum- takes minimum difference for the surrounding traces, maximum-takes maximum difference for the surrounding traces, and max-min – takes the range of the difference for the surrounding traces. Average was chosen as the output display attribute because it takes the average of the difference. This

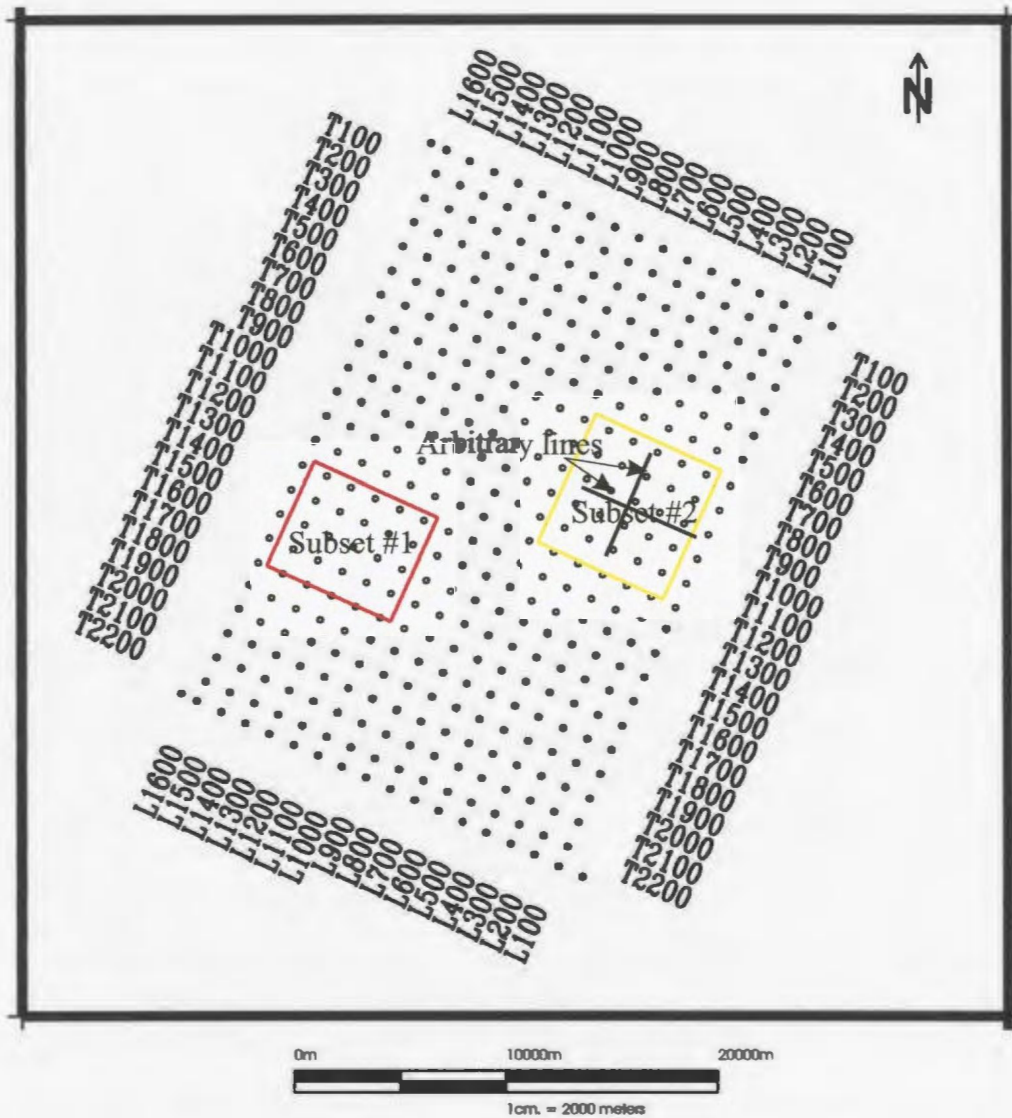


Figure 5.8: Seismic basemap of Hibernia time data. Subset #1 outlined in red, subset #2 outlined in yellow, and black line represents an arbitrary cross-line and in-line of subset #2.

improves the result through taking the average of the output data values rather than providing maximum and minimum values, which could skew results to the high or low ends. Averaging is also the most robust, therefore it is relatively insensitive to errors in the data and can deal with poor quality data. The other three input parameters were used for parameter testing. These are vertical window size (40ms, 60ms, and 80ms), trace pattern (4 corner, 3x3, and 5x5) and dip steering (dip steering on or off). Table 5.1 illustrates six of the many tests performed using the differencing software.

Results from the tests listed in table 5.1 are shown in figures 5.9, 5.10, and 5.11. The first of these tests kept all input parameters constant except for vertical window size. Figure 5.9 illustrates results of varying window size. In figure 5.9 (a) is the input data set, (b), (c), and (d) are differencing results from varying window size 80, 60 and 40ms respectively. The input data set has interpreted the Murre fault and a smaller scale fault paralleling the Murre fault, both of which are outlined by thin white lines. This is displayed as a time slice at time 2740. Each output display has correct fault interpretation outlined by either a white or black thin line. These results indicate that as the vertical window size decreases fault imaging improves. Window size is variant with the size of the structure, however if the window size is too low smaller scale faults will not be evident. Again the fault image of the differencing results are not as distinct as the input. Also the output contains higher frequency content than the input.

The next test had vertical window size (60ms) and dip steering (off) constant, with varying the comparison pattern (4-traces and 3x3). Figure 5.10 illustrates (a)-input data set, (b) differencing result with 4-traces, and (c) differencing result with 3x3 traces.

Table 5.1: Testing Parameters for Difference Method (EDGE).

Parameter	Test 1	Test 2	Test 3	Test 4	Test 5	Test 6
Comparison Option	Average	Average	Average	Average	Average	Average
Comparison Pattern	4	4	4	8	3x3	3x3
Vertical Window Size (ms)	40	60	80	80	60	60
Dip Search	No	No	No	No	No	Yes

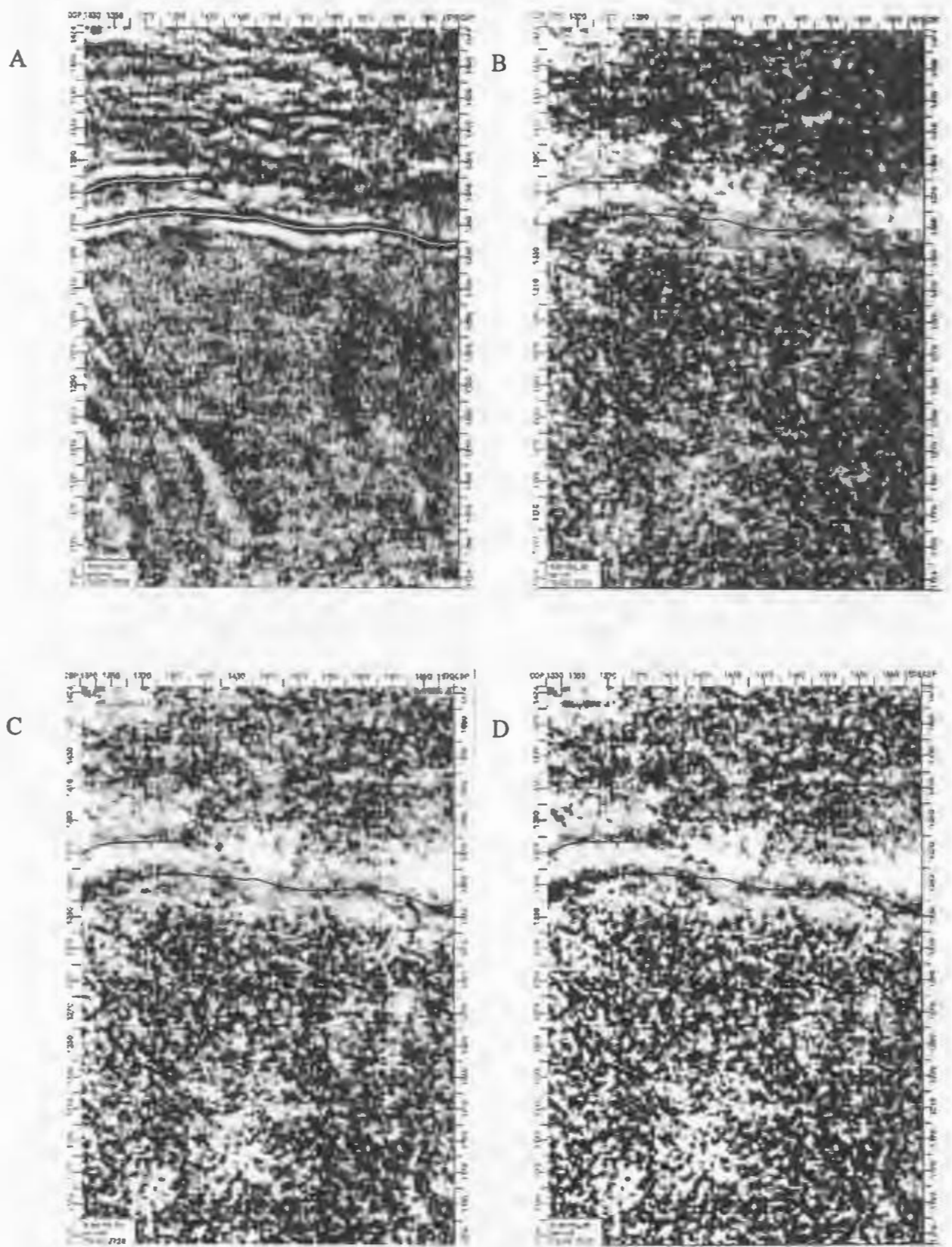


Figure 5.9: Differencing results using various window sizes. (A) Input data set, (B) 80 ms window, (C) 60 ms window, and (D) 40 ms window.

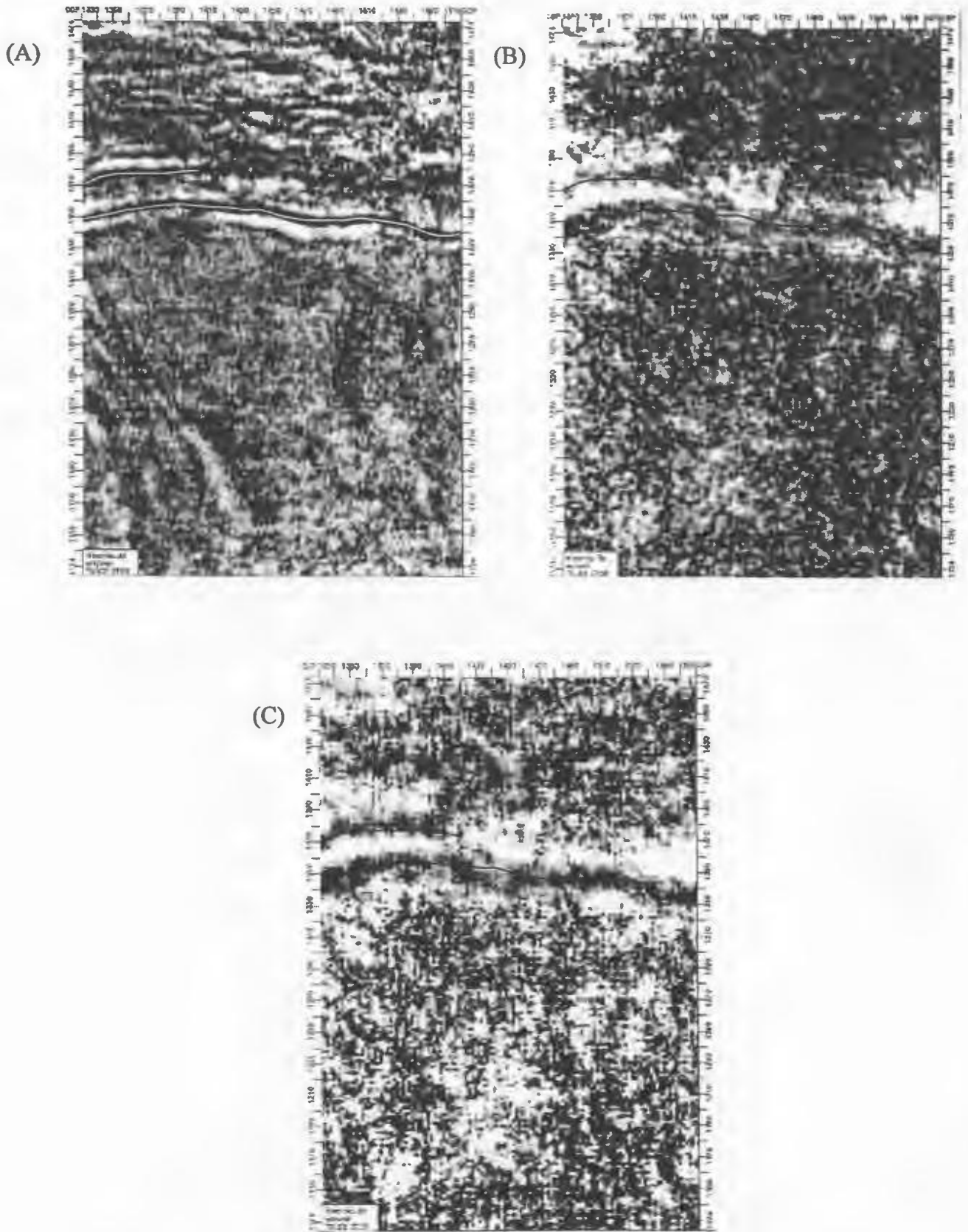


Figure 5.10: Edge results using variation comparison pattern. (A) Input data set, (B) 4 traces, and (C) 3x3 traces.

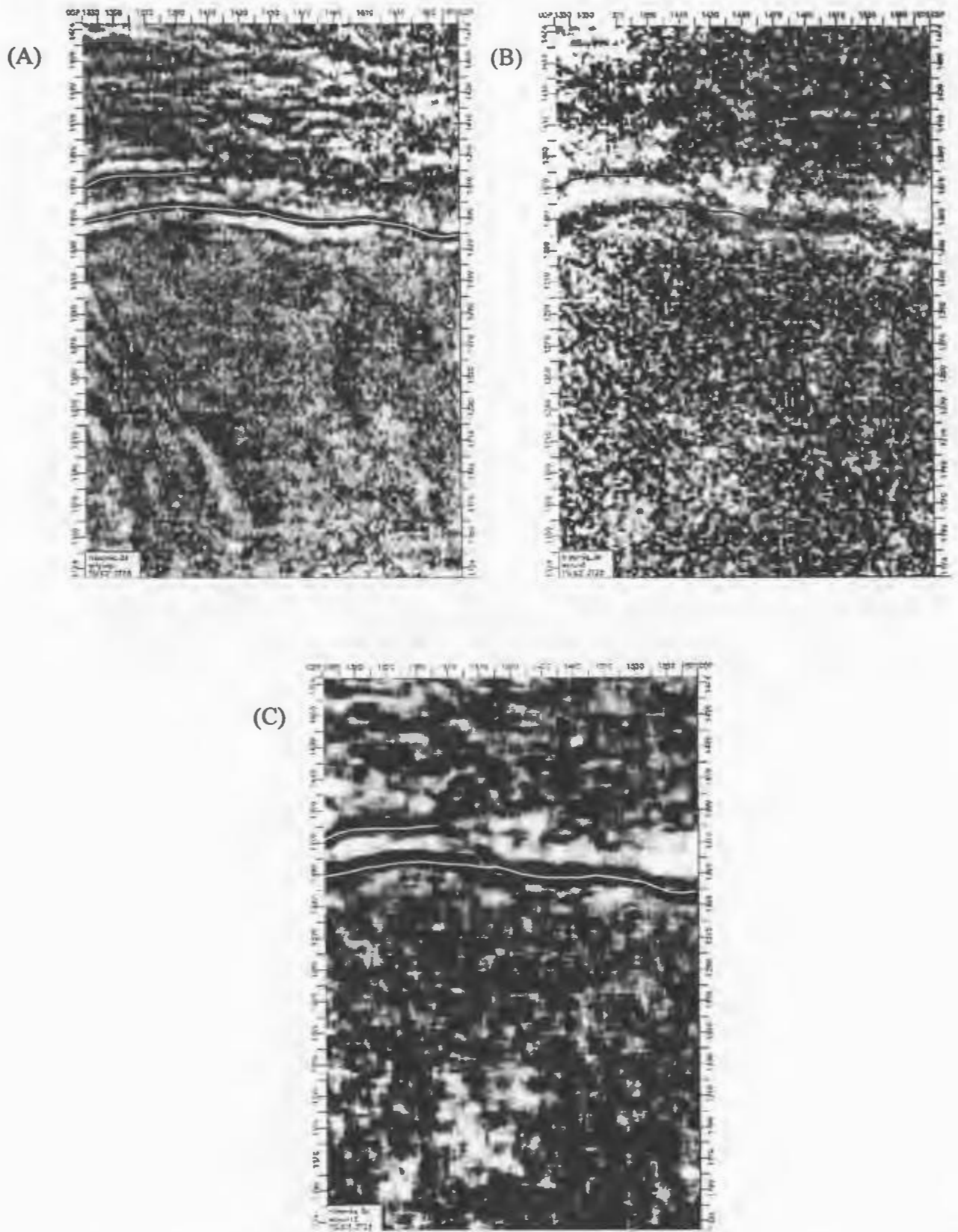


Figure 5.11: EDGE results of dip steering. (A) Input data set, (B) 3x3 with no dip steering, and (C) 3x3 with dip steering.

The results illustrate that by increasing the trace pattern the fault image becomes clearer but again the differencing result have higher frequency content than the input data set.

Dip steering was the next parameter test performed. There were numerous tests performed however the majority of results were not significant. Figure 5.11 illustrates (a) input data set, (b) 3x3 trace with no dip steering and (c) 5x5 trace with dip steering. Both have a vertical window size of 60 ms

Parameter testing of the Edge software illustrated that the best parameters are low vertical window size (40ms), greater number of traces (3x3 or 5x5) and dip steering toggled on to give best result for fault imaging.

5.3.2 Coherency Results Using Time Migrated Data

To test coherency results using time data, Landmark's Poststack/PAL was used. This software was designed to help extract more useful information from seismic data and is used to enhance resolution with the add on feature on continuity which reveals and heightens lateral changes in the data. The subset #1 as previously show in section 5.3.1 was used as input into the Poststack/PAL software.

As previously illustrated with EDGE, Poststack/PAL also has several input parameters that must be determined. Many are similar to EDGE, such as the comparison option, comparison pattern, vertical window size, and maximum dip search. Other parameters that need to be determined for Poststack/Pal includes amplitude scaling and normalization value. These parameters must be determined first since they effect the performance of the software with respect to the other parameter testing. To determine the amplitude scaling and normalization value a workflow for determining the best continuity

parameters written by Gallagher (1996) was used. The workflow is outlined in Appendix A. These values are important for scaling the output coherency. These values are both negative and positive with positive values ranging from 0.20 to 0.95 being ideal.

Therefore to utilize the color bar within Landmark, coherency values need to be scaled so that non-ideal negative values are clipped from the output. Following the workflow in Appendix A the values for amplitude scaling and normalization were determined to be 0.25 and 0.75 respectively. For these data only coherency values between 0.50 and 0.75 will be utilized by the color bar. Figure 5.12 illustrates the effects of using the amplitude scaling and normalization values (A), as opposed to not using any of the parameter's value (B). It is shown that the use of a values of .025 for amplitude scaling and 0.75 for normalization, the data has the full range of the color bar. This compares to no amplitude scaling or normalization value (B), which tends to only use the upper portion of the color bar.

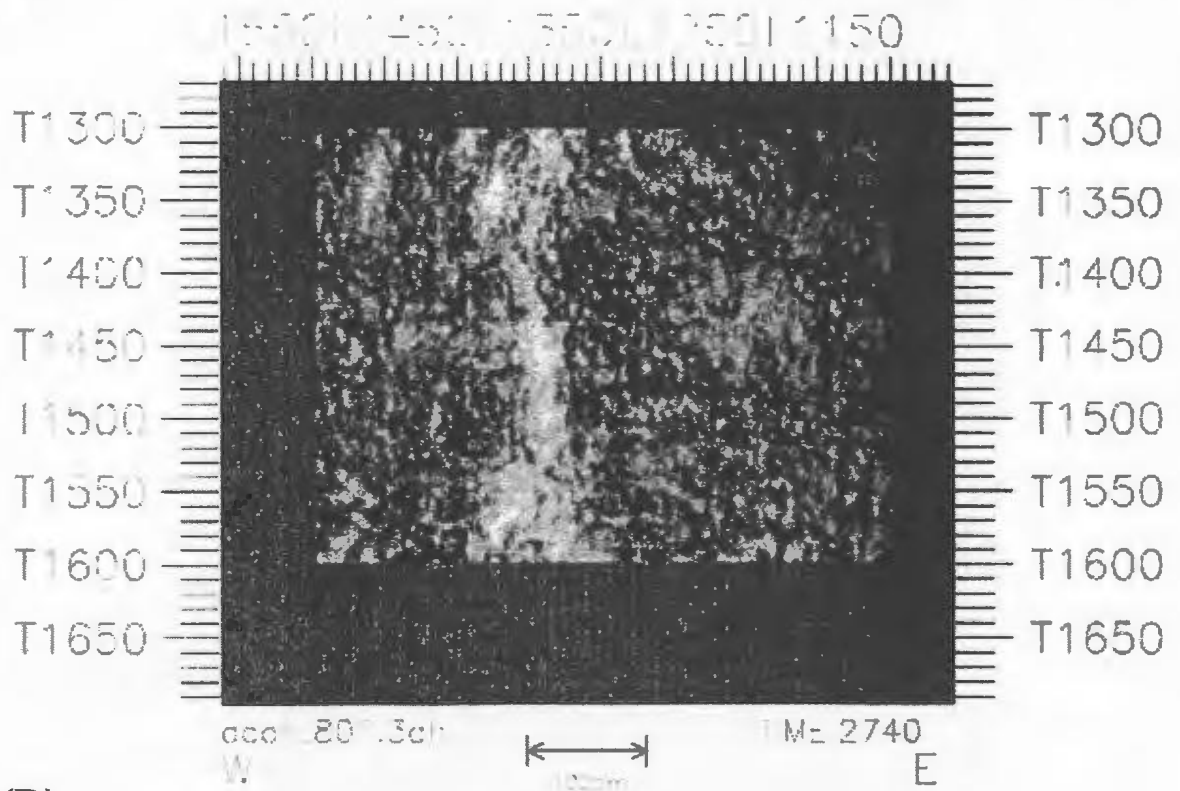
Now that the amplitude scaling and normalization value has been determined, parameter testing can begin. Table 5.2 illustrates testing of coherency using correlation and semblance. Semblance had not been used prior to this, however but since it was available within Landmark's Poststack/PAL, it was used in testing Hibernia's time data. Semblance was explained in chapter 2 section 2.2.2. Tests 1-3 are coherency testing and tests 4-6 are semblance as illustrated in table 5.2. Table 5.2 illustrates that the only parameter used for testing was vertical window size. All tests have a comparison option of average with a comparison option of eight. Eight was chosen for the comparison pattern since the greater number of traces the more robust the results. Also shown is a

Table 5.2: Testing Parameters for Coherency Method (Poststack/PAL).

Parameter	Test 1	Test 2	Test 3	Test 4
Coherency	Correlation	Correlation	Correlation	Semblance
Comparison Option	Average	Average	Average	Average
Comparison Pattern	8	8	8	8
Vertical Window Size (ms)	50	76	150	50
Maximum Dip Search	8	8	8	8
Threshold Applied	0.25	0.25	0.25	0.25
Normalization Value	0.75	0.75	0.75	0.75

Parameter	Test 5	Test 6	Test 7	Test 8
Coherency	Semblance	Semblance	Correlation	Correlation
Comparison Option	Average	Average	Average	Average
Comparison Pattern	8	8	8	8
Vertical Window Size (ms)	76	150	76	76
Maximum Dip Search	8	8	No	8
Threshold Applied	0.25	0.25	0.25	0
Normalization Value	0.75	0.75	0.75	0

(A)



(B)

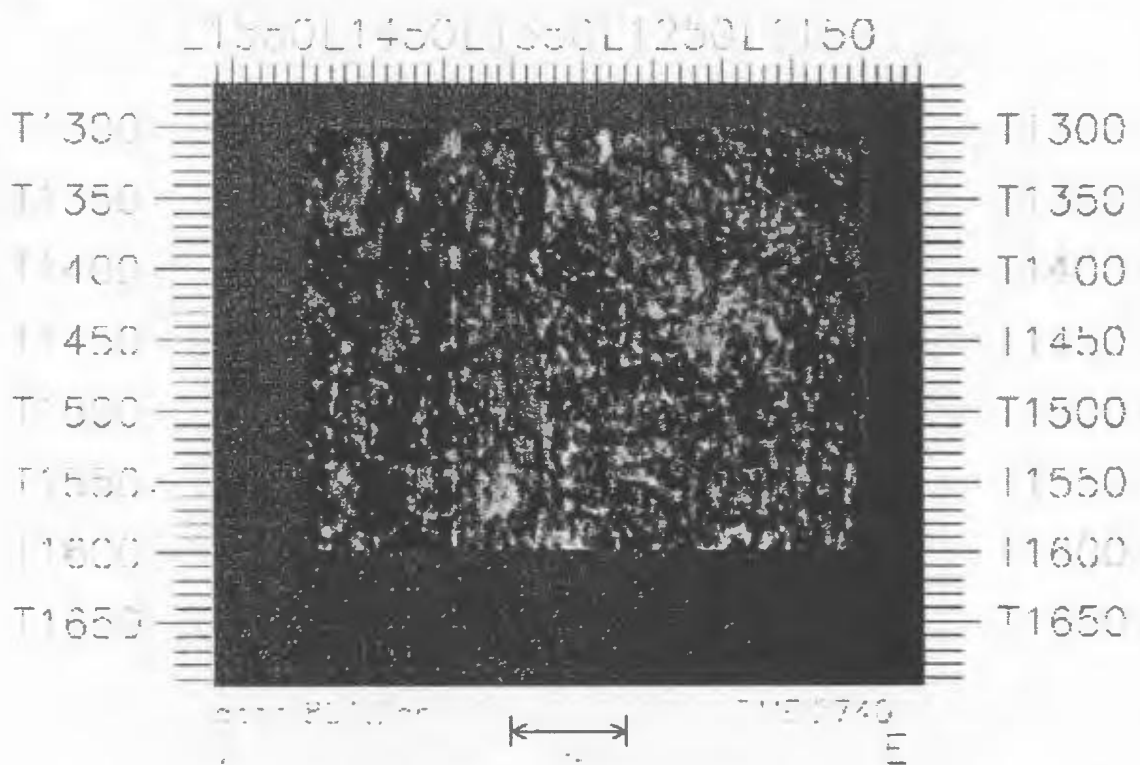


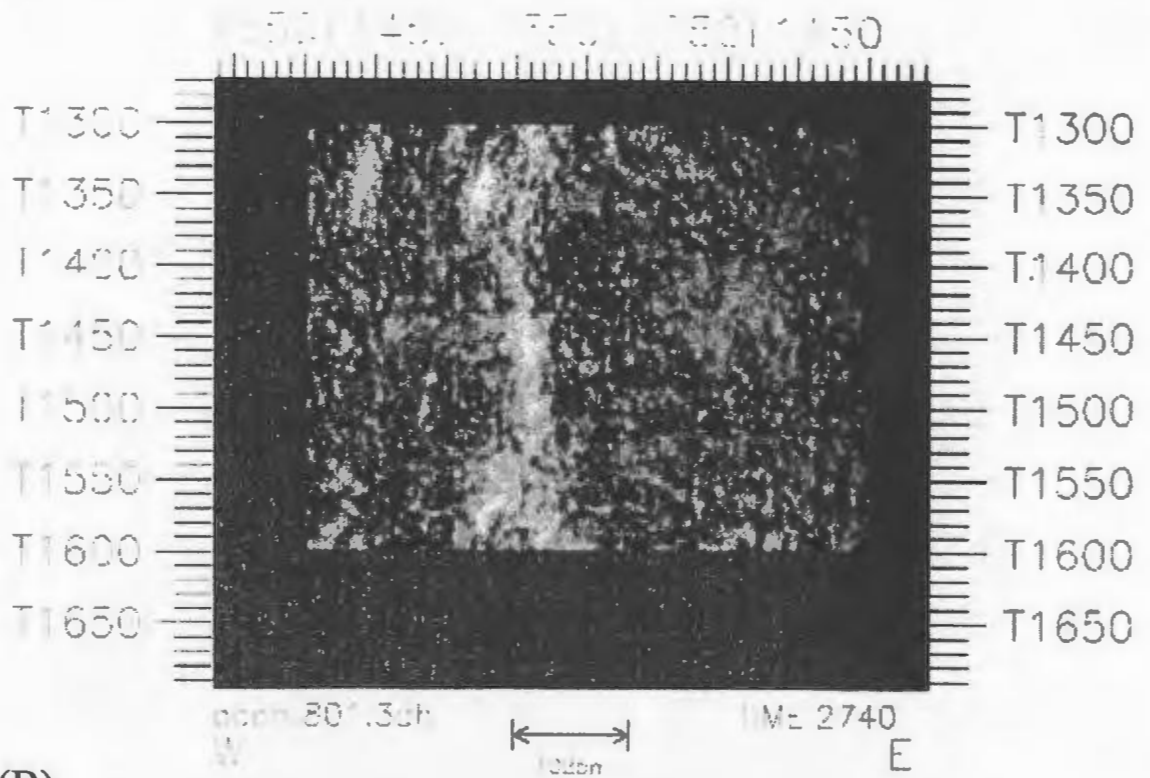
Figure 5.12: Illustration of the effects of using amplifying scaling and normalization value of 0.25 and 0.75 (A) as compared to not using parameter values (B).

maximum dip of 8ms. This value was chosen to be equal to the maximum geological dip (in ms/trace) that is expected to occur within the maximum distance of the comparison pattern (Landmark, 1996) within the input data set. Therefore a 8ms-dip search was chosen for this data. Figure 5.13 illustrates the effects of not using dip steering.

Figure 5.14 illustrates the correlation results of varying vertical window size, (a) is the input data, and (b), (c), and (d) are coherency results of vertical window sizes of 76, 50 and 150. These results illustrate that a shorter window size provides a very sensitive measure of trace to trace dissimilarity, but may be bias from noise effects. A longer windows reduces the risk of noise effects, but tends to obscure more subtle discontinuities. Semblance was also tested using Poststack/PAL, with results similar to correlation. Figure 5.15 illustrates comparison of correlation and semblance using subset #1 shown in (A). Correlation result are shown in (B) and semblance results are shown in (C). From this comparison it is evident that both results are similar with respect to the fault image. The difference between the results is in the darkness of the output. Correlation tends to be darker in color than semblance.

Both correlation and semblance did not obtain the best results for imaging the Murre fault. The cause of this is found by examining the time data, which illustrates that the Murre fault appears to be an imaged event and therefore will not produce an adequate image using the coherency method. Therefore, with respect to the imaging capabilities of Landmarks Poststack/PAL, a subset #2 was used (figure 5.1). This data set illustrates several smaller scale faults, as seen in figure 5.16 (A). These features include what looks like north-south trending and east-west trending faults or stratigraphic features. Figure 5.16 illustrates semblance results of varying window size using subset #2 as input. The

(A)



(B)

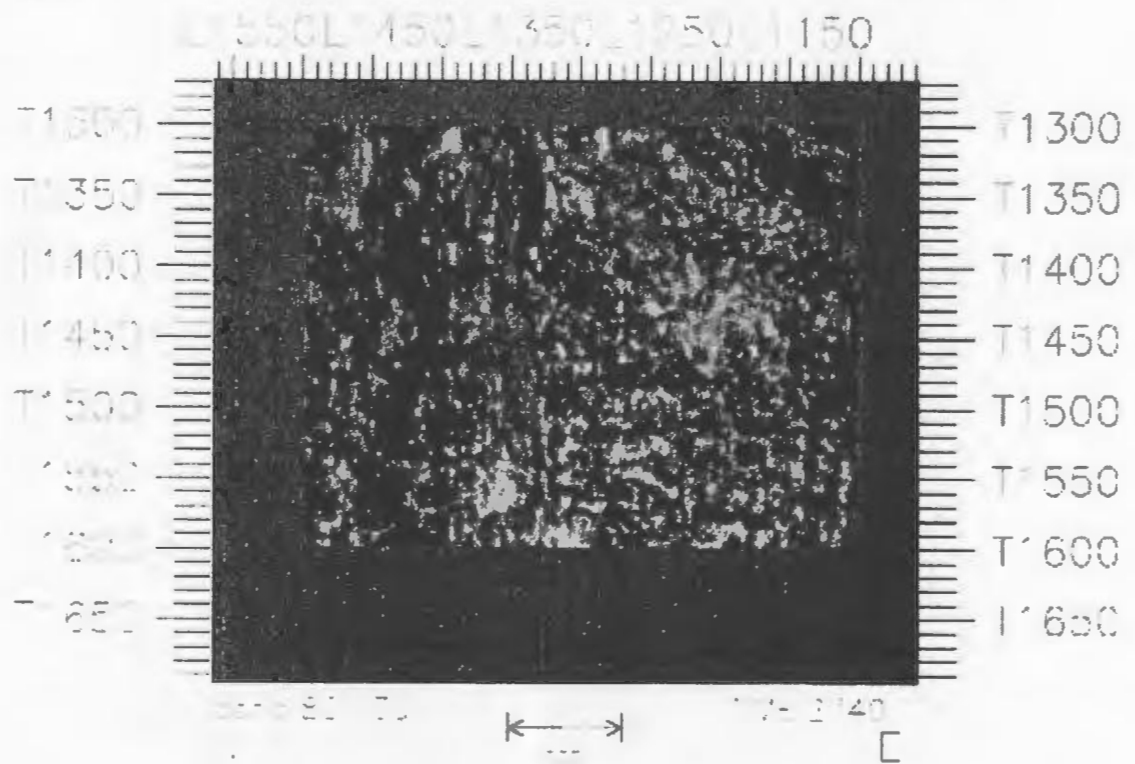


Figure 5.13: Illustration of the effects of using dip steering (A) as compared to no dip steering (B).

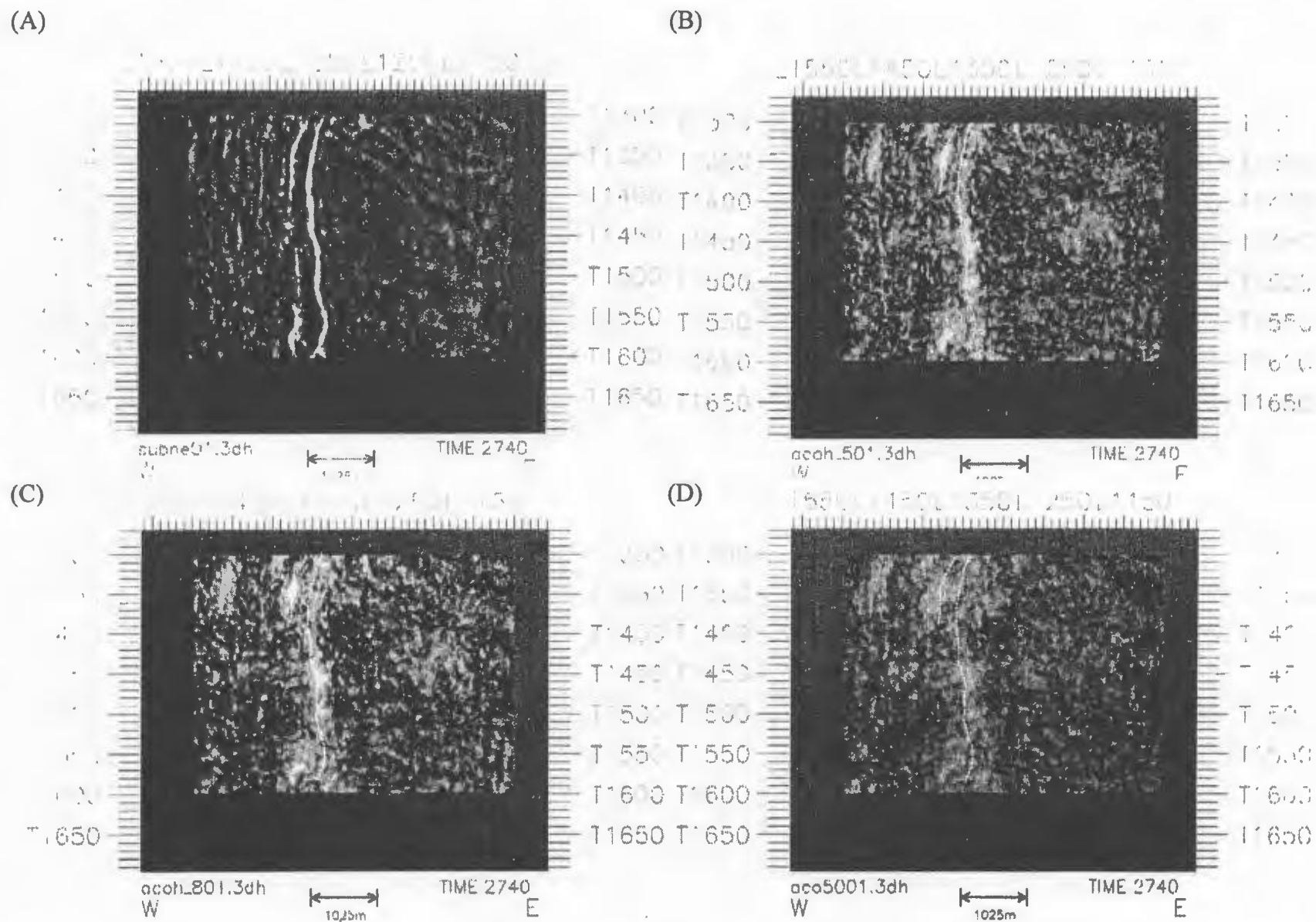


Figure 5.14: Poststack/PAL results due to varying vertical window size. (A) Input data set, (B) 50ms, (C) 76ms and (D) 150ms. Dashed line represents location of Murre fault and smaller parallel fault.

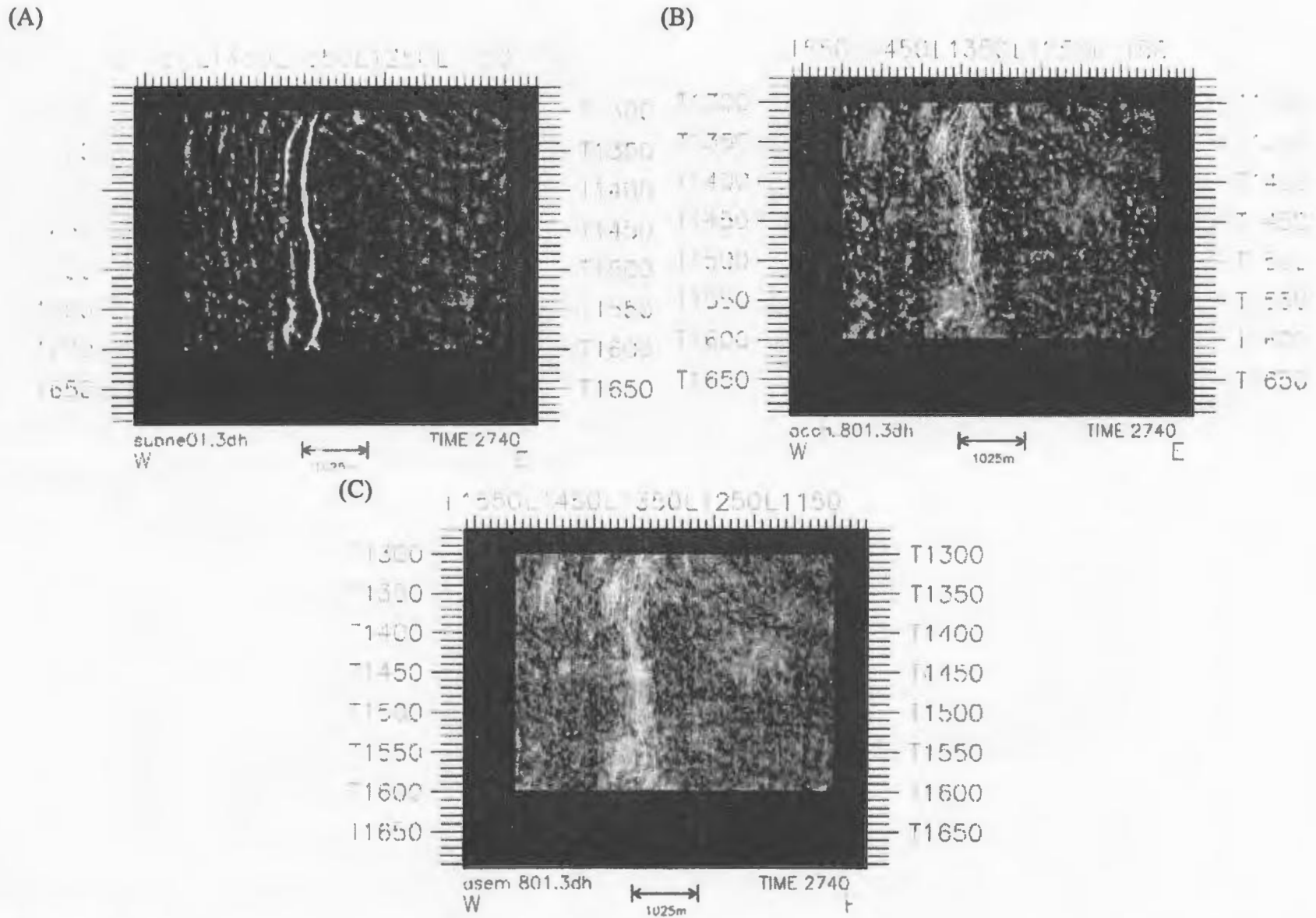


Figure 5.15: Poststack/PAL results of correlation vs. semblance. (A) Input data set, (B) correlation result, (C) semblance result. Dashed line represents location of Murre fault and smaller parallel fault.

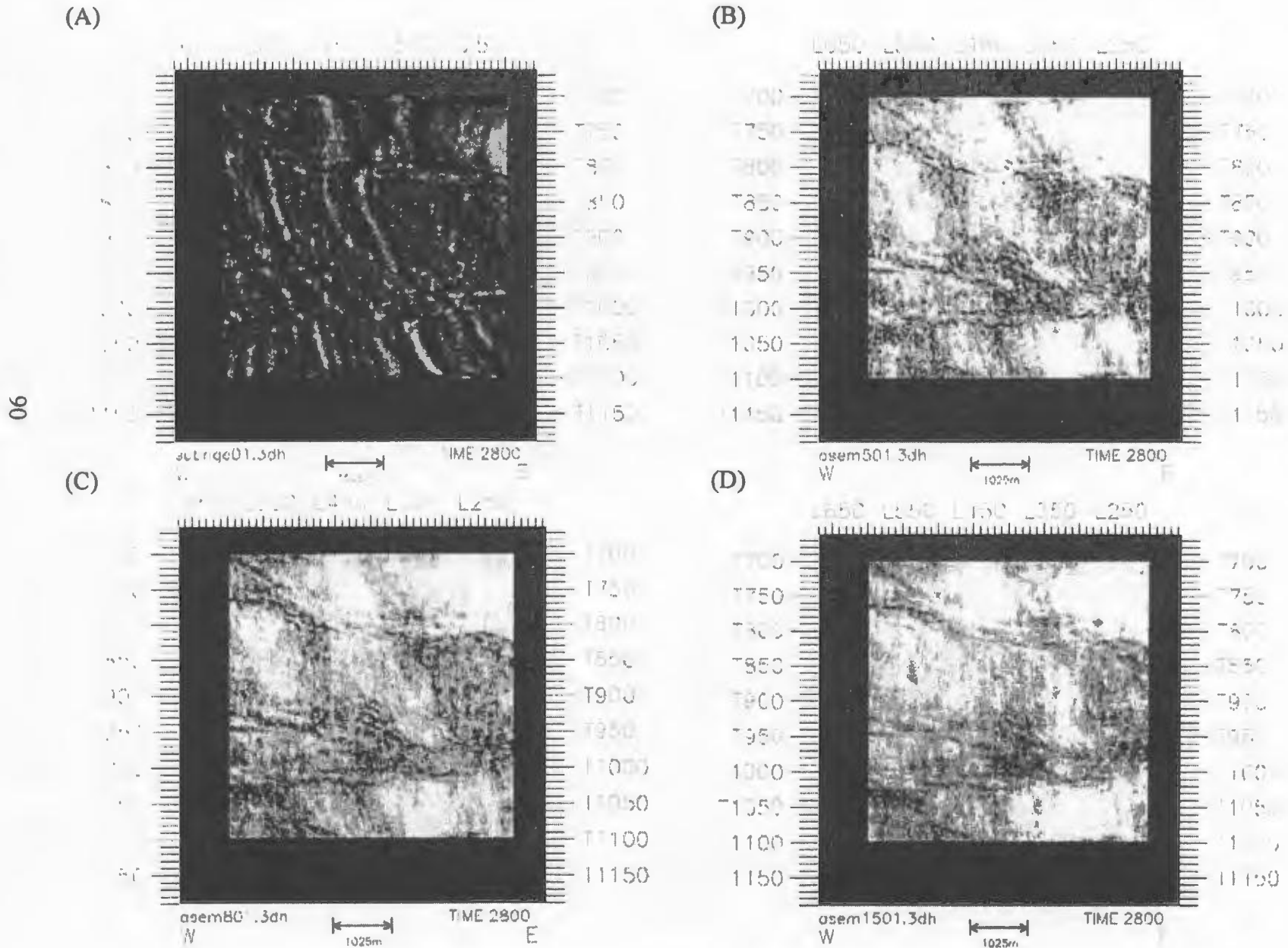


Figure 5.16: Semblance results of subset #2 (A) with varying window sizes. (B) 50 ms window, (C) 76 ms window, and (D) 150 ms window.

window sizes used were (B) 50 ms, (C) 76 ms, and (D) 150 ms. Figure 5.16 shows that as window size decreases the sharper the image. Having a very large window size (150 ms) tends to lose features that are seen with results of smaller window sizes (50 –80 ms). This is illustrated more clearly in figure 5.17, where inlines of subset #2 for each of the result seen in figure 5.16. Therefore using a smaller vertical window size the data will tend to be less averaged.

5.3.3 Comparison of EDGE Vs Poststack/PAL

Comparison results of using EDGE and Poststack/PAL are illustrated in figure 5.18. This shows the input data set (A) of subset #1, (B) EDGE result, and (C) Poststack/PAL result. Results have same vertical window size (80 ms) and comparison traces (8-trace). Poststack has a 8ms dip steering whereas EDGE has dip steering toggled off. The results show that even with the difference in dip steering both software programs produce very similar results for the Murre fault.

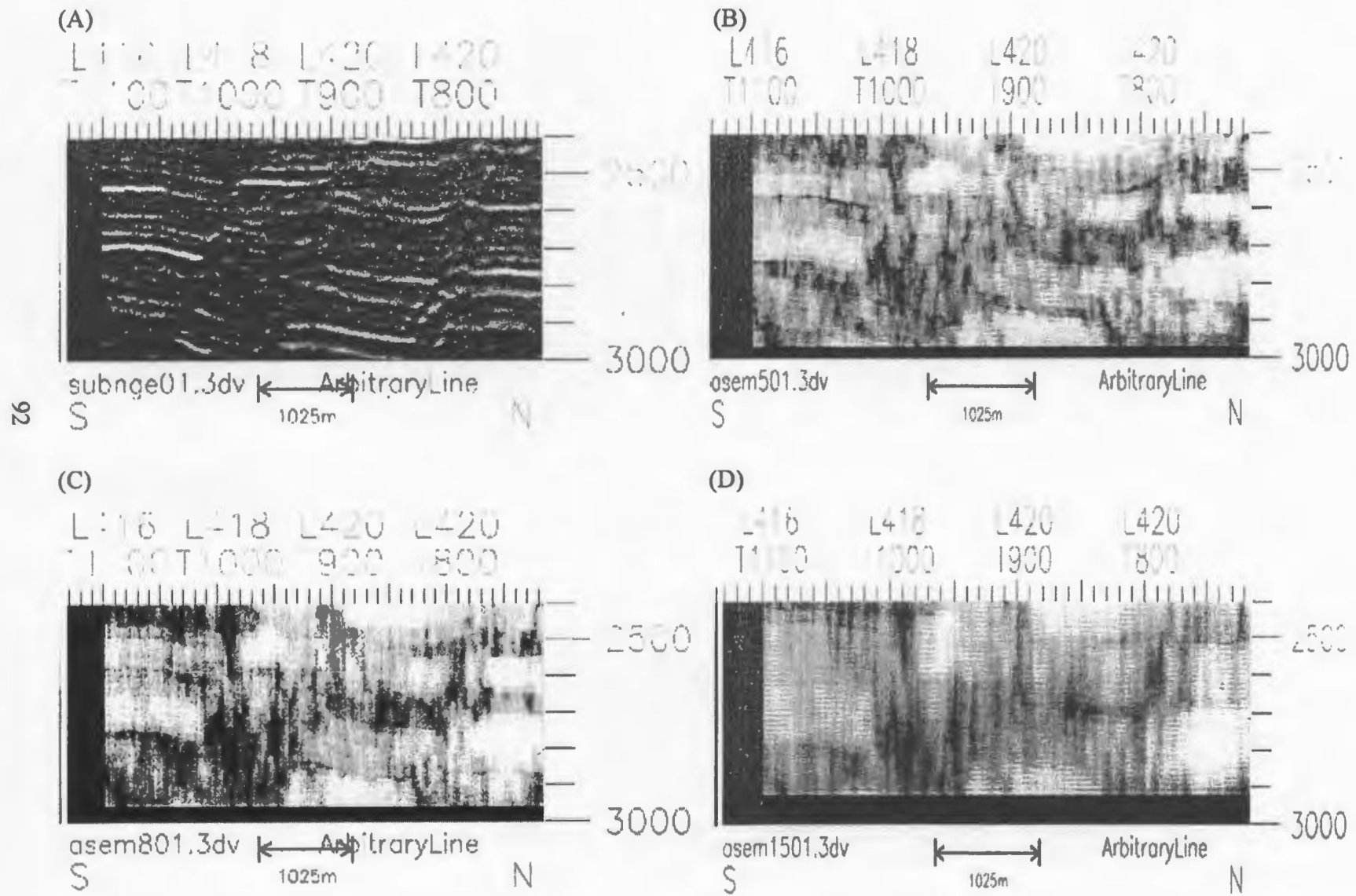


Figure 5.17: Arbitrary line illustrating the effects of varying window size to (A) input data, (B) 50 ms window, (C) 76 ms window, and (D) 150 ms window.

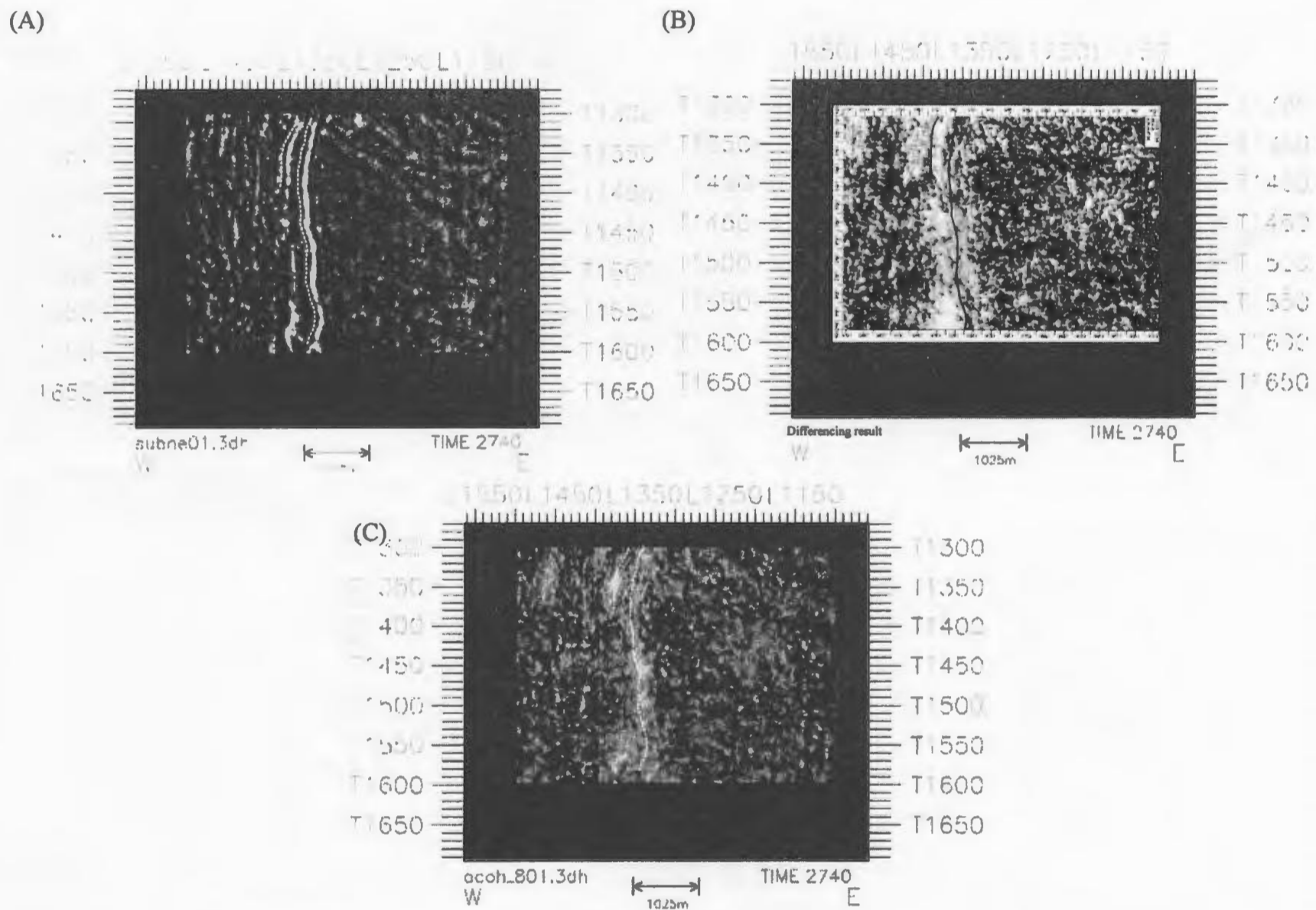


Figure 5.18: Comparison of EDGE (B) and Poststack/PAL (C) results. Input data in show in (A).

Chapter 6

Discussion and Conclusions

6.1 Effects of imaging on fault detection.

Fault detection imaging is extremely useful in areas where faults effect field development and production. It has been shown that the use of fault detection methods is important in areas where faults are not easily imaged using traditional seismic data. Fault detection highlights faults that otherwise may not be interpreted or eliminates features that look like faults on time data as illustrated in section 5.32. In order for such imaging methods to produce their best results the data must be properly processed which means migrating the data before using fault detection. Migration is very important to the outcome quality of the fault detection methods as seen in section 4.1; the migrated model produced a better image of the fault model than the unmigrated model where the fault detection of a migrated and unmigrated section was compared. Other effects of imaging on fault detection involve the type of data used, three-dimensional data is better than two-dimensional because three-dimensional data can provide time or depth slices of the data, therefore allowing observation of lateral extent of fault planes.

6.2 Comparison of Methods

Several different methods of fault detection were tested. They were coherency measures, differencing, second derivative, and semblance. For the model data, coherency, differencing, and second derivatives were tested and compared. The results illustrated that the second derivative result gave the most continuous image of the Murre fault, but suffered from reverberations. All three methods did a good job at eliminating the coherent events, but differencing had a problem with high frequency oscillations.

The coherency method also had a problem with a fault shadow located above the Murre fault.

The depth migrated real data also tested coherency, differencing, and second derivatives. These results illustrated that the coherency method produced the best results. The second derivative produced high frequency oscillations, which are due to the increased noise within the real data as compared to the model data. The differencing method as seen with the model also produced high frequency oscillations.

Testing of the software EDGE (differencing algorithm) and Poststack/PAL (both coherency and semblance) was done using time migrated data. These results did not produce good images of the Murre fault since due to the nature of the fault there tends to be a coherent image within this data set. Results did show however that as vertical window size decreased, comparison trace increased, and dip steering was used the image improved. Also results for the coherency algorithm and semblance algorithm were very similar. By using subset #2 (figure 5.8) the imaging qualities of Poststack/PAL, proved to increase dramatically. Subset #2 contained features that could be interpreted as faults on the time data but when coherency was used these features/faults were very evident and easy to interpret.

6.3 Recommendations

Using model and real data the algorithm's developed by Lines, produced data results which illustrated high frequency oscillations. This may be remedied by using deconvolution as seen in section 4.4 and illustrated in figure 4.26. The deconvolution result did eliminate the high frequency oscillations by compressing the oscillating events

into one dominant peak. Again, the real data requires knowledge of the wavelet.

Deconvolution is designed to improve the resolution of reflected events and to rid the data of unwanted energy. Through the use of software products and time data these high frequency oscillations were removed, eliminating their effects.

To obtain maximum results using fault detection methods, the following features should be considered; type of data (2D or 3D), if there are faulting or stratigraphic features present, proper processing of the data (migration), and proper input parameters determined for the data set. One should be aware that fault detection methods are only a tool to aid in fault identification and should not be used as a first interpretation

In general, the fault detection methods enhanced the amplitude of seismic events representing faults relative to continuous seismic reflections. In some cases, there may be 'ringy' seismic events that parallel the fault and it is difficult to pick the right peak or trough to trace the fault. As mentioned, deconvolution can help to compress the interpreted event. However, it is helpful to use well ties to pin the correct location of the fault. In this respect, interpretation of fault enhanced seismic sections is no different from conventional interpretation where one uses all available information to iron out possible ambiguities. Fortunately, there is a considerable amount of well information in Hibernia field to aid our interpretation.

References

- Arthur K.R., Cole, D.R., Henderson, G.G.L., and Kushnir, D.W., 1982, Geology of the Hibernia discovery, in *The deliberate search for the subtle trap*, AAPG Memoir 32, edited by M.T. Halbouty, 181-195.
- Baysal, E., Kosloff, D.D., and Sherwood, W.C., 1983, Reverse time migration, *Geophysics*, 48, 1514-1524.
- Bell, J.S. and Campbell, G.R., 1990, Geology of the continental margin of eastern Canada, in *Geology of Canada*, No.2, edited by M.J. Keen and G.L. Williams, 693-704, Geological Society of Canada, Ottawa, Canada.
- Benteau, R.I. and Sheppard, M.G., 1982, Hibernia: a petrophysical and geological review, *Journal of Canadian Petroleum Technology*, 21, 59-72.
- Bahorich, M.S. and Farmer, S.L., 1995. 3D seismic discontinuity for faults and stratigraphic features: the coherence cube, *Leading Edge*, vol.4, 10, 1053-1058.
- C-NOPB (Canada-Newfoundland Offshore Petroleum Board), 1992, Poster Display in Earth Science Building, Memorial University of Newfoundland, St.John's, Newfoundland.
- Claerbout, J.F., 1976. *Fundamentals of geophysical data processing*. New York, McGraw-Hill.
- Creaney, S. and Allison, B.H., 1987, An organic geochemical model of oil generation in the Avalon/Flemish Pass sub-basins, east coast Canada, *Bulletin of Canadian Petroleum Geology*, 35, 12-23.
- Enachescu, M.E. 1987. Tectonic and structural framework of the northeast Newfoundland continental margin. In: Beaumont, C. and Tankard, A.J. (eds), *Sedimentary Basins and Basin-forming Mechanisms*. Canadian Society of Petroleum Geophysicists, Memoir 12, 117-146.
- Gallagher, M., 1996, Work flow for determining the best continuity parameters to build continuity cube data (cd) files. *Landmark user notes*.
- Hurley, T.J., Kresia, R.D., Taylor, G.G., and Yates, W.R.L., 1992, The reservoir geology and geophysical of the Hibernia field, offshore Newfoundland, in *Giant oil and gas fields of the decade*, AAPG Memoir 54, edited by Michael T. Halbouty, 35-54.
- Jain, A.K., 1989. *Fundamentals of digital image processing*. Englewood Cliffs, N.J., Prentice-Hall.

- Kelly, I.G., 1998, Modeling and Migration of Hibernia Seismic data. MSc. thesis, Memorial University of Newfoundland.
- Landmark, 1996. User guide, Poststack/PAL. Landmark Graphics Corporation, Houston, Texas.
- Lou, Y., Higgs, W.G., and Kowalik, W.S., 1996, Edge detection and stratigraphic analysis using 3D seismic data, SEG Expanded Abstract, 324-331.
- Marfurt, K., Kirlin, R.L., Farmer, S.L., and Barorich, M.S., 1995, 3-D seismic attributes using a running window semblance algorithm, Geoscience Technology Bulletin F94-G43.
- Marfurt, K., Kirlin, R.L., Farmer, S.L., and Barorich, M.S., 1998, 3D seismic attributes using a semblance based coherency algorithm, Geophysics, 63, 1150-1165.
- McMechan, G.A., 1983, Migration by extrapolation of time-dependant boundary values, Geophysical Prospecting, 31, 413-420.
- Pratt, W.K., 1991. Digital image processing. New York, John Wiley and Sons.
- Regone, C.J., 1994. Measuring the effect of 3-D coherent noise on seismic data quality: Presented at 64 Ann. Internat. Mtg.Soc.Expl.Geophys. workshop: Processing in mountainous trust areas.
- Robinson, E.A., and Treitel, S., 1980. Geophysical signal analysis. Englewood Cliffs, N.J., Prentice-Hall.
- Russ, J.C., 1995. The image processing handbook, 2nd edition. Boca Raton, Fla., CRC Press.
- Sheriff, R. E., 1991. Encyclopedic dictionary of exploration geophysics, 3rd ed. Tulsa, SEG.
- Sheriff, R.E., and Geldart, L.P., 1983. Exploration seismology, vol. 2: Data processing. Cambridge University Press.
- Sinclair, I.K., 1994, Tectonism and sedimentation in the Jeanne d'Arc basin, Grand Banks of Newfoundland, Ph.D. thesis, University of Aberdeen.
- Sinclair, I.K. 1995. Transpressional inversional due to episodic rotation of extensional stresses in Jeanne d'Arc Basin, offshore Newfoundland, In: Buchanan, J.G. and Bauchanan, P.G. (eds.), Basin Inversion, Geological Society of London, Special Publications, 88, 249-271.

Taner, M.T., Koehler, F, and Sheriff, R.E., 1979. Complex seismic trace analysis: *Geophysics*, 44, 1041-1063.

Tankard, A.J, and Welsink, H.J., 1987, Extensional tectonics and stratigraphy of Hibernia oil field, Grand Banks, Newfoundland, *AAPG Bullentin*, 71, 1210-1232.

Telford, W.M., Geldart, L.P., Sheriff, R.E., and Keys, D.A., 1976. *Applied Geophysics*, Cambridge University Press.

Von der Dick, H. and Meloche, J.D., 1986, Generation, migration, and expulsion of hydrocarbons in the Hibernia field, 1986 CSPG Convention Programs and Abstracts, p.38.

Whitmore, N.D., 1983, Iterative depth migration by backward time propagation: 53rd Ann. Internat. Mtg., Soc. Expl. Geophys. Expanded Abstracts, 382-385.

Yilmaz, O., 1987. *Seismic data processing*. Tulsa, SEG publication.

Appendix A

Work Flow for Determining the Best Continuity Parameters to Build Continuity Cube Data (cd) Files

I. **Subset 3DV file**: You want to select a subset of your original 3DV file (orig01.3DV). The smaller bulk shifted subset 3DV file (subBS01.3DV) will be used as input for repeated continuity flows to determine the best parameters.

A - Select small area in mapview ($L_n - L_m / T_r - T_s$)

B - Determine center of time window (t_0) for your zones of interest.

EXAMPLE: ($t_0 = 1000\text{ms}$)

C - Determine correlation window size (W_{corr}). Consider the wavelength of the seismic data and that a smaller correlation window resolves more detail.

EXAMPLE: ($W_{\text{corr}} = 100\text{ms}$)

D - The top of your subsetted data ($t_{\text{top}} = t_0 - W_{\text{corr}}$)

The bottom of your subsetted data ($t_{\text{bot}} = t_0 + W_{\text{corr}}$)

The "thickness" of the subsetted 3DV file should be at least two times the size of the correlation window.

See Figure 1

[Throughout this document the asterisk "*" means to: 1) select this option 2) push button or 3) input value in window].

II. **Bulk shift 3DV subset**: You will bulk shift the 3DV subset to zero time.

A - Launch: PostStack; Main PostStack/PAL Window

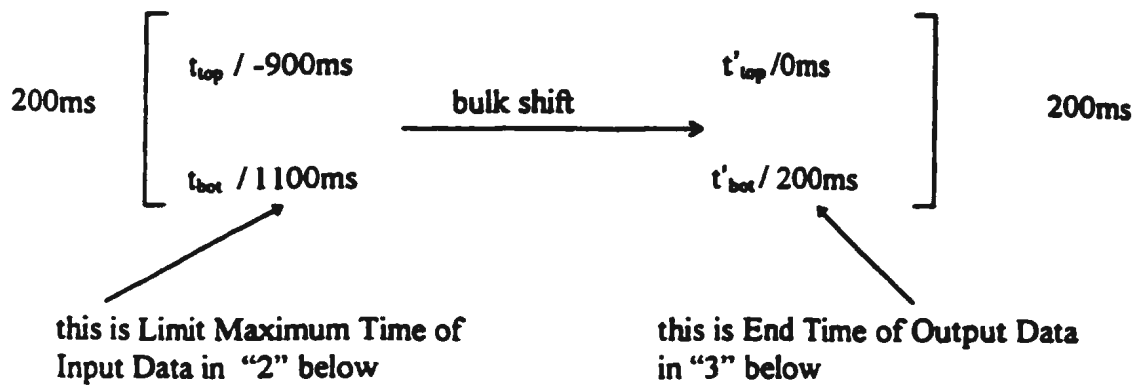
1. * Process

* Data Shifting

* Bulk Time Shift

* Parameters

- * - 900 (negative bulk shift zone of interest so that $t'_{\text{top}} = 0$, zero time)



2 *Input Data

* Vertical File

* Parameters

- Input File \rightarrow * List \rightarrow * orig01.3DV
- * Line/Areal Extents
- Input direction \rightarrow * Lines
- Areal Extent \rightarrow Lines * L_n * L_m
 \rightarrow Traces * T_r * T_s
- * Limit Maximum Time * t_{bot} (1100ms)
- * Fill Gaps with Dead Traces
- * OK
- * OK (Input Data)

3. * Output Data

* Vertical File

* Parameters

- Output File \rightarrow * (Name new file) subBS01.3DV
- Start Time \rightarrow * 0ms
- End Time \rightarrow * 200ms
- Format \rightarrow * 8 bitdata must be scaled if 8 or 16 bit is selected.
- Scaling \rightarrow * Automatic
- Trace Percentile \rightarrow * 99
- Data Set Percentile \rightarrow * 99
- * OK
- * OK (Output Data)

4. * Test Current Flow

* Run

< - if process starts & finishes normally >

* Run Current Flow

* Run

At this point you now have your original 3DV file orig01.3DV subsetted and bulked shifted, and output to the subBS01.3DV. See Figure 2

The "subBS01.3DV" file will be the **input file** for subsequent continuity processes that are run to determine the best parameters for this seismic data set. Selecting a "small" subset of the data allows the continuity process to run quickly and gives you a feel for how long processing will take for the entire data set.

III. Continuity Process

1. * Process
 - * Continuity
 - * Correlation
 - * Parameters
 - Comparison Option → * minimum
 - Comparison Pattern → * 2 traces
 - Vertical Window Size (ms) → * 100 (W_{corr})
 - Maximum Dip Search ms → * 0
 - Apply Threshold NO!
 - Normalization Value → * 0
 - * OK

2. * Input Data
 - * Vertical File
 - * Parameters
 - Input File → * List → * subBS01.3DV
 - * Line/Areal Extents
 - Input Direction → * Lines
 - Areal Extent → Lines * L_n * L_m
→ Traces * T_r * T_s
 - * Limit Maximum Time * t'_{bot} (200ms)
 - * Fill Gaps with dead Traces
 - * OK
 - * OK (Input Data)

3. * Output Data
 - * Vertical File
 - Output File → * (Name new file) BScont01.3DV
 - Start Time → * 0ms
 - End Time → * 200ms
 - Format → * 8 bit
 - Scaling → * Manual
 - Largest Unclipped Amplitude * 1 E * 0
 - * OK
 - * OK (Output data)

4. * Test Current Flow
 - * Run
 - < if process starts & finishes normally >
 - * Run Current Flow
 - * Run

You now have your “first pass” continuity 3DV file. (BScout01.3DV)
 See Figure III

IV. Display Refinement: Correlation Coefficient (CC) values range from +1 to -1. High positive CC values reflect similar traces, and low positive and negative CC values reflect dissimilar traces. Negative values are only generated when there is a phase reversal between adjacent traces. Therefore +99% of your continuity data will be positive and most of that 99% in “good” data will range between 0.20 and 0.95. The correlation coefficient values are “seismic data” and therefore defined by the 127 to -128 values on the left side of the color bar, and you can not edit these values. Below explains how CC values relate to color bar values and how we work around not being able to edit these values.

$$127/127 = 1.00 \text{ Correlation Coefficient}$$

$$-127/127 = -1.00 \text{ Correlation Coefficient}$$

$$n/127 = \text{Correlation Coefficient at the } n \text{ value of the color bar.}$$

Given the above, you are going to find the range of correlation coefficient values for the BScout01.3DV file. Once the range of CC values are found, you will determine the “best” Normalization Value in the Continuity-Parameter and the Largest Unclipped Amplitude in Output Data - Parameters to use so that the CC values use the full length of the color bar 127 to -128. Then you will rerun the Continuity process again changing only those two values.

- A. Bring up a seismic line in subset area.
 - 1 * Seismic → * Seismic Display Parameters
 - * set Interpolation Factors for Line, Crossline & Time to fill screen
 - * set seismic file to BScout01.3DV
 - 2 * Seismic * Reselect Time
 - * set time range 0 - 200ms (time range of bulk shifted subset)

- B. Bring up a color bar for above seismic line See Figure IV
 - 1 * Edit color bar to one color (Blue)
 - 2 * Edit color bar from “bottom” (-128) to 0 with contrasting color (Red)
 - Is any part of the seismic line red?
 - 3 * Edit color bar from “bottom” (-128) pushing “red” higher in color bar until “red” begins to be seen in the seismic line. See squiggly lines “”

in the seismic view (Figure IV). When "red" appears the "lower limit of the CC value range" is defined.

Example: "26" on color bar.

- 4 * Edit color bar from "top" 127 using "yellow". Edit color bar pushing "yellow" down in color bar until yellow begins to be seen in seismic line. See squiggly lines "s" in the seismic view (Figure IV). When "yellow" appears the "upper limit of the CC value range" is defined.

Example: "114" on color bar.

- 5 * The range of CC values can now be calculated using $n/127 = CC$ value.

Example: $26/127 = 0.20$ and $114/127 = 0.90$

- 6 Given the end members 0.20 and 0.90 for the correlation values, you want to normalize these values. (i.e. What one number subtracted from both will give values one negative and one positive centered at about zero).
See Figure V

H = upper limit of CC range (0.90)

L = lower limit of CC range (0.20)

N = number to subtract from both i.e. Normalization Value

A = Largest Unclipped Amplitude

$$\frac{H+L}{2} = N \text{ (Normalization Value)}$$

Example:

$$\frac{0.90 + 0.20}{2} = N$$

$$0.55 = N$$

H - N = A (Largest Unclipped Amplitude)

Example:	0.90 - 0.55 = "A"
	0.35 = "A"

7. Rerun Continuity Process III with following changes:
(Changes Underlined)

a) * Output Data

* Vertical File (Rename if you wish)

* Parameters

Scaling → * Manual

Largest Unclipped Amplitude * "A" value from #6 above

* OK

* OK

b) Continuity from Correlation

* Parameters

* Normalization Value * "N" value from #6 above

* OK

c) * Test Current Flow

* Run

< if process starts & finishes normally >

* Run Current flow

* Run

You now have a final continuity processed 3DV file that utilized the entire color bar.
You can change the continuity process parameters, repeating III & IV above using the subBS01.3DV file as input each time.

V. Build Cube Data File: Build a "cd" file using the output vertical file from "7a" above.
Remember that mapview (topview) is the best way to look at continuity data. Build your "cd" file accordingly. Do positive interpolations in lines and trace dimensions and negative interpolation in sample rate dimension in order to fill screen and stay under the 70% of RAM memory limit for "cd" files.

Figure 1

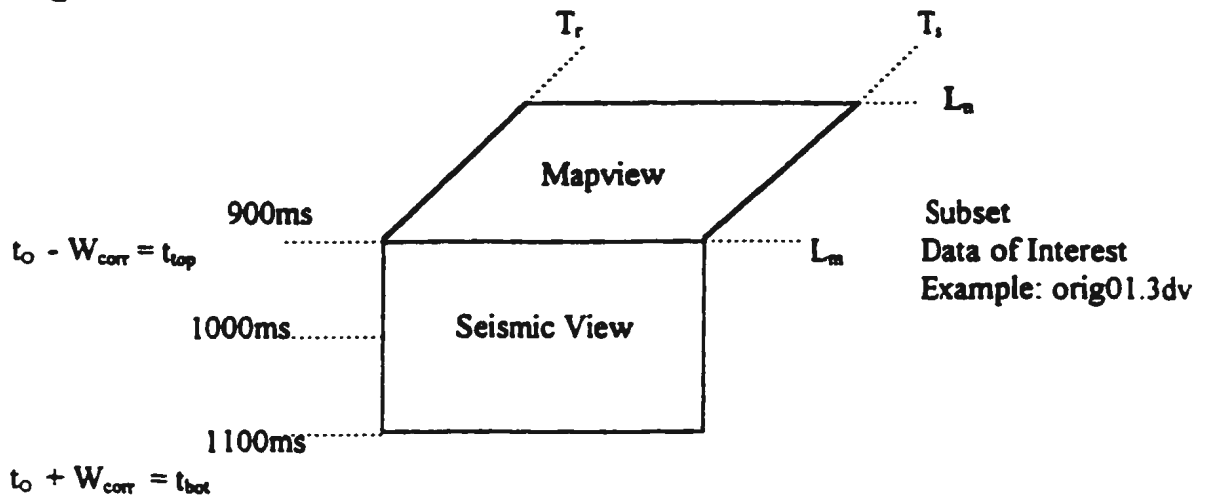


Figure 2

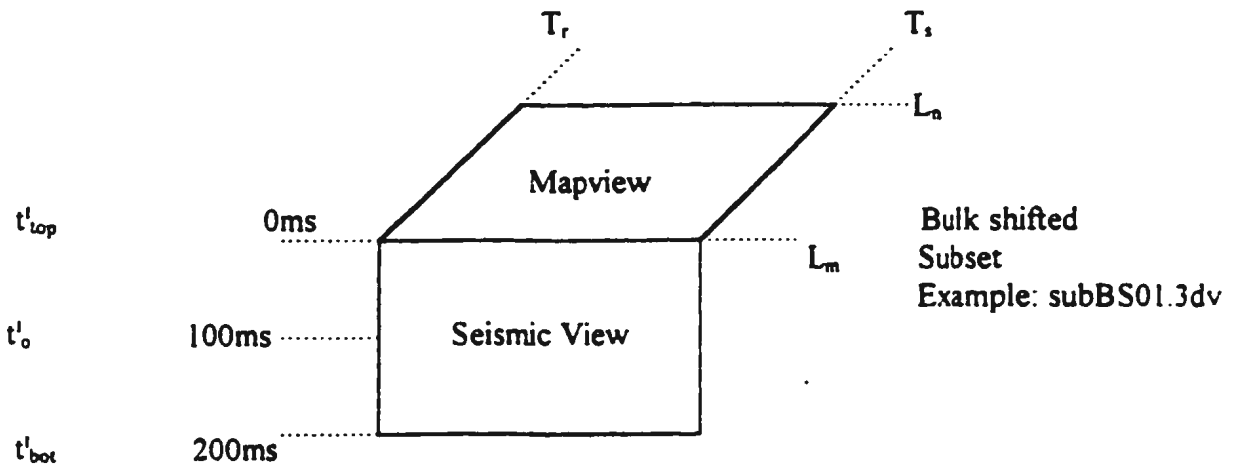


Figure 3

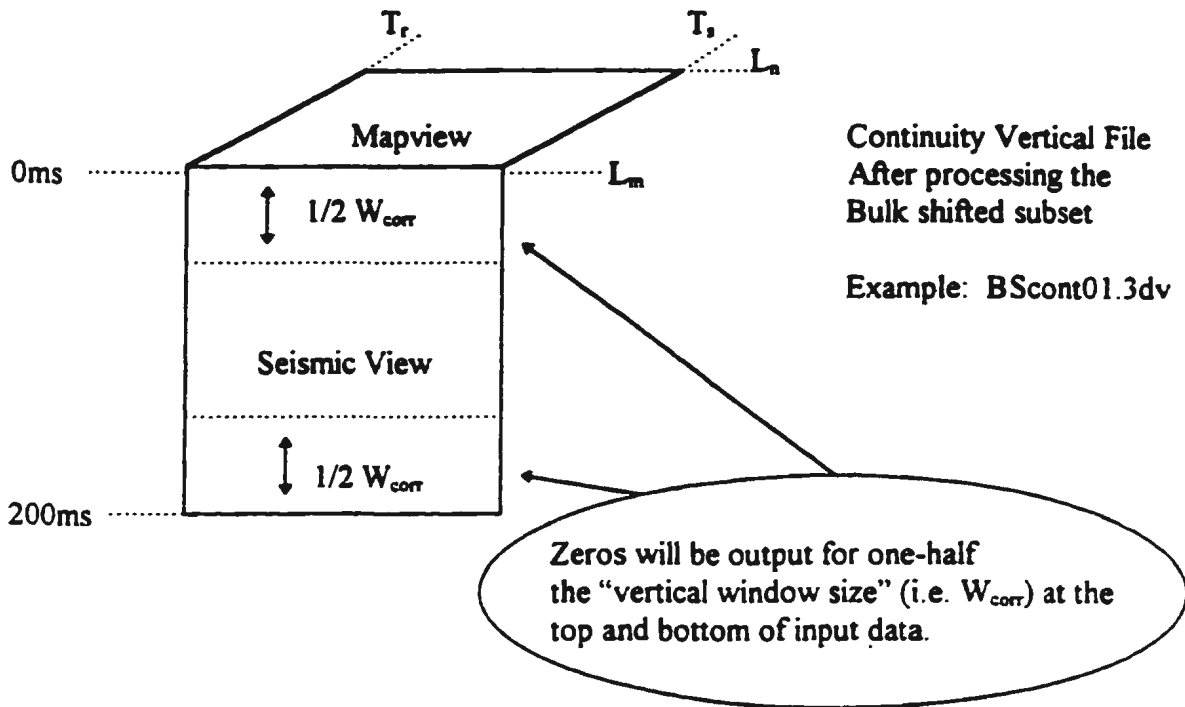


Figure 4

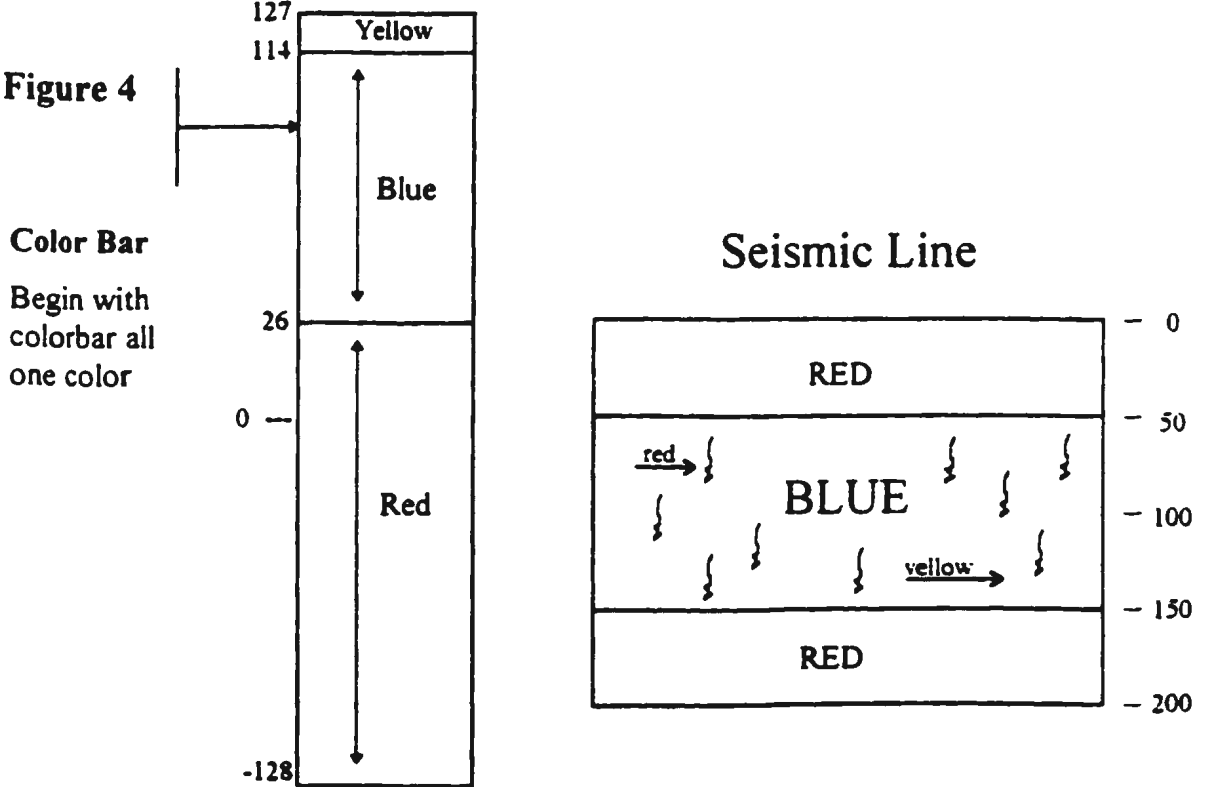


Figure 5

